Reactive Tracers in Turbulence Models

by

Sierra Legare

A thesis
presented to the University of Waterloo
in fulfillment of the
thesis requirement for the degree of
Master of Mathematics
in
Applied Mathematics

Waterloo, Ontario, Canada, 2024

© Sierra Legare 2024

Author's Declaration

This thesis consists of material all of which I authored or co-authored: see Statement of Contributions included in the thesis. This is a true copy of the thesis, including any required final revisions, as accepted by my examiners.

I understand that my thesis may be made electronically available to the public.

Statement of Contributions

Sierra Legare is the sole author of Chapters 1, 2, 3, 4, 6, and 7 which were written under the supervision of Dr. Marek Stastna. Chapter 5 (bar section 5.3) was written for publication and is an exception to sole authorship.

Research presented in Chapter 5:
This research was conducted at the University of Waterloo by Sierra Legare under the supervision of Dr. Marek Stastna. Sierra Legare conducted all data analysis and wrote the manuscript with editorial support from Dr. Marek Stastna.

Citation: Sierra Legare and Marek Stastna. Implications of Reynolds averaging for reactive tracers in turbulent flows. *Journal of Marine Science and Engineering*, 11(11):2036, 2023. [55]

Abstract

This thesis characterizes the description of two tracers, one passive and one reactive (with a particular choice of model) within Reynolds Averaged Navier Stokes simulations (RANS) and Large Eddy Simulations (LES). Both tracers are taken to be passive with respect to the fluid dynamics and the reactive tracer is assumed to undergo a growth reaction governed by Fisher's equation. To begin, the Navier-Stokes equations and the partial differential equation governing the reactive tracer evolution are Reynolds averaged and spatially filtered to obtain the governing equations for each of the turbulence models. The procedure is applied to a generalized polynomial reaction function and can be extended to other sufficiently smooth non-polynomial reactions. The Reynolds averaged and filtered reaction equations are analyzed using a simplified, zero dimensional toy model. A one dimensional toy model is used to illustrate how a non-linear reaction term, advection, and diffusion each influence the spectral distribution of a reactive tracer. To consider the effect of Reynolds averaging, an ensemble of 50 two-dimensional direct numerical simulations is run. Within each simulation, the reactive tracer is subjected to mixing induced by a Rayleigh-Taylor instability. *A priori* Reynolds averaging is applied to the ensemble data to evaluate the discrepancies between the mean system and the dynamics of the ensemble members. A two-dimensional toy model with specified velocities is used to illustrate the effect of spatial filtering. Further, the dependence of the sub-filter-scale flux and reaction terms on the cutoff wavenumber of a low-pass filter and the reaction rate is evaluated. To investigate a system with a larger range of spatial scales, *a priori* LES is applied to data from a three-dimensional simulation of a reactive tracer subjected to turbulence induced by a Rayleigh-Taylor instability. Various filter choices are applied and the sub-filter-scale terms are quantified. Given the scope of this thesis, discussions of the findings and their implications for modelling can be found at the end of chapters 5 and 6. This thesis concludes with a broader discussion of the findings and highlights avenues for future work.

Acknowledgments

Thank you to my supervisor, Marek Stastna, for consistently pushing me to become a better scientist. Your encouragement and support over the many years we have worked together have been invaluable.

Thank you to Andrew Grace for your advice on navigating the academic world.

Dedication

To Chris. And to Oakley, Jasper, and Peaches for being by my side (or on my keyboard) while I wrote this.

Table of Contents

Author's Declaration ii

Statement of Contributions iii

Abstract iv

Acknowledgments v

Dedication vi

List of Figures xi

List of Tables xvii

List of Abbreviations xviii

1 Introduction 1

1.1 Introduction for the General Public 1

1.2 Technical Introduction 3

1.3 Overview of thesis organization 10

2 Methods 12

2.1 Governing Equations 12

2.2 Non-Dimensionalization . . . 15
2.3 Notation and Vocabulary . . . 16
2.4 Reynolds Averaging . . . 17
2.4.1 Reynolds Averaging the Governing Equations . . . 17
2.4.2 Reynolds Averaging $F(\theta)$ . . . 18
2.5 Spatial Filtering for LES . . . 20
2.5.1 Filtering the Governing Equations . . . 21
2.5.2 Filtering $F(\theta)$ . . . 23
2.6 Summary of Equations . . . 25

3 Numerical Methods **27**
3.1 Filtering in Spectral Space, Resolution, and Aliasing . . . 27
3.2 SPINS . . . 29
3.3 Explicit-Implicit Euler's Method Solver in Fourier Space . . . 30

4 Analytical Treatment of the ADR Equation **35**
4.1 Understanding RANS and LES with Toy Signals . . . 35
4.2 Interpreting Dynamics in Spectral Space . . . 37
4.2.1 Non-Linear Reactions Activate Higher Wavenumbers . . . 37
4.2.2 Implications for Filtered Data . . . 40
4.2.3 Effects of Diffusion and Advection on Tracer Spectrum . . . 41
4.3 Fisher's Equation ODE Stability Dynamics . . . 45
4.3.1 Reynolds Averaging . . . 45
4.3.2 LES Filtering . . . 49
4.4 Travelling Wave Solutions . . . 50

5 Reynolds Averaging Analysis **53**
5.1 Setup for Ensemble of 50 Two-Dimensional Rayleigh-Taylor DNS using SPINS 54
5.2 *A Posteriori RANS* Results 57
5.2.1 Tracer Mean and Scalar Variance 57
5.2.2 Reynolds Stresses 62
5.2.3 Eddy Fluxes 65
5.3 Reynolds Averaged ADR Simulations 71
5.3.1 RAADR Simulation Results 72
5.4 Conclusions 77
5.5 Discussion 79

6 Large Eddy Simulations **81**
6.1 Two-Dimensional Toy Model 82
6.1.1 Toy Model Setup 82
6.1.2 Spatial Filtering 83
6.1.3 Toy Model Results 85
6.1.4 Toy Model Takeaways 91
6.2 *A Posteriori* LES on 3D Rayleigh-Taylor Simulations 96
6.2.1 3D Rayleigh-Taylor Simulation Setup 96
6.2.2 3D Filtering Results 99
6.3 Conclusions 106
6.4 Discussion 107

7 Overall Conclusions **109**
7.1 Summary 109
7.2 Discussion 111

References **115**

APPENDICES **127**

A Mathematical Treatment of Other Example Reactions **128**

A.1 Multi-Component Systems 128

A.2 Using Taylor Polynomials on Michaelis-Menten Reaction Terms 129

Glossary **131**

List of Figures

1.1 Scales of ocean processes and related reactive (biological) processes. 2

1.2 Schematic of convective cell approximation for under ice turbulence affecting phytoplankton dynamics. 4

1.3 Outline of topics covered in this thesis. Chapter numbers are shown in orange boxes. 11

3.1 Solutions to the system with $Da \sim O(10)$ using Euler's method (first column), Heun's method with Strang splitting (second column), and the difference (third column). The difference is taken by subtracting the solution found with Euler's method from that found using Heun's method. 33

3.2 (a) Maximum difference between the Euler and Heun solutions when $Da \sim O(10)$, and (b) absolute differences integrated over the domain area. 34

4.1 Result of Reynolds averaging when signals are interpreted as an ensemble versus the result of LES filtering the individual signals. 36

4.2 Cascades resulting from the evolution of different reaction terms in the absence of advection or diffusion. In the second row, the resolution is quadrupled. Note that the x-axis of each row is scaled by the Nyquist frequency corresponding to the resolution used. The initial condition is $\theta(0, x) = 0.5(\sin(4\pi x/L) + \sin(10\pi x/L))$. 39

4.3 (a) Analytical solution to the ODE with Fisher's equation and (b) solution filtered with $k_{cut} = 50$. 39

4.4 Areas in k_i–m_i space where $\exp(i(k_i+m_i)x)$ can be resolved assuming $k_{cut} = 4$. 41

4.5 Solutions to the diffusion-reaction equation in Fourier space at $t = 10$s with (a) $\kappa = 1 \times 10^{-2}$ and (b) $\kappa = 1 \times 10^{-6}$. The vertical dashed lines indicate $k_{cut} = 20$ which was chosen as an arbitrary cutoff for the purposes of illustration. 42

4.6 One dimensional tracer fields for (a) LD, (b) HD, (c) HD-LA, and (d) HD-SA. The second row shows the fields in spectral space as functions of wavenumbers and time. 44

4.7 $F(\theta) = \theta(1-\theta)$ as a function of θ. 46

4.8 (a) $\Theta(1-\Theta) - \overline{(\theta')^2}$ with a constant value of $\overline{(\theta')^2}$ given in the legend. Solutions to (b) $\Theta_t = \Theta(1-\Theta) - \overline{(\theta')^2}$ and (c) $\Theta_t = \left(\Theta(1-\Theta) - \overline{(\theta')^2}\right)\tanh(\Theta/0.001)$ with $\Theta(0) = 0.51$. 47

4.9 (a) Solutions to $\theta_t = \theta(1-\theta)$ with initial conditions randomly generated from a uniform distribution. (b) Mean and (c) scalar variance of the ensemble. 48

4.10 (a) $\langle F(\theta)\rangle$ for the various ODEs. (b) Solutions with initial condition $\theta_0 = 0.2$ and $\theta' = 0.1$. 51

5.1 (a), (c)-(e) Sample initial density stratifications perturbed by $\varepsilon(x)$ (eq 6.7). (b) Initial tracer concentration profile. 56

5.2 Mean and scalar variance of the reactive, (a) and (c), and passive, (b) and (d), tracers at $t = 26$s. 57

5.3 (a)-(b) Bulk mean tracer concentrations and (c) bulk scalar variances for the reactive (blue) and passive (orange) tracers. Shaded areas extend two standard deviations away from the mean. (d)-(e) Scalar variance integrated with respect to x for the reactive and passive tracers, respectively. 58

5.4 (a) Reactive and (b) passive tracer distributions in a sample ensemble member at $t = 26$ s. 59

5.5 (a) Bulk absolute Reynolds stresses, with shaded areas extending two standard deviations away from the mean. Normalized Reynolds stresses (b) R_{12}, (c)R_{11}, and (d)R_{22} integrated with respect to x. 61

5.6 (a) Normalized bulk mean Reynolds stress R_{12} with shaded areas extending two standard deviations away from the mean and corresponding normalized bulk gradient approximation $(U_z + W_z)/2$ calculated with all 50 ensemble members. (b) Time-dependent eddy viscosities from equation 5.6. (c) Normalized R_{12} and (d) normalized gradient approximations for the entire ensemble and two unique subsets of 25 members. 63

5.7 (a) Turbulent kinetic energy given by equation 5.8 integrated with respect to x. (b) Kinetic energy of the mean integrated with respect to x. (c) KEs integrated in x and z (TKE in blue and KE of mean in orange). 64

5.8 Bulk absolute value of the (a) horizontal and (b) vertical eddy fluxes of the reactive (blue) and passive (orange) tracers. Vertical eddy fluxes integrated with respect to x for the (c) reactive and (d) passive tracers. 65

5.9 Normalized bulk absolute values of the (a) horizontal and (b) vertical, eddy fluxes of the reactive (blue) and passive (orange) tracers. The bulk absolute values of the derivatives of the mean tracers are plotted for comparison. Time-dependent (c) horizontal and (d) vertical eddy diffusivities. 67

5.10 Absolute angle between the eddy flux and gradient of the mean at (a) $t =$ 14s, (b) $t = 26s$, and (c) $t = 40s$ quantified as a proportion of the total number of grid points. 68

5.11 Angle between the eddy flux at gradient for the (a) reactive and (b) passive tracers at $t = 26$s. 69

5.12 Passive tracer concentration integrated with respect to x from (a) a sample member, (b) the ensemble mean, (c) simulation S, and (d) simulation SF. . 73

5.13 Reactive tracer concentration integrated with respect to x and plotted as a function of z and time. The panels correspond to (a) a sample member, (b) the ensemble mean, and simulations (c) S, (d) SF, (e) SR, and (f) SFR. . . 74

5.14 Bulk (a) reactive and (b) passive tracer concentrations for a sample member, the ensemble mean, and the pseudo-RANS simulations. 75

5.15 Reactive tracer concentration at $t = 40$s. The panels correspond to (a) a sample member, (b) the ensemble mean, and simulations (c) S, (d) SF, (e) SR, and (f) SFR. 76

6.1 (a) Initial tracer distribution for both the reactive and passive tracers. (b) Large and (c) small scale components of the stream function. 83

6.2 (a) Square and (b) circular filters with cutoff values of 100. (c) Reactive and (d) passive tracer power spectral densities at $t = 0.5$s. 84

6.3 Evolution of the reactive (first row) and passive (second row) tracer distributions at $t = 0.1$s (a, d), $t = 0.3$s (b, e), and $t = 0.5$s (c, f). Note the difference in the colorbar limits in the two rows. 85

6.4 Time-averaged absolute (a) resolved, (b) cross-scale, and (c) sub-filter-scale components of the residual stress tensor plotted as a function of the wavenumber cutoff, k^{cut}. 86

6.5 Figure 6.5: (a) Reactive tracer concentration at t = 0.5 s. Low-pass filtered reactive tracer concentration with cutoffs of (b) 10, (c) 20, (d) 40, (e) 60, (f) 100. 87

6.6 (a) Unfiltered reactive tracer concentration at $t = 0.3$ s. Differences between reactive tracer data filtered with the square and circular filters for cutoffs of (b) 10, (c) 20, (d) 40, (e) 60, (f) 100. 88

6.7 Sum of the norm of the time-averaged components of the **sfs** fluxes, $\vec{f}^A$, on the (a) resolved-scale, (b) cross-scale, and (c) sub-filter-scale. The vertical line in panel (c) at a wavenumber of 4π indicates the point at which the sub-filter-scale fluxes go to zero. 89

6.8 Norm of the time-averaged components of the **sfs** reactions, f^R, for (a) $Da \sim O(0.1)$, (b) $Da \sim O(1)$, and (c) $Da \sim O(10)$. The first vertical black line indicates the wavenumber for which the sum of the resolved components becomes equal to that of the sub-filter-scale components. The second line shows the same for the cross-scale components. The second row of panels provides a close up of the same data for the cases (d) $Da \sim O(0.1)$, (e) $Da \sim O(1)$, and (f) $Da \sim O(10)$. 90

6.9 The norms of the components of the **sfs** reaction term integrated over the domain and scaled by Da. The first row has $k^{cut} = 10$ and the second has $k^{cut} = 100$. The columns, from left to right, correspond to the simulations with $Da \sim O(0.1)$, $Da \sim O(1)$, and $Da \sim O(10)$. 92

6.10 The norms of the components of the vertical **sfs** flux integrated over the domain. The first row has $k^{cut} = 10$ and the second has $k^{cut} = 100$. The columns, from left to right, correspond to the simulations with $Da \sim O(0.1)$, $Da \sim O(1)$, and $Da \sim O(10)$. 93

6.11 The components of the **sfs** reaction term integrated over the domain and scaled by Da. The first row has $k^{cut} = 10$ and the second has $k^{cut} = 100$. The columns, from left to right, correspond to the simulations with $Da \sim O(0.1)$, $Da \sim O(1)$, and $Da \sim O(10)$. Note that only the yellow curves are observable since the blue and red curves have tiny values. 94

6.12 The components of the vertical **sfs** flux integrated over the domain.The first row has $k^{cut} = 10$ and the second has $k^{cut} = 100$. The columns, from left to right, correspond to the simulations with $Da \sim O(0.1)$, $Da \sim O(1)$, and $Da \sim O(10)$. Note that the values in the second row are on the order of machine precision. 95

6.13 (a) The initial reactive and passive tracer profiles with respect to the vertical. (b) The mean initial excess density profile with respect to the vertical. (c) The excess density at $z = 0.256$ m. 97

6.14 Filters used on the 3D data in the (a) k and l directions and (b) m direction. The smoothed and sharp filters retain all wavenumbers between the cutoff lines. The wide smoothed filter is the least harsh, as it retains a larger range of wavenumbers. 99

6.15 Evolution of the reactive tracer field. $x - z$ slices are taken at $y = 0.512$ m and at (a) $t = 10$ s, (b) $t = 16$ s, and (c) $t = 22$ s. $x - y$ slices are taken at $z = 0.3462$ m at the same times. 100

6.16 Normalized differences between the unfiltered reactive tracer field at $t = 22$ s and $y = 0.512$ m and data filtered with (a) the sharp filter, (b) the smoothed filter, (c) the wide smoothed filter, and (d) the Gaussian filter. 101

6.17 Unfiltered reactive tracer norm integrated in x and y at (a) $t = 10$ s, (d) $t = 16$s, and (g) $t = 22$ s. The second column shows the differences between the profiles of the unfiltered data and data filtered with the various filter choices at the corresponding times. The third column shows the profiles of the norm of the differences between the unfiltered data and filtered data. . 102

6.18 The **sfs** reaction components at $t = 22$ s integrated with respect to x and y for the data filtered with the (a) sharp filter, (b) smoothed filter, (c) wide smoothed filter, and (d) Gaussian filter. 103

6.19 Profiles of the components of the vertical **sfs** flux term under the sharp filter. Panels (a) and (c) show the reactive and passive tracers, respectively, at $t = 16$ s. The second column corresponds to $t = 22$ s. 104

6.20 (a, d) Resolved-scale, (b, e) cross-scale, and (c,f) **sfs** components of the **sfs** reaction term (first row) and the vertical **sfs** flux term (second row) at $y = 0.512$ m and $t = 22$ s. The **sfs** terms are obtained using the sharp cutoff filter. Both the **sfs** flux and reaction terms have a negative coefficient in the filtered equations that is not being accounted for in this figure. 105

7.1 The first panel shows the generation of an internal wave over a sill. Within the wave, a recirculating core forms. Large enough topography induces separation. The second panel shows an internal wave of depression shoaling over undulating topography. As the wave shoals, instabilities are generated and breakdown into turbulence. The second panel is reproduced from [87] with permission. 114

List of Tables

4.1 Simulations run with the one dimensional toy model. We use the root-mean-square of the prescribed velocity as the characteristic velocity scale and $L = 1$ (domain half width) as the characteristic length scale. 43

5.1 Simulation parameters and dimensionless numbers for Rayleigh-Taylor Ensemble. 54

6.1 Simulation parameters and dimensionless numbers for Toy Model 82

6.2 Parameters and Dimensionless numbers corresponding to the 3D simulation. 98

List of Abbreviations

sfs Sub-filter-scale 6

ADR Advection-diffusion-reaction 7

DNS Direct numerical simulation 5

LES Large eddy simulation 5

NPZ Nutrient-phytoplankton-zooplankton 3

RANS Reynolds averaged Navier-Stokes as an acronym. The term is commonly used as a noun to refer to models in which the Reynolds Averaged Navier Stokes equations are used. 5

RT Rayleigh-Taylor 10

Chapter 1

Introduction

1.1 Introduction for the General Public

Within the oceans, fluid motions occur on an incredible range of scales. Many of these motions are turbulent in nature and are known to cause strong mixing [25, 85]. Turbulent flows are characterized by large, irregular variations in space and time, making their details unpredictable [52]. These variations often manifest in the form of vortices or filaments. The concept of energy transfer is fundamental to the study of turbulent flows. It is understood that kinetic energy is transferred from the largest scales of motion by non-linear, largely inviscid interactions until it reaches sub-centimeter scales at which point it is dissipated by viscous forces [72]. Meanwhile, gyres in the oceans can form on 1000 kilometer scales [90].

Modern oceanography relies on field measurements, remote sensing, and, increasingly, numerical simulations of ocean processes. All of these have their own established methodology, yet all fail to provide a complete description of the ocean. While numerical models play an important role as investigative and predictive tools of ocean processes [96, 48, 77, 36, 11], they are limited by the underlying numerical method and model resolution. These are, in turn, limited by the availability of computational resources [37, 31].

A host of biogeochemical processes exist within the oceans and the effect of turbulent mixing on these processes cannot be ignored [59, 50, 46]. For instance, transport plays an important role in many ecosystem dynamics [44, 97]. Biogeochemical processes have their own characteristic length and time scales (e.g. the seasonality and distribution of phytoplankton blooms). Studying these processes is complicated by the coupling of environmental and internal factors. For example, migration patterns are dependent on seasonal

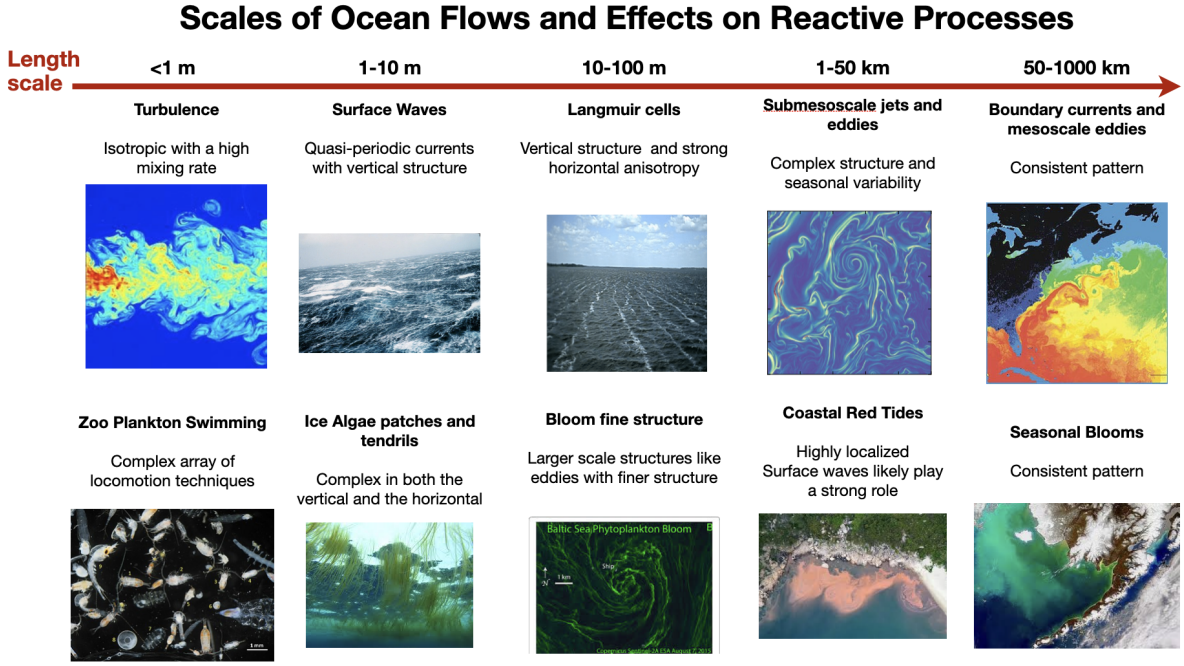


Figure 1.1: Scales of ocean processes and related reactive (biological) processes.

timescales and biological factors, but may also vary according to environmental conditions [108]. Even small fluctuations in environmental conditions in the form of noise can induce resonance in population dynamics, causing large oscillations [13].

Figure 1.1 provides an overview of the range of active scales in the oceans and some of the reactive biological processes that occur at these scales. Coupling hydrodynamic and biogeochemical models only increases the computational demand of a simulation [32]. For this reason, ocean modellers must make choices as to which processes to resolve, which to parameterize, and at times, even which to ignore.

The necessary approximations and parameterizations used to handle turbulence in ocean models (see the technical introduction below 1.2) inevitably affect our interpretation of the biogeochemical aspects of these systems. A multitude of reactive passive tracers (simplified to reactive tracers in what follows) exist within the oceans. Herein, we use the reactive tracer terminology to describe tracers that are passive with respect to fluid dynamical processes, but reactive in a biological or chemical sense. The term passive tracer indicates that the tracer is non-reactive. Examples of reactive tracers include phytoplankton, nutrients [39, 24], and carbon [77] among others.

The effect of turbulence on the reaction dynamics of nutrient phytoplankton zooplankton (NPZ) models has been considered from several different lenses [71, 93, 78]. Complications arise from the impact of turbulence on the spatial distribution of a reactive tracer possibly affecting the reaction rate [78]. Phytoplankton rely on light and nutrient availability, both of which are spatially heterogeneous. Turbulent mixing replenishes nutrients to areas where phytoplankton blooms may quickly deplete them [27]. Transport of phytoplankton towards (or away from) favorable conditions affects growth rates and overall ecosystem dynamics [94, 91]. This is particularly important in polar environments that can be both nutrient and light limited [18, 66, 92, 54]. To complicate matters further, phytoplankton have been found to adjust their buoyancy to sink on timescales of seconds, which increases the nutrient flux to their cells [34]. Additionally, it has been posited that phytoplankton retain some memory of the turbulent mixing they have been subjected to and that this has an effect on their affinity for nutrients [81].

Simplified models of thermal convection have been used in an attempt to explain the impacts of convection, diffusion, and phytoplankton sinking on growth dynamics [93, 94]. These toy models generally use large cell convection to approximate the convective cells expected to form due to thermal convection. A schematic of this setup is shown in Figure 1.2. Unfortunately, studies of this form neglect the effects of multi-scale turbulent motions. Submesoscale features result in strong vertical velocities that enhance the vertical transport of tracers [8, 114, 107], particularly in winter [61]. Accounting for submesoscale physics in numerical models of phytoplankton can result in spatial distributions dominated by fine structures [64].

This thesis will illustrate some of the ways turbulent mixing can affect the dynamics of a reactive tracer. Additionally, we will consider how the reactive tracer dynamics are altered when interpreted through the *a posteriori* application of two forms of turbulence models. To the best of the author's knowledge, there are no published studies outlining these details for a model reactive tracer. Numerous studies have been performed in specialized applications, though none take into account how the model formulation itself affects the interpretation of the reaction dynamics.

1.2 Technical Introduction

It is well-known that limitations on resolution make studying turbulent flows challenging. Hence, the emergence and continued development of the turbulence modelling literature. When a reactive tracer is introduced into a turbulent environment, the reaction dynamics introduce additional length scales. Since few coupled hydrodynamic-biogeochemical models

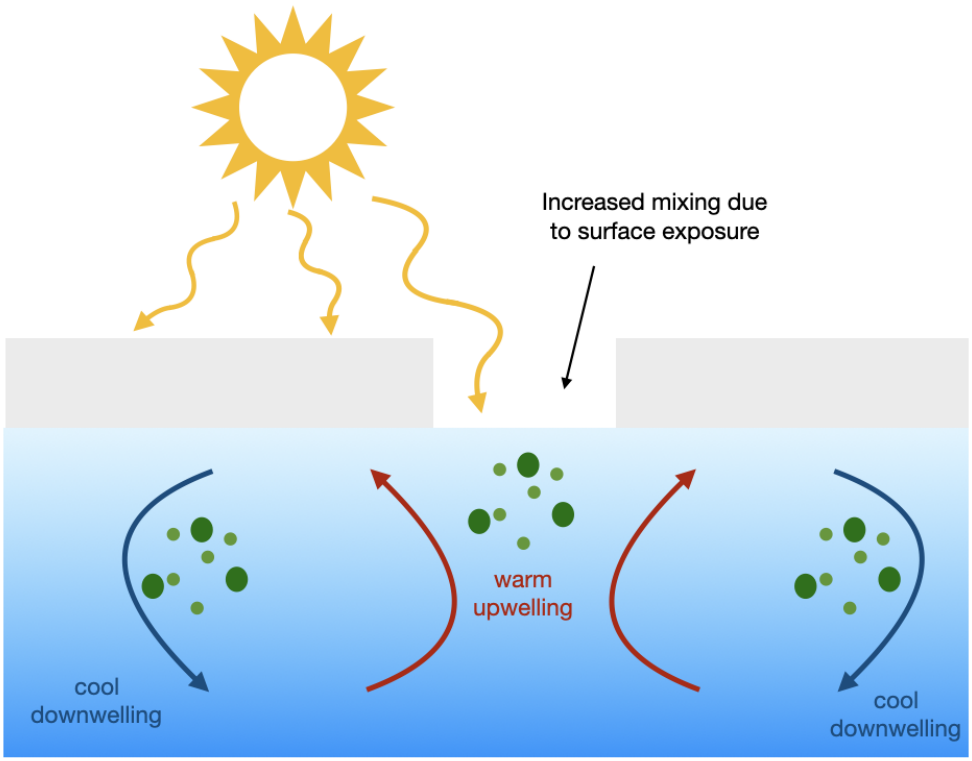


Figure 1.2: Schematic of convective cell approximation for under ice turbulence affecting phytoplankton dynamics.

perform direct numerical simulations (DNS), it is difficult to pinpoint the interplay between turbulent mixing and reaction dynamics. When advective and reactive timescales are on the same order of magnitude, these effects have the potential to become tightly coupled. Field studies [100] are limited by the resolution of observations and geographic applicability. Turbulence modelling studies [91] are limited by the need for parameterizations. Not only is the interplay between turbulent mixing and reaction dynamics not well understood, but there are no standard best practices for modelling reactive tracers within turbulence models. Two of the most widely used turbulence modelling frameworks are Reynolds-averaged Navier Stokes (RANS) simulations and Large Eddy Simulations (LES) [72].

When simulating systems in which there is a high degree of variability, running ensembles is a common practice. An ensemble consists of a set of numerical simulations and allows for the mean state of a system to be quantified. By quantifying the fluctuations of the ensemble members around the mean, the variability of the system can be evaluated and a range of outcomes identified.

Consider Burgers' equation in one dimension as an example

$$u_t + uu_x = \nu u_{xx} \tag{1.1}$$

where subscripts denote partial derivatives. The procedure for deriving the Reynolds averaged Burgers' equation is as follows. Begin by splitting u into a mean part, U, and a part representing fluctuations about the mean, u', such that $u = U + u'$. We then substitute this expression into Burgers' equation

$$(U + u')_t + (U + u')(U + u')_x = \nu(U + u')_{xx}, \tag{1.2}$$

$$U_t + u'_t + UU_x + Uu'_x + u'U_x + u'u'_x = \nu U_{xx} + \nu u'_{xx}. \tag{1.3}$$

Reynolds averaging (denoted by overbars) removes the terms that are linear in u' because the mean of the fluctuations is zero, $\overline{u'} = 0$. Note that any terms that are non-linear in u' are retained. Applying this procedure leaves us with an equation that resembles Burgers' equation for the mean, U, but contains corrections in terms of the unknown fluctuations, u'.

$$U_t + UU_x = \nu U_{xx} - \overline{u'u'_x} \tag{1.4}$$

If we were to solve the Reynolds averaged system, we would need to parameterize or ignore the unknown term.

Under LES, equations are filtered to retain only the larger-scale components. Let angled brackets denote the filtering operation. Quantities are decomposed as $u = \langle u \rangle + u'$ where u'

now denotes the sub-filter-scale contributions. Rather than substituting this decomposition into the Burgers' equation, we filter the equation directly

$$\langle u_t \rangle + \langle u u_x \rangle = \nu \langle u_{xx} \rangle, \tag{1.5}$$
$$\langle u \rangle_t + \langle (\langle u \rangle + u')(\langle u \rangle_x + u'_x) \rangle = \nu \langle u \rangle_{xx}, \tag{1.6}$$
$$\langle u \rangle_t + \langle \langle u \rangle \langle u \rangle_x + u' \langle u \rangle_x + \langle u \rangle u'_x + u' u'_x \rangle = \nu \langle u \rangle_{xx}. \tag{1.7}$$

Next, to obtain something that resembles Burgers' equation with a correction, we need to add and subtract $\langle u \rangle \langle u \rangle_x$ as follows

$$\langle u \rangle_t + \langle u \rangle \langle u \rangle_x - \langle u \rangle \langle u \rangle_x + \langle \langle u \rangle \langle u \rangle_x + u' \langle u \rangle_x + \langle u \rangle u'_x + u' u'_x \rangle = \nu \langle u \rangle_{xx}, \tag{1.8}$$
$$\langle u \rangle_t + \langle u \rangle \langle u \rangle_x = \nu \langle u \rangle_{xx} + \langle u \rangle \langle u \rangle_x - \langle \langle u \rangle \langle u \rangle_x \rangle - \langle u' \langle u \rangle_x + \langle u \rangle u'_x \rangle - \langle u' u'_x \rangle. \tag{1.9}$$

The last terms on the right-hand side form the correction. Note that it is written in terms of both filtered and sub-filter-scale (**sfs**) quantities.

RANS and LES are fundamentally different in their representation of a turbulent system, but similar in their treatment of parameterized processes. The fundamental assumption in RANS is that the most feasible representation of a turbulent system with a high degree of variability is through an ensemble mean. In practice, running an ensemble of any large, three-dimensional system is not computationally feasible and so a set of equations describing the mean state of a system is solved instead. Each quantity of interest is decomposed into two parts; a mean, and fluctuations about the mean. Equations describing the evolution of the mean state of the system are then obtained by substituting the decomposition into the governing equations and then Reynolds averaging (see section 2.4 for the detailed procedure). Any terms involving the fluctuations need to be parameterized. Reynolds averaging the Navier-Stokes momentum equation introduces the Reynolds stress tensor which poses a closure problem as it is defined in terms of the fluctuations which are not known [72]. Eddy viscosity models are the most common choice for parameterizing Reynolds stresses, largely owing to their relative simplicity. These models assume that the Reynolds stress tensor is aligned with the mean strain tensor, allowing the Reynolds stress term to be related to the ensemble mean velocity field [52, 72]. In practice, the Reynolds stress terms in the RANS momentum equation are replaced by simply introducing additional viscosity into the system [72]. These models assume that the local gradient of the mean velocity field dictates the direction of flux. However, if the advection in a turbulent flow is strong enough, the large eddies that emerge may dominate and cause the flux to be oriented against the gradient [52], making the eddy viscosity assumption invalid. In particular, there are cases in which the eddy viscosity becomes negative and the model breaks

down because anti-diffusion is mathematically ill-posed [73]. There are numerous eddy viscosity models which fall under the broad categories of mixing-length models, one-equation models, and two-equation models among others [109]. Other eddy viscosity models have been developed for large eddy simulations, such as the Lilly-Smagorinsky model [111].

Analogously, the eddy fluxes that emerge from Reynolds averaging scalar transport equations are often modelled by eddy diffusivities. Eddy diffusivities have been estimated for passive tracers with satellite observations and found to be strongly space and time dependent [2]. In the upper 2000m of the oceans, horizontal eddy diffusivities on a 300km scale range between $10^2 \mathrm{m}^2/\mathrm{s}$ and $10^4 \mathrm{m}^2/\mathrm{s}$ [20, 65, 80]. The expression used to calculate the eddy diffusivity inevitably affects the estimate. If one were to consider the suppression of mixing by mean currents, then the spatial distribution and magnitude of the eddy diffusivities would differ dramatically [29] compared to estimations that simply use mixing length theory [43]. Evidence has suggested that in stratified fluids, the ocean being a prime example, vertical eddy diffusivity should be modelled as a decreasing function of buoyancy frequency [33]. When considering a reactive tracer eddy diffusivity parameterizations must be treated with caution as the timescale of a particular reaction dictates the amount of effective eddy diffusivity experienced by a tracer [71] as does the mixing regime in which the tracer is located [84].

Eddy mixing is strongly dependent on the tracer being considered [47]. Active tracers may require counter-gradient fluxes rather than down gradient fluxes, resulting in negative eddy diffusivities [84]. For instance, double diffusion displays counter-gradient density flux while turbulence transports density down-gradient [76]. Though some methods for determining eddy diffusivities and transport characteristics have shown indistinguishable performance when used for passive or active tracers [7], this is not necessarily the case for reactive tracers. Several methods for modelling the eddy diffusivity of a reactive tracer have been presented in the literature. Ensembles of Lagrangian particle trajectories have been used to determine a time-dependent diffusion function that yields the effective eddy diffusivity when evaluated at the reaction timescale [71]. The gradient-diffusion hypothesis has been examined by regressing true eddy fluxes onto tracer gradients to determine an effective eddy diffusivity [74]. It was shown to perform more poorly for reactive versus non-reactive tracers, with specifics depending on model parameters.

NPZ models are generally described with advection–diffusion–reaction (ADR) equations. When Reynolds averaging is applied to the reaction term, eddy reactions, defined as covariances of tracer fluctuations, are introduced. Eddy reactions are inevitably strongly reaction dependent and have been shown to be sensitive to seasonality, location, and spatial scales for some NPZ models [58]. In a study of phytoplankton primary production and zooplankton grazing, it was shown that $\pm 5\%$ to $\pm 30\%$ of productivity and grazing was

due to eddy reactions on a sub 100km scale [58]. Similarly, resolving down to the submesoscale (as opposed to the mesoscale) was shown to result in a decreased phytoplankton abundance of 10 to 20% when the model was integrated over 50 years [63]. To the best of our knowledge, there is no standard practice for parameterizing eddy reaction terms.

The Regional Ocean Modelling System (ROMS) is a popular tool for conducting regional (on the order of tens of kilometers) simulations due to its flexibility and stable numerical methodology. ROMS, and similar models, effectively solve the Reynolds Averaged Navier-Stokes (RANS) equations. It has a topography-following coordinate system in the vertical, an implicit free-surface, and can be run as a coupled physical-biogeochemical model [53]. ROMS is a split-explicit model, meaning fast and slow dynamics are split into sub-problems. If non-dissipative time-stepping is used for both, the model becomes unstable [38, 42]. Time-stepping algorithms with forward-backward feedback are used to enhance the internal stability of the model [82]. In addition to the numerical diffusivity introduced by the time–stepping method, ROMS treats horizontal and vertical diffusion differently, and has a number of options for parameterizing vertical mixing [38, 1] all of which are, by nature, dissipative [17]. While not strictly necessary, the majority of regional modeling studies invoke the hydrostatic approximation, meaning some processes (e.g. density overturns) are inherently excluded from consideration. Example use cases for ROMS include the Atlantic Canada Model (O(10km) horizontal resolution and 30 vertical levels) [16], the Coupled-Ocean-Atmosphere-Wave-Sediment-Transport modeling system (4.7-9.0km horizontal resolution, 50 vertical layers spanning 8km) [51], and studies of storm induced circulation and hydrography changes in tropical regions (6km resolution) [89]. The diversity of studies that use ROMS indicates the importance of model flexibility and adaptability.

In addition to being a popular tool for examining oceanic ecosystems, RANS has been used to model reactive tracers in the contexts of water disinfection [112, 113, 5], the spread of air pollutants [106], and combustion [6]. For a discussion of several classes of models, as well as popular modelling techniques and closures when using RANS for turbulence modelling, see [4]. For a review of the uncertainty in RANS models, see [110].

In LES, the governing assumption is that large-scale features dominate the system dynamics, so the smaller-scale features can be parameterized. The division between large and small scales is a function of the model resolution, and so quantities are decomposed into resolved and sub-grid-scale parts. To obtain equations describing the evolution of the resolved portion of each quantity, the governing equations are filtered (see section 2.5 for the detailed procedure). The terms involving sub-grid-scale (equivalently called sub-filter-scale) quantities are then parameterized. LES essentially aims to improve low resolution simulations by including parameterizations of the processes that cannot be resolved. When

filtering the Navier Stokes equations, a residual stress tensor is introduced which is analogous to the Reynolds stress term in RANS and is also often parameterized with an eddy viscosity model. As an example, the Germano dynamic model dynamically calculates an eddy viscosity from the smallest resolved scales under the assumption that turbulence is similar on all small scales [35]. Filtering scalar transport equations introduces sub-filter-scale flux terms that are analogous to the eddy fluxes introduced in RANS and also often represented by eddy diffusivity parameterizations. The two frameworks share many similarities in terms of what the unknown quantities are. However, it is important to remind oneself that RANS and LES provide very different representations of a system.

LES filtering is often performed *a posteriori* to DNS to analyze contributions at varying length scales. Note that this is called *a priori* analysis by convention. Filtering can be performed in physical space, but is most often performed in Fourier space [56]. Turbulence is well known to lead to a cascade as energy moves from larger to smaller scales in a nearly inviscid manner, before being dissipated by viscosity [52]. This is often expressed using Fourier theory in what is referred to as a spectral cascade, wherein higher wavenumbers become active as the cascade progresses. A reactive tracer in a turbulent flow would be expected to follow a similar spectral cascade. However, the introduction of additional variability in the tracer distribution due to local growth or decay will inevitably affect the spectral distribution, though details are not *a priori* known from the equations themselves. When advective and reactive timescales are on the same order of magnitude, these effects have the potential to become tightly coupled.

Diffusion acts to smooth a physical distribution and thus limits the cascade of spectral power to higher wavenumbers. The combined effects of diffusion and turbulence have been found to enhance reaction excitability in the Truscott-Brindley Model [98] under a particular set of conditions (the relative sizes of the Damköhler number and the fraction of the initial state that is excitable) [78]. However, too large a diffusivity value simply results in a loss of spatial structure. Therefore, by artificially increasing the diffusivity of a tracer through an eddy diffusivity parameterization, one constrains its spectral distribution in addition to possibly restricting feedbacks between the fluid physics and reaction dynamics. This likely results in the overestimation of large-scale features since interscale transfer down to smaller scales is suppressed.

Observations of plankton distributions in the oceans are often reported in the form of spectral slopes. In an effort to explain the differences in the spectral slopes of phytoplankton and zooplankton, numerical experiments have been conducted to investigate the effects of advection, diffusion, and varying reaction timescales [15, 3]. The general consensus is that phytoplankton have steeper spectral slopes than zooplankton because they are consumed quickly enough to not have time to cascade down to smaller scales. The

spectral distributions are reliant on the predator-prey (reaction) dynamics [10]. However, one factor to note is that the forms of the phytoplankton and zooplankton reaction terms differ. If the reaction dynamics influence the spectral distribution of a reactive tracer, then the differences in the slopes may be governed by the forms of the reactions at first order, with the reaction timescales playing a secondary role.

Considering that reactions have the potential to introduce fine spatial features beyond what one would expect from turbulence alone, running coupled hydrodynamic biogeochemical models with an overly coarse resolution should be avoided wherever possible. For instance, resolutions on the order of tens of kilometers [18] are bound to miss significant dynamics that have the potential to change quantitative if not also qualitative model outcomes. In geophysical fluid dynamics, substantial work has been done to develop and evaluate parameterizations [67]. LESs have thus been used for studies of ocean processes fairly reliably [83]. The same cannot be said for sub-grid-scale reaction parameterizations, and perhaps it is not a fair comparison. After all, each reactive tracer evolves according to its own unique dynamics and equations.

1.3 Overview of thesis organization

In this thesis, we consider an idealized model reactive tracer that undergoes a growth reaction governed by Fisher's equation. In Chapter 2, we begin by treating the incompressible Navier-Stokes equations and the advection-diffusion-reaction equation describing the tracer evolution. The governing equations are Reynolds averaged and spatially filtered. The detailed procedures are shown for a generalized polynomial reaction function and extended to a multi-component system. As an example, the procedure is applied to a Michaelis-Menten reaction term to demonstrate how it might be adjusted for non-polynomial reaction functions. Chapter 3 presents the numerical methods used in the subsequent analysis. In Chapter 4 the advection-diffusion-reaction system is systematically analyzed. The system's evolution in spectral space is explored with a toy model to illustrate the competing effects of advection, diffusion, and the reaction on the presence of fine spatial features. Differences that arise from RANS or LES are highlighted from both a signal interference perspective and through a stability analysis of a single-spatial point model. The results from performing *a priori* RANS on an ensemble of 50 two-dimensional Rayleigh-Taylor (RT) simulations are presented in Chapter 5. To compliment the *a priori* analysis, the Reynolds averaged advection-diffusion-reaction system is solved using data from the ensemble. Chapter 6 presents the results of spatial filtering a two-dimensional toy model (for the purposes of developing some intuition) and a three-dimensional Rayleigh-Taylor

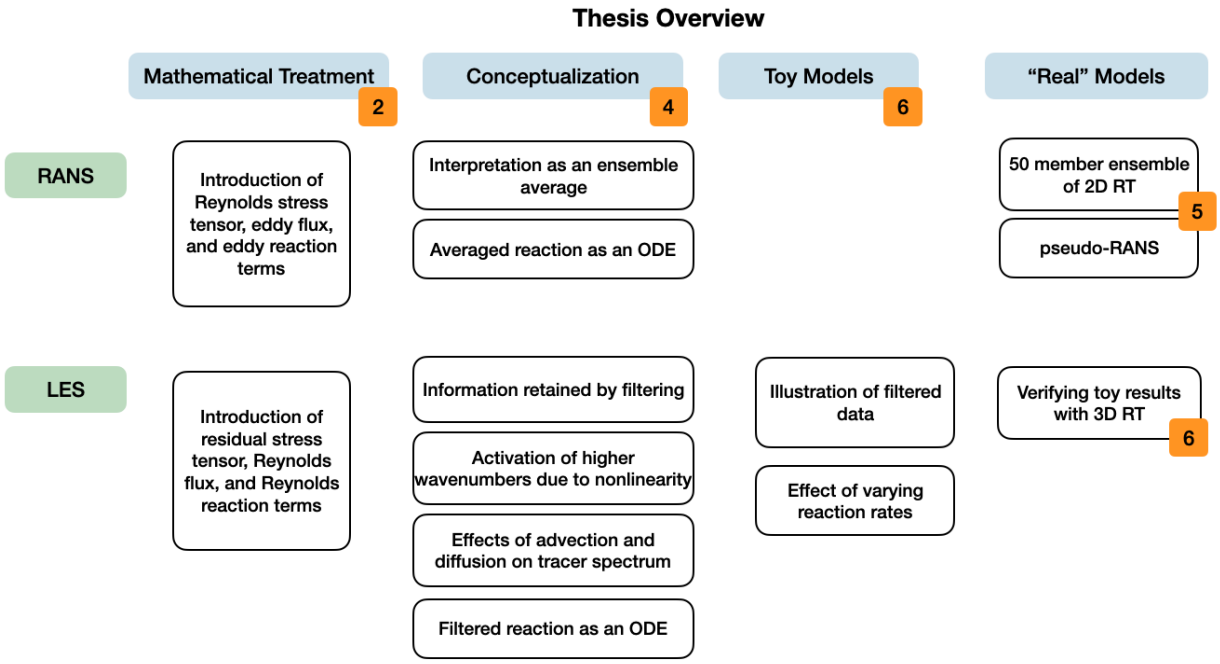


Figure 1.3: Outline of topics covered in this thesis. Chapter numbers are shown in orange boxes.

simulation. Figure 1.3 shows how the various topics discussed herein are interconnected. The thesis concludes with a discussion of the results and highlights how they might be helpful in model development.

Chapter 2

Methods

This chapter introduces the governing equations, their dimensionless forms and the notation to be used throughout the remainder of this thesis. The Reynolds averaging procedure presented in Section 2.4 is pertinent for the ODE analysis in Section 4.3 and for the *a priori* Reynolds averaging results presented in Chapter 5. The filtering procedure performed in Section 2.5 is relevant to the majority of Chapter 4 and to all of Chapter 6 which discusses the results from filtering a toy model and three-dimensional data. Sections A.1 and A.2 are provided for the reader interested in applying the procedures of the earlier sections to a more complex system. Appendix A provides examples of how the mathematical treatment presented in this chapter might be applied to multi-component or non-polynomial reaction functions.

2.1 Governing Equations

Consider the following set of partial differential equations

$$\rho\vec{u}_t + \rho\nabla\cdot(\vec{u}^{\,T}\vec{u}) = -\nabla p + \rho\vec{g} + \mu\nabla^2\vec{u}, \tag{2.1}$$

$$\frac{1}{\rho}\frac{D\rho}{Dt} + \nabla\cdot\vec{u} = 0, \tag{2.2}$$

$$\frac{D\rho}{Dt} = \kappa_\rho\nabla^2\rho, \tag{2.3}$$

$$\theta_t + \nabla\cdot(\vec{u}\theta) = \kappa\nabla^2\theta + F(\theta). \tag{2.4}$$

The first two are the Navier-Stokes equations for the conservation of momentum and the conservation of mass, respectively [52]. The third is an advection-diffusion-reaction (ADR) equation describing the evolution of a scalar tracer undergoing a reaction given by the function $F(\theta)$ and is coupled to the first two equations through the advection term.

Under the Boussinesq approximation, density changes are treated as negligible except where multiplied by $\vec{g}$. The magnitude of the $(1/\rho)D\rho/Dt$ term in the continuity equation is much smaller than that of the velocity gradients, so equation 2.2 can be replaced with the incompressibility condition

$$\vec{\nabla} \cdot \vec{u} = 0. \tag{2.5}$$

Suppose there exists some reference state wherein the density, ρ_0, is constant and the hydrostatic pressure is $\vec{\nabla} p_0 = \rho_0 \vec{g}$. Then we can write $\rho(\vec{x}, t) = \rho_0 + \rho_E(\vec{x}, t)$ where ρ_E is the excess density and $p(\vec{x}) = p_0(z) + p_E(\vec{x})$. Substituting into equation 2.1, subtracting off the reference state, and dividing by ρ_0 yields

$$\left(1 + \frac{\rho_E}{\rho_0}\right) \vec{u}_t + \nabla \cdot (\vec{u}^{\,T} \vec{u}) = -\frac{1}{\rho_0} \nabla p_E + \frac{\rho_E}{\rho_0} \vec{g} + \nu \nabla^2 \vec{u} \tag{2.6}$$

Since $\rho_E / \rho_0 \ll 1$ for small density variations, this reduces to

$$\vec{u}_t + \nabla \cdot (\vec{u}^{\,T} \vec{u}) = -\frac{1}{\rho_0} \nabla p_E + \frac{\rho_E}{\rho_0} \vec{g} + \nu \nabla^2 \vec{u}. \tag{2.7}$$

$$\tag{2.8}$$

For flows in which compressibility effects matter, the Boussinesq approximation cannot be applied. The Mach number, which describes the ratio of inertial to compressibility forces, is given by $M = U/c$ where U is the characteristic velocity of a flow and c is the speed of sound in the fluid medium. For $M < 0.3$, compressibility effects are negligible [52]. In water, attainable flow speeds are much less than the speed of sound, and so the incompressibility assumption is quite good. Further, so long as the vertical scale of the flow, L, satisfies the condition $L \ll c^2/g$, one need not consider compressibility effects due to hydrostatic pressure variations causing large density changes.

To summarize, under the Boussinesq approximation, the governing equations are

$$\vec{u}_t + \nabla \cdot (\vec{u}^T \vec{u}) = -\frac{1}{\rho_0}\nabla p + \frac{\rho_E}{\rho_0}\vec{g} + \nu\nabla^2\vec{u}, \tag{2.9}$$

$$\nabla \cdot \vec{u} = 0, \tag{2.10}$$

$$\frac{D\rho_E}{Dt} = \kappa_\rho \nabla^2 \rho_E \qquad \theta_t + \nabla \cdot (\vec{u}\theta) = \kappa\nabla^2\theta + F(\theta). \tag{2.11}$$

Note that we drop the subscript on the pressure term.

The numerical simulations presented later in this thesis are produced using the SPINS (Spectral Parallel Incompressible Navier–Stokes Solver) model [88] which solves the Navier-Stokes equations under the Boussinesq approximation and the ADR equation given above.

Herein, a scalar tracer undergoing a reaction and evolving according to equation 2.11 will be referred to as a reactive tracer. The term passive tracer will be used to refer to non-reactive, $F(\theta) = 0$, tracers. Both the reactive and passive tracers are passive in the fluid dynamical sense, meaning they do not affect the fluid flow. Reactive tracers are an important component in biophysical models describing ecosystem dynamics, which generally include components evolved by growth and interaction terms [11, 15, 36, 48, 77].

There are a number of forms for the reaction term that are used repeatedly in varying contexts. For example, the logistic equation, $\alpha\theta(1-\theta/K)$, is a popular choice for modelling population growth because it captures the concept of self-limitation [101, 99]. The model allows a population to grow with a maximum rate of α up to a value of K, the carrying capacity of the environment. Accounting for the saturation of resources within an environment is a clear improvement upon linear models, which allow for unlimited exponential growth. For this reason, reaction terms are non-linear more often than not. Fisher's equation [62], $F(\theta) = \theta(1-\theta)$, will be used as an illustrative example herein, but the procedure presented in what follows can be used to treat any reaction term expressed as (or approximated by) a polynomial. Fisher's equation provides a simple, non-linear reaction function and takes the same form as the logistic equation with α and K set to one.

As we will see in section 2.4.2, polynomial reaction functions are fairly straightforward to analyze despite being non-linear. Non-polynomial functions that are infinitely differentiable at a point a can be expressed as a Taylor series. Without loss of generality, we can take $a = 0$ and write

$$F(\theta) = \sum_{n=0}^{\infty} \frac{F^{(n)}(0)}{n!}\theta^n \tag{2.12}$$

so that $F(\theta)$ is locally represented by a polynomial. If we truncate the polynomial at some $n = N$, then if $F(\theta)$ is $N+1$ times differentiable on the interval $(0, \theta)$ and $F^{(N)}(\theta)$ is continuous on $[0, \theta]$ we can use Taylor's Theorem to express the difference between $F(\theta)$ and its degree N Taylor polynomial as a remainder

$$R_N(\theta) = F(\theta) - P_N(\theta) = \frac{F^{(N+1)}(\xi)}{(N+1)!}\theta^{N+1} \tag{2.13}$$

where $\xi \in (0, \theta)$. By placing a restriction on the size of the remainder, one can select an appropriate degree for the Taylor polynomial.

2.2 Non-Dimensionalization

Consider the one-dimensional Navier-Stokes momentum equation and let $u = \mathcal{U}\tilde{u}$, $z = L\tilde{z}$, $t = \tau\tilde{t}$, and $p = P\tilde{p}$ where tildes denote dimensionless variables. Substituting and dropping the tildes yields the following

$$\frac{\mathcal{U}}{\tau}u_t + \frac{\mathcal{U}^2}{L}uu_z = -\frac{P}{\rho_0 L}p_z + \frac{\rho_E}{\rho_0}G\hat{g} + \frac{\nu\mathcal{U}}{L^2}u_{zz}, \tag{2.14}$$

$$u_t + \frac{\mathcal{U}\tau}{L}uu_z = -\frac{P\tau}{\rho_0\mathcal{U}L}p_z + \frac{\rho_E}{\rho_0}\frac{GL}{\mathcal{U}^2}\hat{g} + \frac{\nu\tau}{L^2}u_{zz}, \tag{2.15}$$

$$u_t + uu_z = -p_z + \frac{\rho_E}{\rho_0}\frac{1}{Fr^2}\hat{g} + \frac{1}{Re}u_{zz}, \tag{2.16}$$

$$\tau = \frac{L}{\mathcal{U}}, \qquad P = \rho_0\mathcal{U}^2, \qquad Fr = \frac{\mathcal{U}}{\sqrt{GL}}, \qquad Re = \frac{\mathcal{U}L}{\nu} \tag{2.17}$$

where Fr is the Froude number, the square root of the ratio of inertial to gravitational forces, and Re is the Reynolds number defining the ratio of inertial to viscous forces.

In equation 2.11, we take θ to be a dimensionless quantity, though it will often be referred to as a (dimensionless) concentration is what follows for the sake of conceptualization. The reaction term is required to have units of time^{-1}. So, we add a rate parameter to Fisher's equation, $F(\theta) = \alpha\theta(1-\theta)$, with units $[\alpha] = 1/(\text{time})$ to satisfy the requirement.

Once again let $u = \mathcal{U}\tilde{u}$, $z = L\tilde{z}$, and $t = \tau\tilde{t}$. Substituting and dropping the tildes yields

$$\frac{1}{\tau}\theta_t + \frac{\mathcal{U}}{L}u\theta_z = \frac{\kappa}{L^2}\theta_{zz} + \alpha\theta(1-\theta), \tag{2.18}$$

$$\theta_t + \frac{\mathcal{U}\tau}{L}u\theta_z = \frac{\kappa\tau}{L^2}\theta_{zz} + \alpha\tau\theta(1-\theta). \tag{2.19}$$

We choose to set $\tau = \frac{L}{U}$ to retain a timescale consistent with that from the non-dimensionalization of the Navier-Stokes momentum equation. Substituting and simplifying we get

$$\theta_t + u\theta_z = \frac{\kappa}{UL}\theta_{zz} + \frac{\alpha L}{U}\theta(1-\theta), \tag{2.20}$$

$$\theta_t + u\theta_z = \frac{1}{Sc \cdot Re}\theta_{zz} + Da \cdot \theta(1-\theta), \tag{2.21}$$

$$Sc = \nu/\kappa, \qquad Da = \frac{\alpha L}{\mathcal{U}}, \tag{2.22}$$

where Sc is the Schmidt number, the ratio of momentum to mass diffusivity, and Da is the Damköhler number which gives the ratio of the reactive (α) to advective ($1/\tau$) timescales. Note that the definition of the Damköhler number depends on the context in which it is used and that we have made a choice as to how to formulate it. The characteristic length, time, and velocity scales will depend on the numerical simulation being considered and will be discussed in chapter 3.

2.3 Notation and Vocabulary

We will be considering how Reynolds averaging and the spatial filtering used to derive the equations for LES (referred to as LES filtering from this point onwards) affect the form of equation 2.11, paying particular attention to the reaction term. As will be shown in sections 2.4 and 2.5 the two methods produce similar equations and unknowns. It is therefore important to outline the fundamental differences between the two approaches, and to keep these differences in mind throughout the rest of this chapter.

Reynolds averaging consists of taking the *average over an ensemble* and will be denoted with an overbar. The differences between each ensemble member and the ensemble average are defined as fluctuations. Applying a Reynolds decomposition to an ensemble member consists of expressing it as the sum of a slowly varying mean part (the ensemble average) and fluctuations about the mean. As an example, the horizontal velocity component of a fluid can be expressed as $u(\vec{x},t) = U(\vec{x},t) + u'(\vec{x},t)$ where $U(\vec{x},t) = \overline{u(\vec{x},t)}$ is the mean

and $u'(\vec{x},t) = u(\vec{x},t) - U(\vec{x},t)$ captures the fluctuations with $\overline{u'(\vec{x},t)} = 0$. Throughout this thesis, capitalized variables will correspond to mean values and primes will denote fluctuations (except when used in the filtered equations).

Where Reynolds averaging requires an ensemble of data, the spatial filtering associated with LES only requires one ensemble member. LES filtering a physical quantity removes all sub-filter-scale features leaving only the resolved data. Grid resolution determines what is resolved in a numerical simulation and what is ignored. Similarly, the length scale associated with an LES filter determines which features in a dataset are retained. Angled brackets will be used to denote filtered quantities, $\langle u(\vec{x},t)\rangle$ and sub-filter-scale quantities will be denoted with primes, $u'(\vec{x},t) = u(\vec{x},t) - \langle u(\vec{x},t)\rangle$.

Filtering can be thought of as taking a running mean in space, with the filter scale setting the distance over which the average is taken. This inevitably smooths (smears) the features observed in a single simulation. A Reynolds average can be interpreted as a single spatial point average, since it does not introduce any interdependence between values at different spatial points. Rather, the Reynolds average at a spatial point is simply the average of the values of the ensemble members at that same point.

2.4 Reynolds Averaging

2.4.1 Reynolds Averaging the Governing Equations

We begin by decomposing the velocity field into a slowly varying mean part, $\vec{U}$, and a rapidly fluctuating part, $\vec{u}'$, so that $\vec{u} = \vec{U} + \vec{u}'$ with $\overline{\vec{u}} = \vec{U}$ and $\overline{\vec{u}'} = 0$. Similarly, for the pressure and excess density we have $p = P + p'$ and $\rho_E = \mathcal{P}_E + \rho'_E$. Substituting the Reynolds decompositions into equation 2.9 and then Reynolds averaging yields the Reynolds averaged momentum equation,

$$\vec{U}_t + \nabla\cdot(\vec{U}^{\,T}\vec{U}) = -\frac{1}{\rho_0}\nabla P + \frac{\mathcal{P}_E}{\rho_0}\vec{g} + \nu\nabla^2\vec{U} - \nabla\cdot\overline{\vec{u}'^{T}\vec{u}'}. \tag{2.23}$$

The Reynolds stress tensor describes the effects of the fluctuations on the mean flow and is defined as $R_{ij} = \overline{u'_i u'_j}$. Note that here we are assuming $\vec{u}$ is a row vector.

The procedure can be applied to equation 2.11 by applying a Reynolds decomposition to the tracer field, $\theta = \Theta + \theta'$. Following the same procedure, the Reynolds averaged ADR

equation is

$$\Theta_t + \nabla \cdot (\vec{U}\Theta) = \kappa \nabla^2 \Theta + \overline{F(\Theta + \theta')} - \nabla \cdot \overline{\vec{u}'\theta'}, \tag{2.24}$$

where $\overline{\vec{u}'\theta'}$ is the eddy flux, representing the transport of tracer fluctuations by fluctuations in the velocity field. The treatment of the $\overline{F(\Theta + \theta')}$ term will be considered in section 2.4.2.

2.4.2 Reynolds Averaging $F(\theta)$

Consider a polynomial reaction function of degree N. We want to rewrite each term, $\overline{\theta^n}$ with $n \leq N$, in a way that allows us to separate the effects due to the mean tracer field, those due to fluctuations, and those due to interactions of the two. By substituting $\theta = \Theta + \theta'$, the reactions can be binned as follows

$$\overline{\theta^n} = \overline{(\Theta + \theta')^n} \tag{2.25}$$

$$= \sum_{\alpha_1+\alpha_2=n;\ \alpha_1,\alpha_2\geq 0} \binom{n}{\alpha_1, \alpha_2} \overline{\Theta^{\alpha_1}(\theta')^{\alpha_2}} \tag{2.26}$$

$$= \Theta^n + \underbrace{\sum_{\alpha_1+\alpha_2=n;\ \alpha_1>0\ \alpha_2>1} \binom{n}{\alpha_1, \alpha_2} \Theta^{\alpha_1} \overline{(\theta')^{\alpha_2}}}_{I_n} + \underbrace{\overline{(\theta')^n}}_{S_n}. \tag{2.27}$$

The scalar quantity I_n represents the interactions between the mean tracer field and the fluctuations. Correlations between the fluctuations are quantified through S_n with S_2 being the scalar variance of the tracer. Note that $I_n = 0$ for $n < 3$ and $S_n = 0$ for $n < 2$ since $\overline{\theta'} = 0$ and a constant function ($n = 0$) does not have a fluctuating part.

The Reynolds averaged reaction term can be written as

$$\overline{F(\theta)} \approx \sum_{n=0}^{N} \frac{F^{(n)}(0)}{n!} \Theta^n + \sum_{n=3}^{N} \frac{F^{(n)}(0)}{n!} I_n + \sum_{n=2}^{N} \frac{F^{(n)}(0)}{n!} S_n. \tag{2.28}$$

Note that this expression can be used to treat both polynomial reaction functions and Taylor polynomial approximations of degree N taken around $\theta = 0$. The expression can be modified for Taylor polynomials taken around a point $\theta = a$ by evaluating the coefficients at a (rather than at zero as is written above) and substituting $(\Theta - a)$ anywhere Θ appears.

If one wanted to find an evolution equation for the fluctuations, the reaction term would

take the following form

$$F(\theta)' = F(\theta) - \overline{F(\theta)} = \sum_{n=0}^{N} \frac{F^{(n)}(0)}{n!}(\theta^n - \Theta^n) - \sum_{n=3}^{N} \frac{F^{(n)}(0)}{n!} I_n - \sum_{n=2}^{N} \frac{F^{(n)}(0)}{n!} S_n. \quad (2.29)$$

For Fisher's equation, the Reynolds averaged and fluctuation reaction terms can be expressed as follows

$$\overline{F(\theta)} = \Theta(1-\Theta) - \overline{(\theta')^2}, \quad (2.30)$$

$$F(\theta)' = \theta'(1-\theta') + \overline{(\theta')^2} - 2\Theta\theta'. \quad (2.31)$$

The scalar variance, $S_2 = \overline{(\theta')^2}$, is strictly non-negative and therefore acts as a sink in the Reynolds averaged equation and a source in the fluctuation equation.

If the tracer in question must have non-negative values everywhere in its domain (concentration, population, etc.), then its mean must also be non-negative. However, there is no such restriction on the fluctuations, the signs of which depend on the spatial distribution of each ensemble member relative to the mean. Fluctuations will be negative (positive) anywhere an ensemble member has less (more) tracer than the mean. At these locations, the sign of $-2\Theta\theta'$ is opposite that of θ' and so this term drives the fluctuations towards 0. However, it must compete with $F(\theta')$ which drives $\theta' \to 1$ if $\theta' > 0$ and $\theta' \to -\infty$ if $\theta' < 0$ as well as S_2 which drives $\theta' \to \infty$.

The Reynolds averaged ADR (RAADR) equation is

$$\Theta_t + \nabla \cdot (\vec{u}\Theta) = \kappa \nabla^2 \Theta + \Theta(1-\Theta) - \overline{(\theta')^2} - \nabla \cdot \overline{\vec{u}'\theta'}, \quad (2.32)$$

and the ADR equation describing the evolution of the fluctuations is

$$\theta'_t + \nabla \cdot (\vec{U}\theta' + \vec{u}'\Theta) + \nabla \cdot (\vec{u}'\theta' - \overline{\vec{u}'\theta'}) = \kappa \nabla^2 \theta' + \theta'(1-\theta') + \overline{(\theta')^2} - 2\Theta\theta'. \quad (2.33)$$

We note that the equation for the fluctuations is often multiplied by θ' and averaged to produce an equation for the scalar variance [109]. However, with Fisher's equation as the reaction term, this would result in triple correlations of the form $\overline{(\theta')^3}$, posing another closure problem. Since our numerical simulations provide sufficient data and resolution to treat the fluctuations directly, we consider an equation for the fluctuations.

2.5 Spatial Filtering for LES

We denote spatial filtering with angled brackets, $\langle\theta\rangle$, and the sub-filter-scale quantities with primes, θ'. Filtering is applied by taking the convolution of a quantity with a filter function, $G(\vec{x})$

$$\langle\theta(\vec{x},t)\rangle = \iiint_{-\infty}^{\infty} G(\vec{x}-\vec{s})\theta(\vec{s})d\vec{s}. \tag{2.34}$$

By taking the Fourier transform of a filter in physical space, we can define an equivalent filter in spectral space

$$\hat{G}(\vec{k}) = \iiint_{-\infty}^{\infty} \exp(i\vec{k}\cdot\vec{x})G(\vec{x})d\vec{x}. \tag{2.35}$$

Wavenumbers are denoted $\vec{k} = (k,l,m)$. Filtering in spectral space is advantageous for a number of reasons. For one, filtering in spectral space consists of simply performing multiplication

$$\langle\hat{\theta}(\vec{k},t)\rangle = \hat{\theta}(\vec{k},t)\hat{G}(\vec{k}). \tag{2.36}$$

From a conceptual standpoint, considering a dataset in terms of its spatial frequencies makes it easier to understand the relevant active length scales. It also makes it easier to cleanly separate a dataset into low frequency (resolved) and high frequency (sub-filter-scale) parts. Low-pass filters which employ a hard cutoff allow for a perfect separation and take the form

$$\hat{G}(\vec{k}) = \begin{cases} 1, & |k_i| < k_i^{cut} \\ 0, & |k_i| \geq k_i^{cut} \end{cases} \tag{2.37}$$

where k_i^{cut} is the wavenumber cutoff [109]. Since wavenumbers are inversely proportional to wavelengths, a low-pass filter only retains features with wavelengths larger than that corresponding to the wavenumber cutoff.

Fourier transforms allow us to express a periodic quantity in spectral space through its Fourier series.

$$\theta(\vec{x},t) = \sum_{n=-\infty}^{n=\infty} \hat{\theta}(\vec{k}_n,t)\exp(i\vec{k}_n\cdot\vec{x}) \tag{2.38}$$

where $\hat{\theta}(\vec{k}_n, t)$ is a coefficient that needs to be solved for. For a triply-periodic variable we have

$$\hat{\theta}(\vec{k}_n, t) = \frac{1}{P_x P_y P_z} \int_{-P_x/2}^{P_x/2} \int_{-P_y/2}^{P_y/2} \int_{-P_z/2}^{P_z/2} \theta(\vec{x}, t) \exp(-i\vec{k}_n \cdot \vec{x}) d\vec{x} \tag{2.39}$$

where P_x is the period in x, $k_n = 2\pi n / P_x$, and similarly for y and l, and z and m.

When we apply a spectral filter to the Fourier series we get

$$\sum_{n=-\infty}^{n=\infty} \hat{G}(\vec{k}_n) \hat{\theta}(\vec{k}_n, t) \exp(i\vec{k}_n \cdot \vec{x}). \tag{2.40}$$

For a low-pass filter with wave-cutoff $\vec{k}^{cut} = (k_Q, l_R, m_S)$ this simplifies to

$$\sum_{q=-Q}^{q=Q} \sum_{r=-R}^{r=R} \sum_{s=-S}^{s=S} \hat{\theta}((k_q, l_r, m_s), t) \exp(i(k_q, l_r, m_s) \cdot \vec{x}). \tag{2.41}$$

so that we have effectively truncated the series and only the large-scale components remain.

2.5.1 Filtering the Governing Equations

When a spatial filter is applied to a physical quantity, whatever is removed by the filter constitutes the sub-filter-scale (**sfs**) part of the quantity. We will denote resolved components with angled brackets and **sfs** components with primes. For a velocity field, we have $\vec{u}' = \vec{u} - \langle \vec{u} \rangle$. Rearranging, we can decompose the velocity field in terms of the two components so that $\vec{u} = \langle \vec{u} \rangle + \vec{u}'$. This looks similar in form to a Reynolds decomposition. In both cases, we are taking physical quantities to be the sum of some known (mean or resolved) component and an unknown (fluctuation or **sfs**) component. Note that while $\overline{U} = U$ for Reynolds averaging, the relationship between $\langle \langle \vec{u} \rangle \rangle$ and $\langle \vec{u} \rangle$ depends on the form of the spatial filter used. The order of operations for deriving the filtered Navier-Stokes equations is not the same as that for obtaining the RANS equations. We do not substitute $\vec{u} = \langle \vec{u} \rangle + \vec{u}'$ into equation 2.9. Instead, we apply the filter to the equation directly. Note that the filtering operation commutes with differentiation.

$$\langle \vec{u} \rangle_t + \nabla \cdot \langle \vec{u}^T \vec{u} \rangle = -\frac{1}{\rho} \nabla \langle p \rangle + \frac{\langle \rho_E \rangle}{\rho_0} \vec{g} + \nu \nabla^2 \langle \vec{u} \rangle \tag{2.42}$$

$$\langle \vec{u} \rangle_t + \nabla \cdot (\langle \vec{u} \rangle^T \langle \vec{u} \rangle) = -\frac{1}{\rho} \nabla \langle p \rangle + \frac{\langle \rho_E \rangle}{\rho_0} \vec{g} + \nu \nabla^2 \langle \vec{u} \rangle - \nabla \cdot (\langle \vec{u}^T \vec{u} \rangle - \langle \vec{u} \rangle^T \langle \vec{u} \rangle) \tag{2.43}$$

The second term on the LHS is the result of adding and subtracting $\nabla \cdot \langle \vec{u} \rangle^T \langle \vec{u} \rangle$. By doing so, we have recovered the form of the NS equations in terms of only the resolved velocity. However, we have also introduced the residual stress tensor $\tau_{ij}^{LES} = \langle \vec{u}^T \vec{u} \rangle - \langle \vec{u} \rangle^T \langle \vec{u} \rangle$. We can rewrite the tensor by substituting $\vec{u} = \langle \vec{u} \rangle + \vec{u}\,'$ as follows

$$\tau_{ij}^{LES} = \langle (\langle u_i \rangle + u_i')(\langle u_j \rangle + u_j') \rangle - \langle u_i \rangle \langle u_j \rangle \tag{2.44}$$

$$\tau_{ij}^{LES} = \underbrace{\langle \langle u_i \rangle \langle u_j \rangle \rangle - \langle u_i \rangle \langle u_j \rangle}_{L_{ij}} + \underbrace{\langle \langle u_i \rangle u_j' + u_i' \langle u_j \rangle \rangle}_{C_{ij}} + \underbrace{\langle u_i' u_j' \rangle}_{R_{ij}} \tag{2.45}$$

$$\tau_{ij}^{LES} = L_{ij} + C_{ij} + R_{ij} \tag{2.46}$$

Using the substitution allows us to re-express the residual stress tensor in terms of three sub-tensors. The resolved interactions are grouped into L_{ij}, termed the Leonard tensor or sub-grid stress tensor. The sub-filter scale interactions are contained in R_{ij}, the Reynolds stress-like tensor (not to be confused with the Reynolds stress tensor from the RANS equations). The cross-scale interactions are grouped in the Clark tensor, C_{ij}.

The filtered incompressible Navier-Stokes equations are

$$\langle \vec{u} \rangle_t + \nabla \cdot (\langle \vec{u} \rangle^T \langle \vec{u} \rangle) = -\frac{1}{\rho} \nabla \langle p \rangle + \frac{\langle \rho_E \rangle}{\rho_0} \vec{g} + \nu \nabla^2 \langle \vec{u} \rangle - \nabla \cdot \tau^{LES} \tag{2.47}$$

$$\nabla \cdot \langle \vec{u} \rangle = 0 \tag{2.48}$$

Let us now perform the same procedure on the ADR equation for the reactive tracer 2.11.

$$\langle \theta \rangle_t + \nabla \cdot \langle \vec{u} \theta \rangle = \kappa \nabla^2 \langle \theta \rangle + \langle F(\theta) \rangle \tag{2.49}$$

$$\langle \theta \rangle_t + \nabla \cdot \langle \vec{u} \theta \rangle - \nabla \cdot (\langle \vec{u} \rangle \langle \theta \rangle) + \nabla \cdot (\langle \vec{u} \rangle \langle \theta \rangle) = \kappa \nabla^2 \langle \theta \rangle + \langle F(\theta) \rangle \tag{2.50}$$

$$\langle \theta \rangle_t + \nabla \cdot (\langle \vec{u} \rangle \langle \theta \rangle) = \kappa \nabla^2 \langle \theta \rangle - \nabla \cdot (\langle \vec{u} \theta \rangle - \langle \vec{u} \rangle \langle \theta \rangle) + \langle F(\theta) \rangle \tag{2.51}$$

Note that we added and subtracted $\nabla \cdot (\langle \vec{u} \rangle \langle \theta \rangle)$ to obtain an ADR equation of the same form but in terms of resolved quantities. The non-linearity of the advection term introduces a

sfs flux term that we define as $\vec{f}^A = \langle\vec{u}\theta\rangle - \langle\vec{u}\rangle\langle\theta\rangle$. Substituting the decompositions $\vec{u} = \langle\vec{u}\rangle + \vec{u}\,'$ and $\theta = \langle\theta\rangle + \theta'$, we can reformulate $\vec{f}^A$ as follows

$$\begin{aligned}
\vec{f}^A &= \langle\vec{u}\theta\rangle - \langle\vec{u}\rangle\langle\theta\rangle && (2.52)\\
&= \langle(\langle\vec{u}\rangle + \vec{u}\,')(\langle\theta\rangle + \theta') - \langle\vec{u}\rangle\langle\theta\rangle && (2.53)\\
&= \underbrace{\langle\langle\vec{u}\rangle\langle\theta\rangle\rangle - \langle\vec{u}\rangle\langle\theta\rangle}_{\vec{L}^A} + \underbrace{\langle\langle\vec{u}\rangle\theta' + \vec{u}\,'\langle\theta\rangle\rangle}_{\vec{C}^A} + \underbrace{\langle\vec{u}\,'\theta'\rangle}_{\vec{R}^A} && (2.54)
\end{aligned}$$

Note that the A superscripts indicate that these are advective terms. The expression for $\vec{f}^A$ is similar in form to that for the residual stress tensor. The $\vec{L}^A$ component contains the **sfs** portion of the transport of the resolved part of the tracer, $\langle\theta\rangle$, by the resolved velocity field, $\langle\vec{u}\rangle$. The other components, $\vec{C}^A$ and $\vec{R}^A$, represent the cross-scale and sub-filter scale interactions, respectively. The filtered ADR equation can thus be written as follows

$$\langle\theta\rangle_t + \nabla\cdot(\langle\vec{u}\rangle\langle\theta\rangle) = \kappa\nabla^2\langle\theta\rangle - \nabla\cdot\vec{f}^A + \langle F(\theta)\rangle. \tag{2.55}$$

The treatment of $\langle F(\theta)\rangle$ will be discussed in section 2.5.2

2.5.2 Filtering $F(\theta)$

When filtering a degree N polynomial, we can filter each term individually so that

$$\langle F(\theta)\rangle = \left\langle \sum_{n=0}^{N} \frac{F^{(n)}(0)}{n!}\theta^n \right\rangle = \sum_{n=0}^{N} \frac{F^{(n)}(0)}{n!}\langle\theta^n\rangle\,. \tag{2.56}$$

For consistency, we wish to express $\langle \theta^n \rangle$ in terms of a decomposition with the same form as those for the residual stress tensor and **sfs** flux term. Consider the following

$$\langle \theta^n \rangle = \langle (\langle \theta \rangle + \theta')^n \rangle, \tag{2.57}$$

$$= \sum_{\alpha_2+\alpha_2=n;\ \alpha_1,\alpha_2 \geq 0} \binom{n}{\alpha_1, \alpha_2} \langle \langle \theta \rangle^{\alpha_1} (\theta')^{\alpha_2} \rangle, \tag{2.58}$$

$$= \sum_{\alpha_2+\alpha_2=n;\ \alpha_1,\alpha_2 > 0} \binom{n}{\alpha_1, \alpha_2} \langle \langle \theta \rangle^{\alpha_1} (\theta')^{\alpha_2} \rangle + \langle \langle \theta \rangle^n \rangle + \langle (\theta')^n \rangle, \tag{2.59}$$

$$= \langle \theta \rangle^n + \underbrace{\langle \langle \theta \rangle^n \rangle - \langle \theta \rangle^n}_{L_n^R} + \underbrace{\sum_{\alpha_2+\alpha_2=n;\ \alpha_1,\alpha_2 > 0} \binom{n}{\alpha_1, \alpha_2} \langle \langle \theta \rangle^{\alpha_1} (\theta')^{\alpha_2} \rangle}_{C_n^R} + \underbrace{\langle (\theta')^n \rangle}_{R_n^R}. \tag{2.60}$$

We define scalar quantities L_n^R, C_n^R, and R_n^R to describe the resolved scale, cross-scale, and sub-filter scale portions of this expression. The R superscript identifies them as contributions to the reaction term. Let $f_n^R = L_n^R + C_n^R + R_n^R$ so that we have defined a **sfs** reaction term with a form analogous to that of the **sfs** fluxes. Note that f_n^R is zero for $n < 2$.

Using f_n^R, we can express a degree N polynomial reaction function as

$$\langle F(\theta) \rangle = \sum_{n=0}^{N} \frac{F^{(n)}(0)}{n!} \langle \theta^n \rangle = \sum_{n=0}^{N} \frac{F^{(n)}(0)}{n!} \langle \theta \rangle^n + \sum_{n=2}^{N} \frac{F^{(n)}(0)}{n!} f_n^R. \tag{2.61}$$

For Fisher's equation, $F(\theta) = \theta(1-\theta)$, the filtered reaction term is

$$\langle F(\theta) \rangle = \langle \theta \rangle - \langle \theta^2 \rangle = \underbrace{\langle \theta \rangle - \langle \theta \rangle^2}_{F(\langle \theta \rangle)} - \underbrace{(\langle \langle \theta \rangle^2 \rangle - \langle \theta \rangle^2)}_{L_2^R} - \underbrace{2\langle \langle \theta \rangle \theta' \rangle}_{C_2^R} - \underbrace{\langle (\theta')^2 \rangle}_{R_2^R}. \tag{2.62}$$

The R_2^R term acts as a sink in the filtered reaction equation similarly to how the fluctuations formed a sink in the Reynolds averaged reaction. The contributions of the L_2^R and C_2^R terms are not as straightforward to interpret.

To summarize, the filtered ADR equation with Fisher's equation describing the reaction is

$$\langle \theta \rangle_t + \nabla \cdot (\langle \vec{u} \rangle \langle \theta \rangle) = \kappa \nabla^2 \langle \theta \rangle + \langle \theta \rangle (1 - \langle \theta \rangle) - \nabla \cdot \vec{f}^A - f^R \tag{2.63}$$

2.6 Summary of Equations

For the reader's convenience and for ease of comparison, the Reynolds averaged and filtered governing equations are summarized in this section. The RANS equations under the Boussinesq approximation are

$$\vec{U}_t + \nabla \cdot (\vec{U}^{\,T}\vec{U}) = -\frac{1}{\rho_0}\nabla P + \frac{\mathcal{P}_E}{\rho_0}\vec{g} + \nu\nabla^2\vec{U} - \nabla \cdot R, \tag{2.64}$$

$$\nabla \cdot \vec{U} = 0. \tag{2.65}$$

The Reynolds averaged energy equation is

$$\frac{D\mathcal{P}_\mathcal{E}}{Dt} = \kappa_\rho \nabla^2 \mathcal{P}_E, \tag{2.66}$$

and the Reynolds averaged ADR equation with Fisher's equation as the reaction is

$$\Theta_t + \nabla \cdot (\vec{U}\Theta) = \kappa\nabla^2\Theta - \nabla \cdot \overline{\vec{u}'\theta'} + \Theta(1-\Theta) - \overline{(\theta')^2}. \tag{2.67}$$

The filtered incompressible Navier-Stokes equations under the Boussinesq approximation are

$$\langle\vec{u}\rangle_t + \nabla \cdot (\langle\vec{u}^{\,T}\rangle\langle\vec{u}\rangle) = -\frac{1}{\rho}\nabla\langle p\rangle + \frac{\langle\rho_E\rangle}{\rho_0}\vec{g} + \nu\nabla^2\langle\vec{u}\rangle - \nabla \cdot \tau^{LES}, \tag{2.68}$$

$$\nabla \cdot \langle\vec{u}\rangle = 0. \tag{2.69}$$

The filtered energy equation is

$$\frac{D\langle\rho_E\rangle}{Dt} = \kappa_\rho \nabla^2\langle\rho_E\rangle \tag{2.70}$$

and the filtered ADR equation with Fisher's equation as the reaction is

$$\langle\theta\rangle_t + \nabla \cdot (\langle\vec{u}\rangle\langle\theta\rangle) = \kappa\nabla^2\langle\theta\rangle + \langle\theta\rangle(1-\langle\theta\rangle) - \nabla \cdot \vec{f}^A - f^R, \tag{2.71}$$

$$\vec{f}^A = (\langle\langle\vec{u}\rangle\langle\theta\rangle\rangle - \langle\vec{u}\rangle\langle\theta\rangle) + \langle\langle\vec{u}\rangle\theta' + \vec{u}'\langle\theta\rangle\rangle + \langle\vec{u}'\theta'\rangle, \tag{2.72}$$

$$f^R = (\langle\langle\theta\rangle^2\rangle - \langle\theta\rangle^2) + 2\langle\langle\theta\rangle\theta'\rangle + \langle(\theta')^2\rangle. \tag{2.73}$$

Filtering the governing equations produces more complex expressions for the unknown terms (in the sense that there are more components to account for) than Reynolds aver-

aging. Based on this fact alone, one might be tempted to hypothesize that LES provides a weaker representation of a reactive tracer evolving in a turbulent flow. However, this is not necessarily true, as the two methods are conceptually quite different. This discussion point will be revisited throughout what follows.

Chapter 3

Numerical Methods

This chapter presents the numerical methods used to generate and analyze the data considered in Chapters 4, 5 and 6. Section 3.1 discusses the relationship between spatial filtering and the effective resolution of a simulation, in addition to briefly addressing some of the challenges posed by aliasing. In Section 3.2, the Spectral Incompressible Navier Stokes Solver is introduced. The model is later used to generate the ensemble of 50 two-dimensional Rayleigh-Taylor instabilities (see Section 5.1) and a high-resolution three-dimensional Rayleigh-Taylor simulation (see Section 6.2.1). The solver presented in Section 3.3 is used to generate the toy model results presented in Chapter 4 and Section 6.1.

3.1 Filtering in Spectral Space, Resolution, and Aliasing

For computational convenience, all spatial filtering was performed in spectral space. Recall that the filtering operation as defined in Chapter 2 involved a convolution in physical space. By filtering in spectral space, we eliminate the need for numerical integration and instead use multiplication alongside the fast Fourier transform, well-known for its efficiency.

The resolution of a numerical simulation determines the smallest wavelength (largest wavenumber) that can be resolved. To resolve a wave with wavelength λ and wavenumber $k = 2\pi/\lambda$ the distance between grid points cannot exceed $\lambda/2$ [95]. The wavenumbers that can be resolved on a grid with spacing dx lie in the interval $[-k^{nyq}, k^{nyq}]$ where $k^{nyq} = \pi/dx$ is the Nyquist frequency. Each wavenumber, k, within this interval has infinitely many

aliases given by $\tilde{k} = k + 2\pi m/dx$ where m is an integer. For two functions to be aliases of one another, they must have the same value at each grid point.

Applying low-pass spatial filtering with a cutoff wavenumber, $k^{cut} < k^{nyq}$ enlarges the smallest wavelength that can be resolved. The reduced resolution associated with the cutoff wavenumber is $\Delta = \pi/k^{cut}$ where $\Delta > dx$. Suppose you ran a simulation with resolution $dx = L/N$ (with L being the width of the domain and N the number of grid points) and want to know what information you would lose should the grid spacing increase by an order of magnitude. Then the appropriate cutoff for your *a priori* LES analysis can be determined by setting $\Delta_x = 10dx$ and solving for $k^{cut} = \pi/\Delta_x$. However, it is important to note that if you were to compare data from a low-resolution simulation with data from a high-resolution simulation that had been low-pass filtered to a resolution equivalent to that of the low-resolution data there may still be differences. In part, these differences could be due to aliasing errors that might accumulate in the low-resolution data more readily than in the high-resolution data.

If $u(x)$ is a smooth function with a bounded first derivative and $v(x)$ is its representation on the discrete grid, $v_j = u(x_j)$, then from the aliasing theorem the error is [95]

$$\hat{v}(k) - \hat{u}(k) = \sum_{j=-\infty, j\neq 0}^{\infty} \hat{u}\left(k + \frac{2\pi j}{dx}\right). \tag{3.1}$$

In a low resolution simulation, the spectral power associated with unresolvable wavenumbers is attributed (erroneously) to their resolvable aliases (de-aliasing techniques may mitigate these errors). Under low-pass filtering, the spectral power contained in wavenumbers greater than k^{cut} is removed from the system entirely. The generation of high wavenumbers results from non-linear terms in the governing equations. Therefore, even simulations with initial conditions containing only resolvable wavenumbers will eventually develop unresolvable wavenumbers.

The spectral power of smoother functions is concentrated around lower wavenumbers. Therefore, aliasing errors are reduced for smoother functions. When simulating physical distributions with spectral or pseudospectral methods, the stability of the scheme relies upon the distributions remaining sufficiently smooth. Diffusion and viscosity play important roles in maintaining the stability of such schemes, and in practice large diffusivity and viscosity values may be used to compensate for coarse grid resolution. More details are provided in section 4.2. In general, even the orders of magnitude of viscosity values taken from various parameterizations differ between studies. See [103, 9, 26] for examples of how viscosity parametrizations might be implemented.

3.2 SPINS

The pseudospectral model SPINS was used to perform direct numerical simulations of the Rayleigh-Taylor instability. The model uses third-order accurate, variable time step Adams-Bashforth time-stepping and has spectral accuracy in space. When compared to lower order finite difference or volume schemes with the same resolution, numerical errors are much smaller [95]. Further, the numerical dispersion and diffusion errors often found in classical lower order methods are absent from spectral methods. The SPINS code has been extensively validated against linear theory (e.g., growth rate for shear instability and internal wave generation [88]), existing numerical methods (e.g., in the context of dipole–wall collisions [88]), exact solutions (e.g., for the propagation of exact internal solitary waves [40]), and experimental data (e.g., cross-boundary layer transport due to shoaling mode 2 internal waves [23]).

SPINS solves the Navier-Stokes equations under the Boussinesq approximation and a scalar transport equation for density.

$$\vec{u}_t + \nabla \cdot (\vec{u}^{\,T}\vec{u}) = -\frac{1}{\rho_0}\nabla p + \frac{\rho_E}{\rho_0}\vec{g} + \nu\nabla^2\vec{u}, \tag{3.2}$$

$$\nabla \cdot \vec{u} = 0, \tag{3.3}$$

$$\rho_t + \vec{u} \cdot \ \nabla\rho = \kappa_\rho \nabla^2 \rho. \tag{3.4}$$

Here $\vec{u}$ is the velocity field, p is the pressure, $\rho_0 = 1000$ kg/m^3 is the reference density, $\rho_E = \rho - \rho_0$ is the excess density, and $\vec{g} = 9.81$ m/s^2 $\hat{z}$ is the gravitational acceleration. The viscosity of water is $\nu = 1 \times 10^{-6}$ and the diffusivity of density is taken to be $\kappa_\rho = 1 \times 10^{-6}$ so that $Pr = \nu/\kappa_\rho = 1$.

In this work, SPINS is extended to solve a scalar transport equation for a reactive tracer

$$\theta_t + \nabla \cdot (\vec{u}\theta) = \kappa\nabla^2\theta + F(\theta) \tag{3.5}$$

where θ is a dimensionless reactive tracer concentration and $F(\theta) = \alpha\theta(1-\theta)\tanh(\theta/0.001)$ with $\alpha = 0.1$. We take $\kappa = 1 \times 10^{-6}$ so that $\nu/\kappa = 1$. The reaction term is a modification of Fisher's equation, chosen because it is both simple and non-linear. The multiplication by a hyperbolic tangent ensures that if any oscillations around $\theta = 0$ develop due to the numerical scheme, any points with $\theta < 0$ will be pushed back to $\theta = 0$.

SPINS minimizes numerical errors due to unresolved scales and aliasing through the

implementation of an exponential filter [14]. The filter takes the form

$$\hat{G}_{\text{SPINS}}(k) = \begin{cases} 1, & \text{if } |k| \leq k^{cut} \\ \exp\left(-\alpha\left(\frac{|k|-k_{cut}}{k^{nyq}-k^{cut}}\right)^{\beta}\right), & \text{otherwise} \end{cases} \tag{3.6}$$

for each component of $\vec{k}$. The filter has parameters k^{cut}, α (filter strength at k^{nyq}), and β (falloff order after k^{cut}) with default values $k^{cut} = 0.6k^{nyq}$, $\alpha = 2$, $\beta = 20$ [88]. The filter is applied to all velocity components and all tracers at each time step. In Chapter 6, we will consider the implications of various filter choices and touch upon the SPINS filter in the discussion.

In Chapter 5, SPINS is used to generate an ensemble of two-dimensional simulations. The simulations are initialized with an unstable density stratification so that RT instabilities develop. Reactive and passive tracers are evolved through the scalar transport equation above, with $F(\theta) = 0$ for the passive tracer. More details are provided in section 5.1. In Chapter 6, the two-dimensional setup is extended and a three-dimensional RT simulation is run with reactive and passive tracers. Details can be found in section 6.2.1.

3.3 Explicit-Implicit Euler's Method Solver in Fourier Space

Throughout this thesis, toy models are used to illustrate important concepts in a controlled manner. These models have prescribed velocity fields, so only the ADR equation for θ needs to be solved. The numerical method we use to do so treats the advection and reaction terms explicitly and handles diffusion implicitly. Equation 2.11 is solved using a discretization in Fourier space and the solution is transformed back into physical space at each timestep.

The update equation is obtained as follows. First, we take the Fourier transform of equation 2.11, denoted by tildes. Note that we only use this method in at most two dimensions (the $x - z$ plane).

$$\theta_t + \nabla \cdot \vec{u}\theta = \kappa\nabla^2\theta + F(\theta), \tag{3.7}$$

$$\widetilde{\theta}_t + i(k,m) \cdot \widetilde{\vec{u}\theta} = -\kappa(k^2+m^2)\widetilde{\theta} + \widetilde{F(\theta)}. \tag{3.8}$$

Discretizing in time and treating the advection and reaction terms implicitly and the

diffusion term explicitly yields

$$\frac{\widetilde{\theta^{n+1}} - \widetilde{\theta^n}}{\Delta t} + ik\widetilde{u\theta^n} + im\widetilde{w\theta^n} = -\kappa(k^2+m^2)\widetilde{\theta^{n+1}} + \widetilde{F(\theta^n)}, \tag{3.9}$$

$$\frac{\widetilde{\theta^{n+1}} - \widetilde{\theta^n}}{\Delta t} + \kappa(k^2+m^2)\widetilde{\theta^{n+1}} = -ik\widetilde{u\theta^n} - im\widetilde{w\theta^n} + \widetilde{F(\theta^n)}, \tag{3.10}$$

$$(1+\Delta t\kappa(k^2+m^2))\widetilde{\theta^{n+1}} = \widetilde{\theta^n} + \Delta t(-ik\widetilde{u\theta^n} - im\widetilde{w\theta^n} + \widetilde{F(\theta^n)}), \tag{3.11}$$

$$\widetilde{\theta^{n+1}} = \frac{1}{1+\Delta t\kappa(k^2+m^2)}\left(\widetilde{\theta^n} + \Delta t(-ik\widetilde{u\theta^n} - im\widetilde{w\theta^n} + \widetilde{F(\theta^n)})\right). \tag{3.12}$$

To recover the solution in physical space, we simply take the inverse fast Fourier transform.

To consider the stability of the numerical scheme, let us reduce the system to one dimension, assume u to be constant, assume $F(\theta) = 0$, and take the norm of both sides.

$$|\widetilde{\theta^{n+1}}| = \frac{\sqrt{1+\Delta t^2k^2u^2}}{1+\Delta t\kappa k^2}|\widetilde{\theta^n}| \tag{3.13}$$

The relative sizes of Δt, u, and κ govern the stability of the numerical scheme. The timestep, Δt must be chosen such that the amplification factor on the right-hand side is less than one. Small diffusivity values can lead to instability, especially if paired with relatively large velocities. The addition of a non-zero reaction term would inevitably affect the stability as well. For Fisher's equation with $\theta \in [0,1]$, $F(\theta) = \theta(1-\theta) \geq 0$ so the reaction term increases the magnitude of the right-hand side.

Euler's method is well-known to be a first order method and prone to stability issues. In our toy models, values of κ, Δt, and u were selected with this in mind. Concerns over using such a low order method for our toy models are valid, though in practice unnecessary since the toy models were re-run using Strang Splitting and Heun's method for the reaction term. In the one-dimensional model presented in section 4.2, the maximum difference (among all simulations considered) between the reactive tracer profiles from either method was found to be $O(10^{-7})$.

In the two-dimensional simulations presented in section 6.1.1, the order of magnitude of the maximum difference between the reactive tracer distributions depends on the Damköhler number. For $Da \sim O(0.1)$ and $Da \sim O(1)$ the maximum differences are $O(10^{-6})$ and $O(10^{-5})$ respectively. In these two cases, the differences reach a maximum

value early in the simulation and then continuously decrease. For $Da \sim O(10)$ the order of magnitude of the maximum difference jumps up to $O(10^{-3})$ and the error monotonically increases with time. Note that all these runs used $\Delta t = 5 \times 10^{-5}$ as the time step. Reducing Δt by an order of magnitude in the $Da \sim O(10)$ case reduced the maximum difference by an order of magnitude.

If we were solving a set of equations describing a particular physically meaningful system, these differences would be admittedly quite concerning. However, the two-dimensional toy data is only generated to create a dataset that can be used to illustrate the effect of spatial filtering. The results from the filtering process are unaffected by errors introduced by the numerical method. Rather, the resolution is the far more important factor to consider. Figures 3.1 and 3.2 quantify the differences. To the unknowing observer, the spatial distributions in columns one and two of Figure 3.1 look identical.

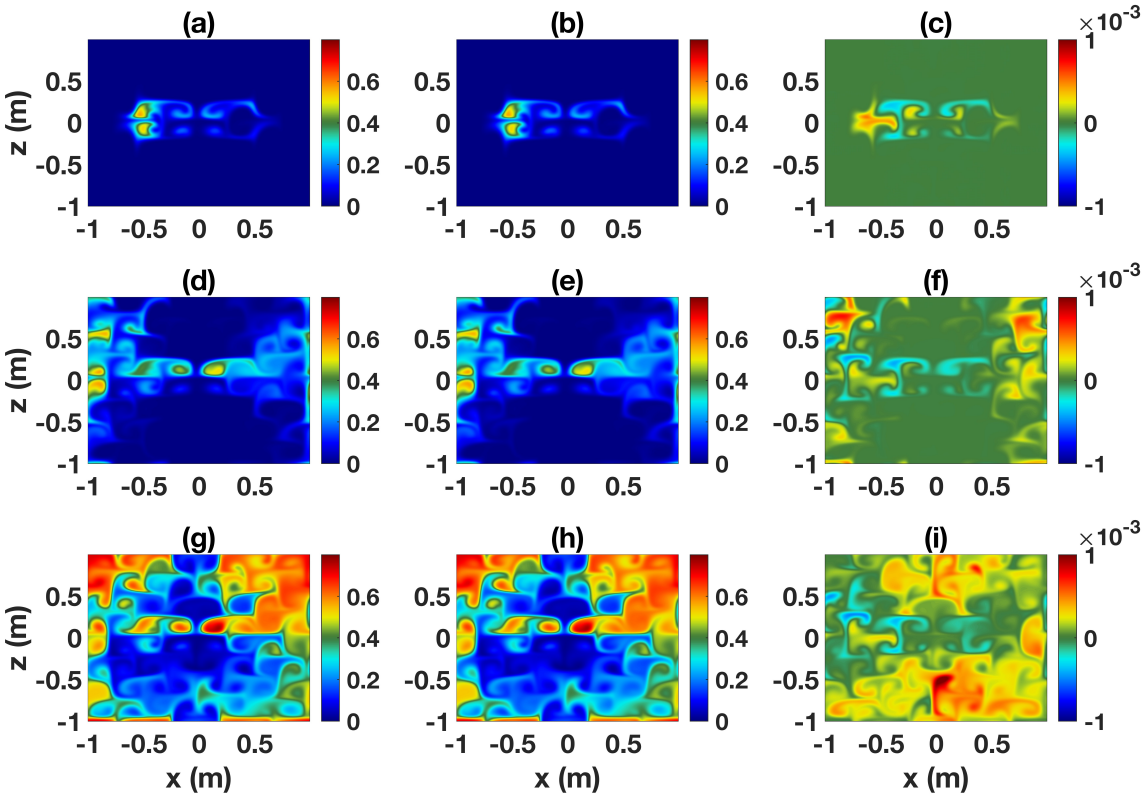


Figure 3.1: Solutions to the system with $Da \sim O(10)$ using Euler's method (first column), Heun's method with Strang splitting (second column), and the difference (third column). The difference is taken by subtracting the solution found with Euler's method from that found using Heun's method.

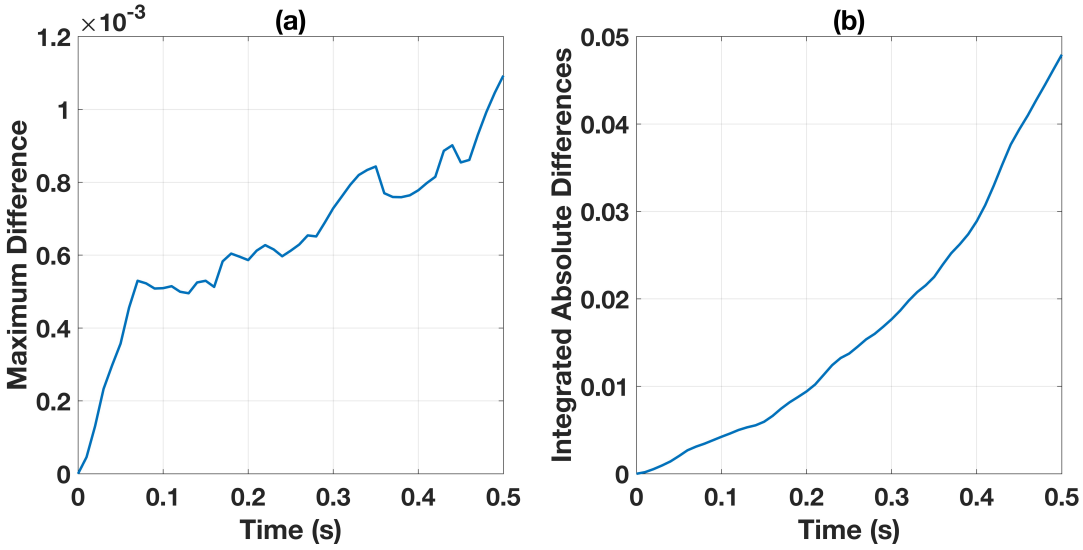


Figure 3.2: (a) Maximum difference between the Euler and Heun solutions when $Da \sim O(10)$, and (b) absolute differences integrated over the domain area.

Chapter 4

Analytical Treatment of the ADR Equation

In Chapter 2 we derived Reynolds averaged and filtered ADR equations. Both frameworks changed the form of the original ADR equation by introducing advection and reaction terms that would need to be parameterized in a RANS simulation or LES. In this chapter, we will explore these frameworks from a conceptual standpoint. We will also interpret the effects of the various terms in the equations through ODE analysis and in spectral space.

The intuition developed in Section 4.1 will be important for the interpretation of the Reynolds averaged ensemble in Chapter 5. In Section 4.2, the competing effects of advection, diffusion, and the reaction will be investigated using the reactive tracer distribution in spectral space. These results are relevant to those in Chapter 6. In Section 4.3, the Reynolds averaged reaction dynamics and spatially filtered reaction dynamics will be investigated. The single-spatial point ODE model is not directly helpful in our later analysis, but understanding how the reaction dynamics change under either framework is important.

4.1 Understanding RANS and LES with Toy Signals

Consider two signals $\delta_1 = \sin(x/2) + 0.1\sin(2x)$ and $\delta_2 = \sin(x/2 - \pi)$. The signals are plotted as ensemble members in the top left panel of Figure 4.1. If we consider the resulting signal under RANS, we get $(\delta_1 + \delta_2)/2 = 0.1\sin(2x)$ because the large components of the two signals are perfectly out of phase and cancel each other out. The mean captures what is essentially noise in one of the ensemble members. In this (albeit constructed) example,

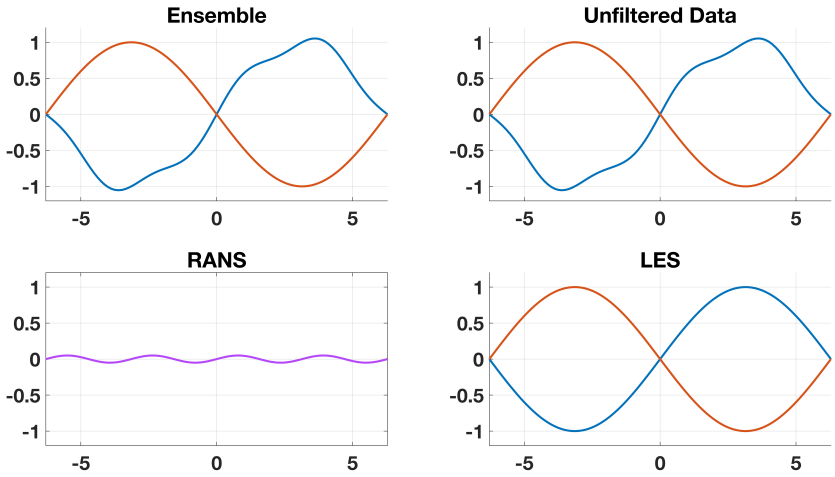


Figure 4.1: Result of Reynolds averaging when signals are interpreted as an ensemble versus the result of LES filtering the individual signals.

the fluctuations capture the lower frequency signal components. RANS is intended to represent the range of possible outcomes from a large ensemble so it is important to note that we should not expect good results from an ensemble with only two members.

Suppose we want to instead apply a filter to the two signals as if they were being processed via *a priori* LES. Let us choose a low-pass filter with a cutoff value that retains the low frequency components of the signals but removes the high frequency noise from δ_2. We are left with two signals that resemble the original signals fairly well. If we were to increase the cutoff wavenumber used by the filter, then it would also be possible to capture the high frequency component in the blue curve.

Under *a priori* LES, the resolved part of the signal converges to the actual signal as the cutoff wavenumber is increased past the largest active wavenumber in the signal. Under *a priori* RANS, increasing the size of the ensemble may increase the amount of information captured by the mean. However, cancellations between ensemble members dictate whether information ends up in the mean field or in the fluctuations. For highly variable systems such as turbulent flows, interference between the signals contained in the ensemble members is not something that can be predicted *a priori*. Therefore, it is possible that cancellations between ensemble members result in a large portion of the dynamics needing to be modelled.

4.2 Interpreting Dynamics in Spectral Space

LES filtering is often performed in spectral space because this allows high frequency signals to be isolated and removed. A tracer distribution can be interpreted in terms of signals of varying frequencies. As a reactive tracer is evolved through the ADR equation, so too are the frequencies that describe its distribution. In this section, we use toy models to examine how the frequencies evolve and how the terms that make up the ADR equation contribute to this evolution.

4.2.1 Non-Linear Reactions Activate Higher Wavenumbers

Consider Fisher's equation as an ODE with initial condition $\theta(t = 0, x) = \sin(kx)$ where k is a constant. Using Euler's method to discretize the ODE in time we have

$$\theta^{n+1} = \theta^n + dt\theta^n(1 - \theta^n). \tag{4.1}$$

So, after the first update θ becomes

$$\theta(t = dt, x) = \sin(kx) + dt(\sin(kx)(1 - \sin(kx)) \tag{4.2}$$

$$= (1 + dt)\sin(kx) - \frac{dt}{2}(1 - \cos(2kx)). \tag{4.3}$$

Squaring θ introduces the additional active wavenumbers $k = 0$ (due to the addition of a constant) and $2k$ (from the cosine). A wavenumber "cascade" thus occurs as the update is repeated. A similar effect can be found by plotting the spectral distribution of the analytical solution versus time.

Note that the term "cascade" is being used in this chapter to draw a parallel between the activation of higher wavenumbers due to the non-linear reaction and the spectral cascade induced by turbulence. The mechanisms behind the two processes are very different. In a turbulent cascade, kinetic energy is continuously being transferred from larger scales to smaller ones by inviscid processes. When the energy reaches small enough scales, it is dissipated by molecular viscosity. Turbulent cascades occur in physical space, but are generally interpreted in spectral space because the power spectral density of kinetic energy clearly indicates the active length scales. In physical space, the disorder associated with turbulence makes interpreting the cascade in detail quite difficult.

The cascade induced by the reaction does not depend on physics but rather on the non-linearity in the reaction term. Figure 4.2 compares the spectral cascades associated

with four common reaction terms. In the linear case there is simply no observable cascade, while in the three non-linear cases the cascade is very clear. It is important to note that the cascades in the non-linear cases require the initial tracer distribution to have a non-uniform initial spatial structure. The spectral power in each of the non-linear cases remains greatest for small wavenumbers. From our discretization of $\theta_t = \theta(1-\theta)$ we see that there is a consistent re-injection of spectral power at the initial wavenumber k and a small injection at wavenumbers 0 and $2k$. This is an important point that will be returned to in Chapter 6. Briefly, if low spatial frequencies dominate, then running simulations that cannot resolve the highest frequencies is less problematic.

The spectral cascade corresponds to the localized steepening of the tracer distribution in physical space resulting from the non-linearity of Fisher's equation. If the initial spatial distribution has a point, x_0, for which $\theta(x_0, t=0) = 0$ and $\theta(x_0 + \delta x, t=0) > 0$ then a particularly sharp front will form and be sustained until diffusion catches up with the reaction (assuming the reaction timescale is faster than that of diffusion). In the absence of diffusion, the reaction would cause the tracer distribution to develop a jump discontinuity at x_0. Panel (a) of Figure 4.3 shows how the solution of $\theta_t = \theta(1-\theta)$, $\theta(t=0) = \sin(2\pi x)$ develops steep valleys over time.

Fourier series converge exponentially fast for functions that are both analytic and periodic, but an n term Fourier series only converges at $O(n^{-1})$ for non-periodic functions[70]. As the distribution of the reactive tracer develops sharp transitions, convergence takes longer, until, in the limit of a jump discontinuity, the function is no longer smooth and the Gibbs phenomenon occurs. In panel (b) of Figure 4.3, the solution curves are filtered with a hard spectral filter with $k^{cut} = 50$. In the yellow curve, filtering has introduced oscillations because due to the longer Fourier series required to represent the steeper valleys.

In many numerical process studies, artificially large viscosity and diffusivity values are used to smooth the distributions of physical quantities, thereby reducing the number of terms required for convergence. This strategy also allows simulations to be run with a lower resolution. A coarse resolution may fail to capture sharp transitions in physical distributions, and thus such transitions would effectively become jump discontinuities. In practice, periodicity can be recovered by extending a dataset with a periodic extension so long as this does not make it unreasonably large and thus maintaining periodicity is generally of less concern than ensuring a distribution remains smooth.

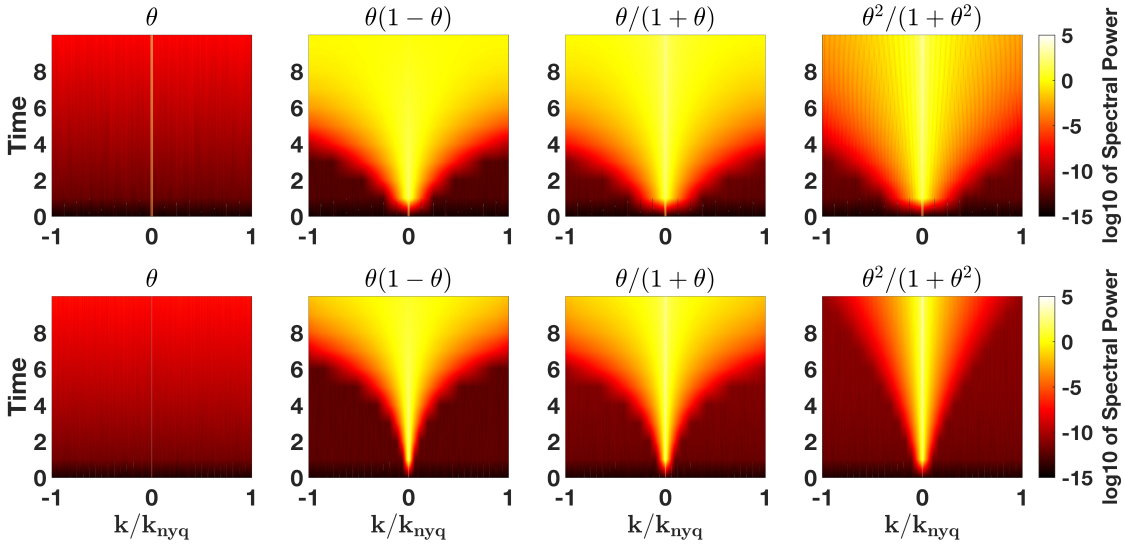


Figure 4.2: Cascades resulting from the evolution of different reaction terms in the absence of advection or diffusion. In the second row, the resolution is quadrupled. Note that the x-axis of each row is scaled by the Nyquist frequency corresponding to the resolution used. The initial condition is $\theta(0, x) = 0.5(\sin(4\pi x/L) + \sin(10\pi x/L))$.

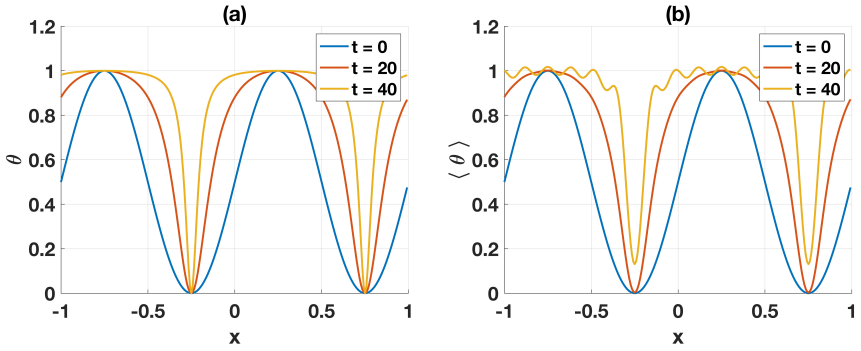


Figure 4.3: (a) Analytical solution to the ODE with Fisher's equation and (b) solution filtered with $k_{cut} = 50$.

4.2.2 Implications for Filtered Data

Consider two tracers $\theta = \exp(ik_1x) + \exp(ik_2x)$ and $\phi = \exp(im_1x) + \exp(im_2x)$ where $k_1, m_1 < k_{cut}$ and $k_2, m_2 \geq k_{cut}$. The operations of multiplication and spatial filtering do not commute, as shown in the following equations.

$$\langle\theta\phi\rangle = \begin{cases} \exp(i(k_1 + m_1)x), & \text{if } k_1 + m_1 < k_{cut} \\ 0, & \text{otherwise} \end{cases} \tag{4.4}$$

$$\langle\theta\rangle\langle\phi\rangle = \exp(i(k_1 + m_1)x) \tag{4.5}$$

When performing *a priori* LES, the differences will be apparent in any calculations performed on the simulation data.

Under true LES, filtered data is resolvable data, and so the conditions on equation 4.4 would also be applied to equation 4.5. For reactive tracers, the equations describing the reaction dynamics have the potential to evolve resolved features into unresolvable ones. The green area in Figure 4.4 indicates the area in $k - m$ space where $\exp(i(k_1 + m_1)x)$ can be resolved. The yellow areas indicate where cross-scale terms (due to the multiplication of resolved and **sfs** terms) can be resolved. The blue areas indicate that two out of phase **sfs** signals can cancel each other out and result in resolvable signals. In true LES, the **sfs** data is unknown and so the yellow and blue areas contain contributions to the tracer field that are, in theory, resolvable, but that can not be directly accounted for in practice. LES models account for the contributions of **sfs** terms through various parameterizations. This will be revisited in Section 7.2.

While we have only discussed results pertaining to the multiplication of two tracers, these concepts are also applicable when considering the advection term in the material derivative since it involves the multiplication of two physical quantities with various active spatial frequencies. Of course, if the velocity is constant, then it has no effect on the spectral distribution of the tracer.

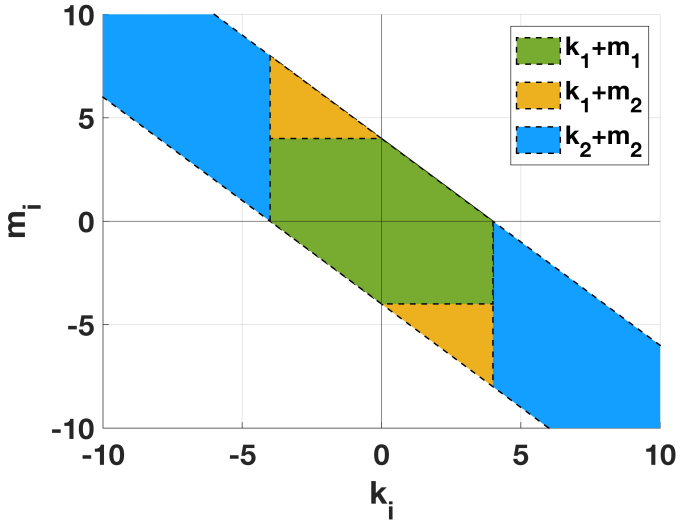


Figure 4.4: Areas in k_i–m_i space where $\exp(i(k_i + m_i)x)$ can be resolved assuming $k_{cut} = 4$.

4.2.3 Effects of Diffusion and Advection on Tracer Spectrum

Diffusion and viscosity act to smooth the spatial distributions of physical quantities. Their effect is to constrain the distribution of said quantities in spectral space. For velocity fields, increased viscosity values inhibit the formation of fine turbulent structures and thus restrict the spectral cascade that is attributed to turbulence. In the previous sections, we noted that non-linear reaction terms encourage higher frequency features in reactive tracer distributions. In this section, we consider the contributions of diffusion and advection.

Consider the one-dimensional diffusion equation in spectral space.

$$\theta_t = \kappa\theta_{xx} \tag{4.6}$$

$$\Rightarrow \tilde{\theta}_t = -\kappa k^2 \tilde{\theta} \tag{4.7}$$

$$\Rightarrow \tilde{\theta} = \tilde{\theta}(0)\exp(-\kappa k^2 t) \tag{4.8}$$

The solution with $\tilde{\theta}(t = 0) = 0.5$ is plotted in Figure 4.5 for (a) $\kappa = 1 \times 10^{-2}$ and (b) $\kappa = 1 \times 10^{-6}$. The smaller the diffusivity value, the longer it takes for the Gaussian to broaden. These Gaussian distributions indicate the envelope that restricts the spectral power at each wavenumber and can be interpreted as filters (since they affect higher wavenumbers more strongly). There exists a time at which the width of the Gaussian nears $2k_{cut}$ and the spectral power in the sub-filter-scale is suppressed. For a passive tracer, this time can

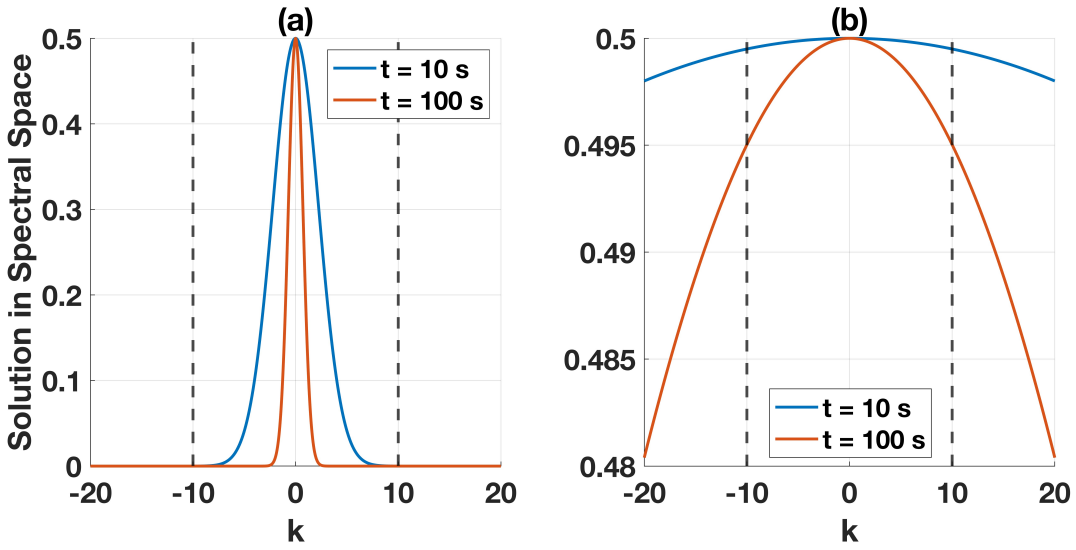


Figure 4.5: Solutions to the diffusion-reaction equation in Fourier space at $t = 10$s with (a) $\kappa = 1 \times 10^{-2}$ and (b) $\kappa = 1 \times 10^{-6}$. The vertical dashed lines indicate $k_{cut} = 20$ which was chosen as an arbitrary cutoff for the purposes of illustration.

be calculated via the relationship

$$t^* = \frac{-1}{\kappa k_{cut}^2} \ln\left(\frac{\varepsilon}{\tilde{\theta}(0)}\right) \tag{4.9}$$

where ε is some small threshold value. Unsurprisingly, the time is inversely proportional to the diffusivity, as observed in Figure 4.5. As $t \to \infty$, the passive tracer solution in Fourier space goes to $\tilde{\theta}(k) \to 0$ with the exception of $\tilde{\theta}(k = 0) = \tilde{\theta}(0)$. This says that the effect of diffusion is to create a uniform passive tracer distribution everywhere in the domain, which is precisely what we expect from our physical intuition.

To illustrate the effect of advection and diffusion on a reactive tracer, let's consider the one-dimensional ADR equation

$$\theta_t + u_x\theta + u\theta_x = \kappa\theta_{xx} + \theta(1 - \theta), \tag{4.10}$$

and prescribe a spatially-varying velocity field constructed with sinusoids of different fre-

Simulation Name	Diffusivity (m^2/s)	Prescribed velocity (m/s)	$Da = \alpha L/U$
LD	1×10^{-6}	0	n/a
HD	1×10^{-3}	0	n/a
HD-LA	1×10^{-3}	$\sin(4\pi x/L)$	1.41
HD-SA	1×10^{-3}	$\sin(10\pi x/L)$	1.41

Table 4.1: Simulations run with the one dimensional toy model. We use the root-mean-square of the prescribed velocity as the characteristic velocity scale and $L = 1$ (domain half width) as the characteristic length scale.

quencies

$$u = \sum_i \sin(k_i \pi x/L). \tag{4.11}$$

The simple one-dimensional model is solved with the explicit–implicit Euler's method solver as described in section 3.3. The four cases described in Table 4.1 were run. The initial condition for all simulations was taken to be $\theta(x, t = 0) = (\sin(4\pi x/L) + \sin(10\pi x/L) + 1)/3$ (shifted up by the minimum and normalized to that θ is in $[0, 1]$ everywhere). A supplementary case without diffusion or advection was compared with the analytical solution at all outputs and the maximum root–mean–square difference was found to be 0.0685. The difference was primarily due to sharp transitions in the tracer distribution between the equilibrium points $\theta = 0$ and $\theta = 1$. The effect of diffusion is to stabilize the model, therefore we expect our discretization, resolution, and timestep to suffice for the purposes of illustration.

In cases LD and HD, we purposefully do not introduce advection to demonstrate the competing effects of the reaction and diffusion on the spectral cascade. In Figure 4.6, the first and second columns correspond to simulations LD and HD, respectively. Increasing the diffusivity of the tracer leads to a more uniform tracer distribution in physical space. It also constrains the cascade of spectral power to higher wavenumbers as shown by comparing panels (e) and (f). The cascade coincides with the presence of sharp fronts in the physical distribution of the tracer as caused by the reaction.

When introducing advection into a system, an additional timescale and (potentially) many additional length scales are introduced. The introduction of large-scale advection

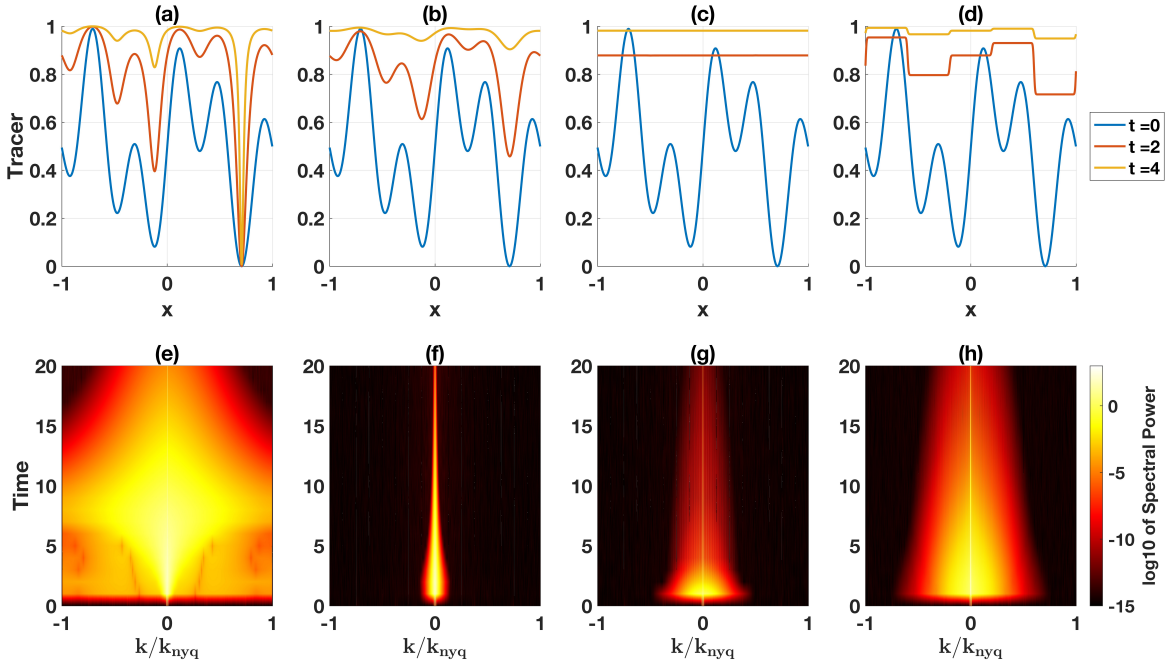


Figure 4.6: One dimensional tracer fields for (a) LD, (b) HD, (c) HD-LA, and (d) HD-SA. The second row shows the fields in spectral space as functions of wavenumbers and time.

given by

$$u = \sin(4\pi x/L) \tag{4.12}$$

causes the tracer distribution to reach uniformity in physical space more quickly, panel (c) of Figure 4.6. Note that the division between large and small scales is arbitrary. These terms are used to indicate the spatial frequencies of the velocities in HD-LA and HD-SA relative to one another.

While the introduction of the large-scale advection in HD-LA eliminates sharp fronts, it also allows for a larger cascade and a larger range of persistently active wavenumbers as compared to the advection-free case with the same diffusivity value, HD. In simulation HD-SA, the presence of small-scale advection causes local changes in the tracer distribution and thus sharpens the fronts. The sharpening of the fronts once again corresponds to an amplified cascade.

In turbulent systems, there is a large range of active advective length scales and so the

interplay between the effects of advection, diffusion, and the reaction are less clear-cut. We considered a case with multi-scale advection (not shown) taken as the average of the prescribed velocities in HD-LA and HD-SA. The resulting spectral cascade was found to lie between those of the HD-LA and HD-SA cases. Having limited resolution is concerning if you are considering a reactive tracer with a small diffusivity, and even more problematic if it is exposed to small–scale advection.

4.3 Fisher's Equation ODE Stability Dynamics

Modelling studies of biogeochemical systems often reduce complex processes to a set of ODEs thereby ignoring the effects of diffusion and transport[18, 28]. Taking this reductionist approach is computationally advantageous and allows model formulations to be analyzed using an arsenal of ODE analysis techniques. As we saw in Chapter 2, the form of the reaction term in the ADR equation is modified under Reynolds averaging and spatial filtering. Inevitably, this changes the reaction dynamics that lead to the growth of the Reynolds averaged reactive tracer and the filtered reactive tracer. To study how the dynamics change, we reduce the ADR system to an ODE. The solution to $\theta_t = \theta(1-\theta)$ with initial condition $\theta(0) = \theta_0$ is

$$\theta(t) = \frac{\theta_0}{\theta_0 + (1-\theta_0)\exp(-t)}. \tag{4.13}$$

The ODE has an unstable equilibrium point at $\theta = 0$ and a stable equilibrium at $\theta = 1$, Figure 4.7. Since we are interested in non-negative tracer values, we can safely assume that $\theta_0 \geq 0$ and so $\theta \to 1$ as $t \to \infty$. Note that in Chapter 3, Fisher's equation was modified by a hyperbolic tangent to ensure that any oscillations in the numerical solution causing θ to become negative would not grow towards $-\infty$.

4.3.1 Reynolds Averaging

When the Reynolds averaging procedure (substituting a decomposition of the form $\theta = \Theta + \theta'$ and then averaging) is applied to Fisher's equation, a sink appears in the resulting reaction term.

$$\overline{F(\theta)} = \Theta(1-\Theta) - \overline{(\theta')^2} \tag{4.14}$$

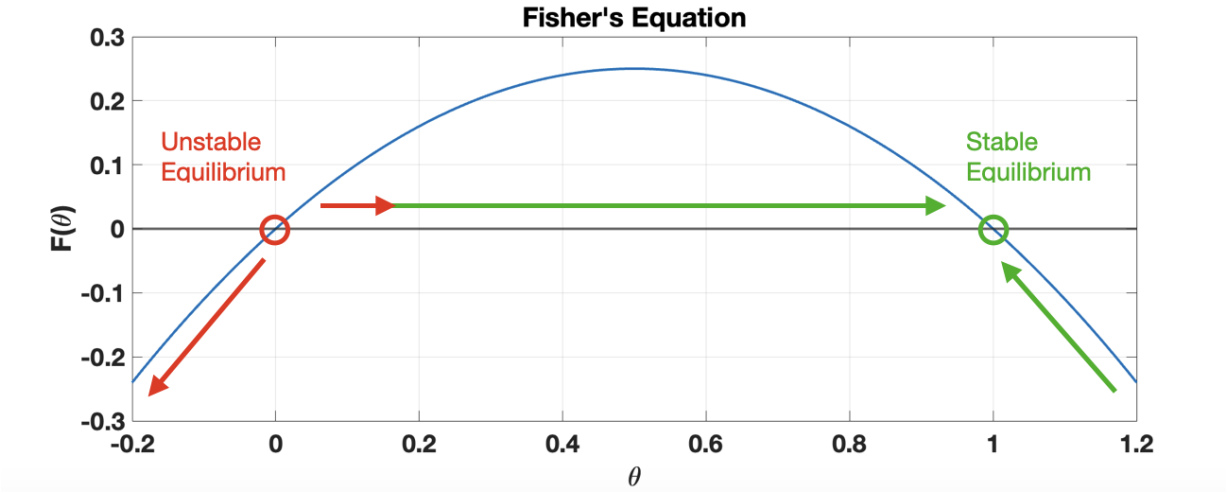


Figure 4.7: $F(\theta) = \theta(1-\theta)$ as a function of θ.

The effect of the sink is to shift the parabolic function describing the growth rate of θ downwards. In panel (a) of Figure 4.8, this is shown for several constant sink values. In a turbulent system, the sink will not be constant. Note that as the parabola shifts downwards, the equilibrium points of the system become

$$\theta = \frac{1}{2} \pm \frac{1}{2}\sqrt{1 - 4\overline{(\theta')^2}}. \tag{4.15}$$

So long as $\frac{1}{2}\sqrt{1 - 4\overline{(\theta')^2}} \neq 0$ the stability of the equilibrium points does not change. The point with the smaller value of θ remains unstable and the other point remains stable.

If we consider $\overline{(\theta')^2}$ to be a system parameter, then we can conclude that the system has a bifurcation point at $\overline{(\theta')^2} = 1/4$. At this point, a saddle-node bifurcation occurs. As a result, the system behavior changes. For $\theta_0 \geq 0.5$, $\theta \to 0.5$ (the equilibrium value) but for $\theta_0 < 0.5$, $\theta \to -\infty$. For $\overline{(\theta')^2} > 1/4$, the equilibrium points become imaginary and $\theta \to -\infty$ for any θ_0.

For convenience, assume $\overline{(\theta')^2}$ is constant in time. Solving $\Theta_t = \overline{F(\theta)}$ with $\Theta(0) = \theta_0$ yields the following

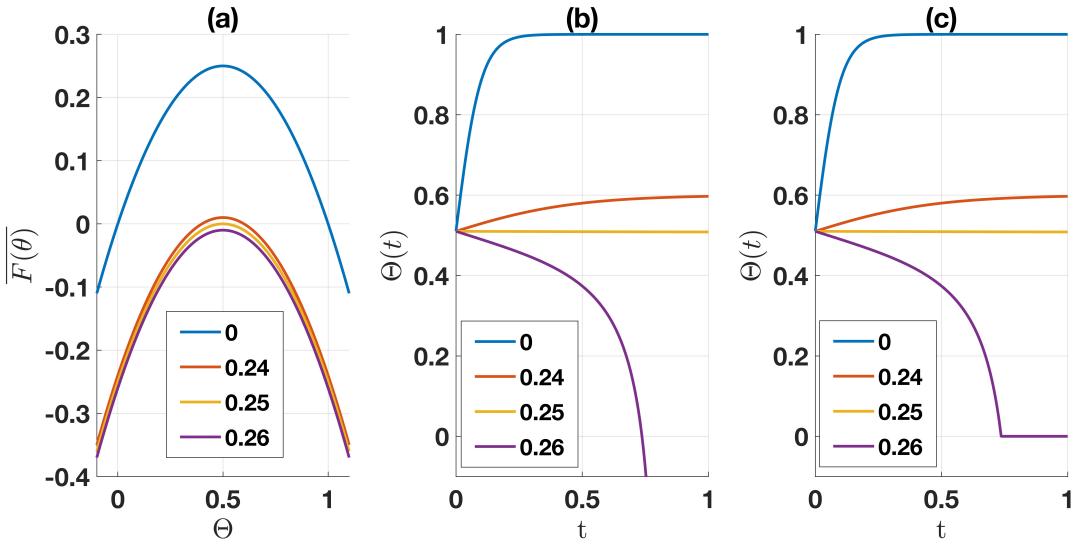


Figure 4.8: (a) $\Theta(1-\Theta) - \overline{(\theta')^2}$ with a constant value of $\overline{(\theta')^2}$ given in the legend. Solutions to (b) $\Theta_t = \Theta(1-\Theta) - \overline{(\theta')^2}$ and (c) $\Theta_t = \left(\Theta(1-\Theta) - \overline{(\theta')^2}\right)\tanh(\Theta/0.001)$ with $\Theta(0) = 0.51$.

$$\Theta = \begin{cases} \dfrac{1}{2} + \dfrac{\sqrt{1-4\overline{(\theta')^2}}}{2}\tanh\left(\dfrac{\sqrt{1-4\overline{(\theta')^2}}}{2}t - \operatorname{arctanh}\left(\dfrac{1-2\theta_0}{\sqrt{1-4\overline{(\theta')^2}}}\right)\right), & \text{if } a < 1/4 \\ \dfrac{(2\theta_0-1)t+4\theta_0}{2(2\theta_0-1)t+4}, & \text{if } a = 1/4 \\ \dfrac{1}{2} - \dfrac{\sqrt{4\overline{(\theta')^2}-1}}{2}\tan\left(\dfrac{\sqrt{4\overline{(\theta')^2}-1}}{2}t - \arctan\left(\dfrac{2\theta_0-1}{\sqrt{4\overline{(\theta')^2}-1}}\right)\right), & \text{if } a > 1/4 \end{cases} \tag{4.16}$$

As compared to equation 4.13, the solution form has changed drastically due to the addition of the sink. The first and third expressions come from using the identities $\tanh(x) = -i\tanh(ix)$ and $i\operatorname{arctanh}(x) = \arctan(ix)$. Solutions for varying values of $\overline{(\theta')^2}$ are shown in panels (b) and (c) of Figure 4.8.

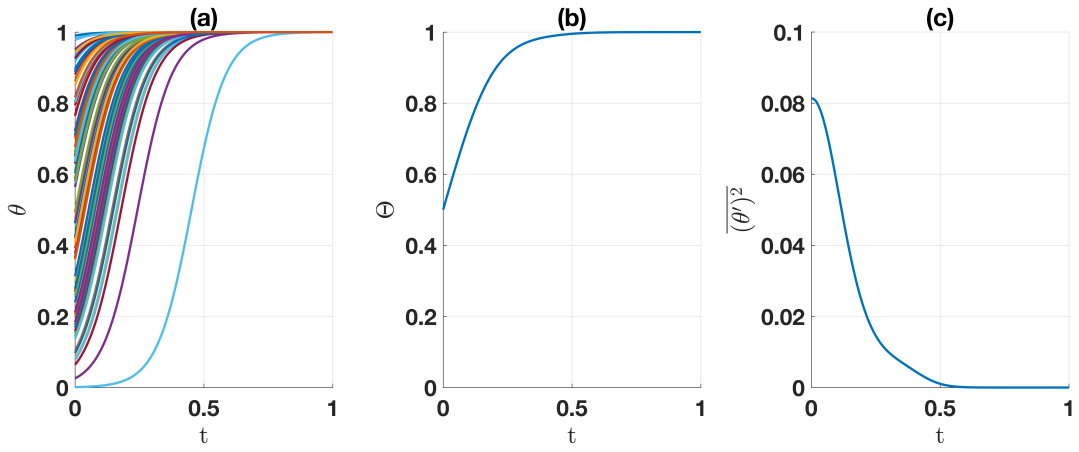


Figure 4.9: (a) Solutions to $\theta_t = \theta(1-\theta)$ with initial conditions randomly generated from a uniform distribution. (b) Mean and (c) scalar variance of the ensemble.

When initializing an ensemble of reactive tracer values for a system with a single reactive tracer, you would need it to be perfectly uniform such that to have $\overline{(\theta')^2} = 0$. In a multi-component system with two or more reactive tracers that interact, it is possible for the covariances to cancel in such a way that $\overline{(\theta'\phi')} = 0$ without the ensemble being perfectly uniform. If the initial scalar variance is non-zero, then in the absence of any perturbations to the ensemble members, the scalar variance will tend towards zero at the same rate that the ensemble members tend to the equilibrium value of $\theta = 1$. In Figure 4.9, we create an ensemble with initial conditions randomly chosen from $U(0,1)$. The initial value of the scalar variance is very close to the variance of the $U(0,1)$ distribution, as expected. This may seem reassuring given our previous discussion of how the sink term may alter the stability of the Reynolds averaged system. The scalar variance monotonically decreases for all time and is never greater than or equal to the bifurcation value.

However, this narrative is a cautionary tale that illustrates the danger of basing one's intuition on overly simplified ODE models. In the oceans, there are numerous factors that may effectively perturb the growth trajectories of the ensemble members. Turbulent mixing modifies the spatial distribution of a tracer, thereby creating fluctuations and driving tracer gradients. This will be revisited in Chapters 5 and 6. Other perturbations can come from the modification of growth rates and carrying capacities by environmental conditions (e.g. cloudiness[12]) . Therefore, in more realistic systems, it is likely that the scalar variance is quite large and is sustained by environmental factors.

4.3.2 LES Filtering

Recall the modified reaction function for Fisher's equation under LES:

$$\langle F(\theta)\rangle = \langle\theta\rangle(1-\langle\theta\rangle) - \langle\langle\theta\rangle^2\rangle + \langle\theta\rangle^2 - 2\langle\langle\theta\rangle\theta'\rangle - \langle(\theta')^2\rangle \tag{4.17}$$

We want to investigate how the behavior of the filtered ODE changes based on the form of the correction term. Let $\theta = \exp(ik_1x) + \exp(ik_2x)$ where $k_1 < k_{cut}$ and $k_2 > k_{cut}$. Suppose k_1 and k_2 are both non-negative. Then the terms in the correction to the LES filtered equation become:

$$\langle\langle\theta\rangle^2\rangle - \langle\theta\rangle^2 = \begin{cases} 0, & \text{if } k_{cut}/2 > k_1 \\ -\exp(i2k_1x), & \text{if } k_{cut} > k_1 \geq k_{cut}/2 \end{cases} \tag{4.18}$$

$$\langle\langle\theta\rangle\theta'\rangle = 0 \tag{4.19}$$

$$\langle(\theta')^2\rangle = 0 \tag{4.20}$$

If k_1 and k_2 have the same sign, then the filtered reaction falls under one of two cases:

$$\langle F(\theta)\rangle = \begin{cases} \langle\theta\rangle(1-\langle\theta\rangle), & \text{if } |k_1| < k_{cut}/2 \\ \langle\theta\rangle, & \text{if } k_{cut}/2 \leq |k_1| < k_{cut} \end{cases} \tag{4.21}$$

Suppose now that k_1 is non-negative but $k_2 < -k_{cut}$. In this case, the terms in the LES correction become:

$$\langle\langle\theta\rangle^2\rangle - \langle\theta\rangle^2 = \begin{cases} 0, & \text{if } k_{cut}/2 > k_1 \\ -\exp(i2k_1x), & \text{if } k_{cut} > k_1 \geq k_{cut}/2 \end{cases} \tag{4.22}$$

$$\langle\langle\theta\rangle\theta'\rangle = \begin{cases} \exp(i(k_1+k_2)x), & \text{if } -k_{cut} > k_2 \geq -k_{cut} - k_1 \\ 0, & \text{if } k_2 \leq -k_{cut} - k_1 \end{cases} \tag{4.23}$$

$$\langle(\theta')^2\rangle = 0 \tag{4.24}$$

So we have four cases for the correction and thus four possible filtered reactions when k_1 and k_2 have opposite signs:

$$\langle F(\theta)\rangle = \begin{cases} \langle\theta\rangle(1-\langle\theta\rangle), & \text{if } |k_1| < k_{cut}/2 \text{ and } |k_2| < k_{cut} + k_1 \\ \langle\theta\rangle, & \text{if } k_{cut}/2 \leq |k_1| < k_{cut} \text{ and } |k_2| < k_{cut} + k_1 \\ \langle\theta\rangle(1-\langle\theta\rangle-\theta'), & \text{if } |k_1| < k_{cut}/2 \text{ and } k_{cut} + k_1 \leq |k_2| \\ \langle\theta\rangle(1-\theta'), & \text{if } k_{cut}/2 \leq |k_1| < k_{cut} \text{ and } k_{cut} + k_1 \leq |k_2| \end{cases} \tag{4.25}$$

In the first case, the form of the ODE is unchanged. The second and fourth cases now only have an unstable equilibrium at 0. In the third case, the stable equilibrium is shifted down to $1-\theta'$. The four possible solutions are

$$\text{LES1: } \langle\theta\rangle(t) = \frac{\theta_0}{\theta_0 + (1-\theta_0)\exp(-t)} \tag{4.26}$$

$$\text{LES2: } \langle\theta\rangle(t) = \theta_0 \exp(t) \tag{4.27}$$

$$\text{LES3: } \langle\theta\rangle(t) = \frac{(1-\theta')\theta_0 \exp((1-\theta')t)}{1-\theta'-\theta_0+\theta_0\exp((1-\theta')t)} \tag{4.28}$$

$$\text{LES4: } \langle\theta\rangle(t) = \theta_0 \exp((1-\theta')t) \tag{4.29}$$

The labels are provided for interpreting Figure 4.10 which shows sample solution curves as a function of time with $\theta' = 0.1$ taken to be constant. Note that the LES1 solution and the true solution are the same for a single-spatial point model since spatial filtering does not have any significance without a spatial distribution.

4.4 Travelling Wave Solutions

This section is presented for completeness given the substantial amount of literature that investigates travelling wave solutions to Fisher's equation.

Consider the scalar transport equation reduced to one spatial dimension with $u = 0$

$$\theta_t = \kappa\theta_{xx} + F(\theta). \tag{4.30}$$

For simplicity, we present the equation without an advection term, though it is common practice to group the reaction and advection terms into a function of the form $G(\theta, \theta_x)$ which would take the place of $F(\theta)$ in the equation above. To find travelling wave solutions, we move into a reference frame moving with constant speed c, $z = x - ct$, and look for

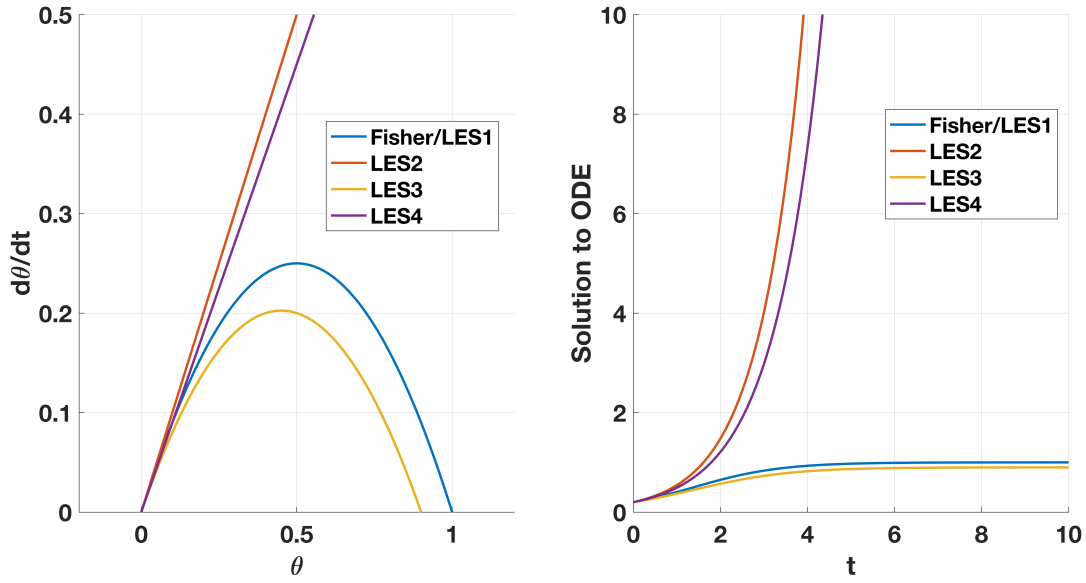


Figure 4.10: (a) $\langle F(\theta) \rangle$ for the various ODEs. (b) Solutions with initial condition $\theta_0 = 0.2$ and $\theta' = 0.1$.

solutions of the form $\theta(x,t) = \tilde{\theta}(z)$. Switching into the moving reference frame allows for the PDE to be rewritten as an ODE

$$-c\tilde{\theta}' = \kappa\tilde{\theta}'' + F(\tilde{\theta}) \tag{4.31}$$

$$\kappa\tilde{\theta}'' + c\tilde{\theta}' = -F(\tilde{\theta}) \tag{4.32}$$

To require that the solution be bounded and approach equilibrium states as $z \to \pm\infty$, we impose the following conditions

$$\tilde{\theta}(-\infty) = \tilde{\theta}_L, \qquad \text{and} \qquad \tilde{\theta}(\infty) = \tilde{\theta}_R, \qquad \text{where} \qquad F(\tilde{\theta}_L) = F(\tilde{\theta}_R) = 0. \tag{4.33}$$

If we let $\psi = \tilde{\theta}'$, then the second order ODE can be re-written as a system of first order ODEs

$$\kappa\psi' + c\psi = -F(\tilde{\theta}), \tag{4.34}$$

$$\tilde{\theta}' = \psi. \tag{4.35}$$

Expressing the system in this way allows us to apply dynamical systems techniques, such as

performing stability analyses. A travelling wave solution exists if a trajectory from $(\tilde{\theta}_L, 0)$ to $(\tilde{\theta}_R, 0)$ can be identified in phase space[62]. There is a large body of literature surrounding this problem for various forms of $F(\theta)$ and the more general case $G(\theta, \theta_x)$[104]. Exact solutions tend to be highly specialized, and traveling wave solutions are more generally shown with non-constructive proofs. For Fisher's equation, $F(\theta) = \alpha\theta(1-\theta)$, there are traveling wave solutions if $c \geq 2\sqrt{\alpha\kappa}$[30]. Investigating travelling wave solutions to Fisher's equation within LES is a potential avenue for future work.

Chapter 5

Reynolds Averaging Analysis

Note that the material in Sections 5.1 and 5.2 was published in[55].

In sections 2.4 and 2.4.2, we presented the Reynolds averaged equations and a method for treating ADR equations. In this chapter, we begin by presenting the results from an ensemble of simulations governed by equations 2.9 and 2.11. The ensemble provides data that can be used to diagnose the ability of Reynolds averaged quantities to capture the dynamics of a reactive tracer. The mean quantities described in section 2.4 are calculated by averaging over the ensemble members. The fluctuations are the differences between each ensemble member and the ensemble mean. The analysis of the ensemble is what we term *a priori* RANS. Note that we use the term "RANS" in the sense of the simulation method and not as an acronym.

Following the *a priori* RANS analysis, we will consider the results of pseudo-RANS simulations. These simulations are described in section 5.3. We term them "pseudo-RANS" because we are solving the Reynolds averaged ADR equations, but not the Reynolds averaged Navier-Stokes equations. Rather, we use the ensemble data to determine the mean velocity field. The theory behind Reynolds averaging suggests that solving the Reynolds averaged ADR equation (eq. 2.32) should yield a result that resembles the ensemble mean. In section 5.3.1 we will determine whether this holds true. Further, by isolating the eddy flux and eddy reaction terms in the various simulations, we can determine their effects on the mean. Since the passive tracer is not affected by eddy reactions, we need only consider the effects of eddy fluxes.

5.1 Setup for Ensemble of 50 Two-Dimensional Rayleigh-Taylor DNS using SPINS

Simulation parameters and dimensionless numbers are given in Table 5.1. All simulations were run in two dimensions with a 2.048m wide and 0.512m tall domain. We used 4096 grid points in the horizontal and 1024 in the vertical to have 0.5mm resolution in both directions. Periodic boundary conditions were implemented in x and free slip boundary conditions were implemented in z.

Table 5.1: Simulation parameters and dimensionless numbers for Rayleigh-Taylor Ensemble.

Simulation Parameter	**Value**	**Dimensionless Number**	**Value**
L_x	2.048 m	Re	1.1264×10^4
L_z	0.512 m	Sc	7.1429
N_x	4096	Pe	8.0457×10^4
N_z	1024	Da	2.3273
g	9.81 m/s^2		
ρ_0	1000 kg/m^3		
ν	1×10^{-6} m^2/s		
κ	1.4×10^{-7} m^2/s		
α	0.1		

All simulations begin from a state with $\vec{u} = 0$. To induce the formation of Rayleigh-Taylor (RT) instabilities, each ensemble member is initialized with an unstable density stratification that is perturbed in the horizontal. The density and velocity fields thus take the form

$$\rho_E(\vec{x}, t = 0) = -5 \times 10^{-4} \left(1 - \tanh\left(\frac{z - 0.256 - \varepsilon(x)}{0.02}\right)\right), \tag{5.1}$$

$$\varepsilon(x) = 2.5 \times 10^{-3} \sum_{i=1}^{3} Y_{1i} \sin\left(\frac{16\pi(Y_{2i} + 1)}{2.048} x + 2\pi Y_{3i}\right), \tag{5.2}$$

$$\vec{u}(\vec{x}, t = 0) = 0, \tag{5.3}$$

where $Y_{ji} \sim U(0, 1)$ is a random variable chosen from a uniform distribution between 0 and 1. Following standard practice, the random number generator for the distribution is

seeded by the fastest changing portion of the clock-time at the start of each simulation. The only difference between ensemble members is the perturbation, ε, applied to the initial density stratification. The initially unstable density stratification leads to the formation of RT instabilities. By perturbing the density interface in each simulation, we create lateral variability between ensemble members as the large-scale dynamics of RT instabilities maintain some memory of the initial conditions of the system[21].

The instability growth is exponential in time and a quasi-turbulent state is reached by $t = 26$ seconds. We generate an ensemble of 50 simulations (i.e. 50 realizations of the quasi-turbulent state), storing the initial condition of each and then storing data every two seconds from $t = 14$s to $t = 40$s. This yields 2.5G of data per ensemble member and a total of 125G of data for subsequent analysis of the ensemble. Each of these relatively small simulations took roughly 4 hours to run with 16 cores giving a total of 200 hours of computing time.

Panel (a) of Figure 5.1 shows an example stratification from a subdomain of one of the simulations. In panels (c) through (e), the initial stratification in three other ensemble members are shown. The distinction between ensemble members comes from the perturbations, ε, to the density stratification, which are observable by comparing the panels.

Estimates of the dimensionless numbers were calculated using the domain height as the characteristic length scale and the maximum root-mean-square vertical velocity of a sample ensemble member as the velocity scale. Values are given in table 5.1. The Reynolds number, $Re = UL/\nu$, represents the ratio of the inertial to viscous forces. Our simulations have $Re \approx 1.1264 \times 10^4$ indicating the flow becomes turbulent. The Schmidt number, $Sc = \nu/\kappa = 7.1429$, tells us the momentum diffusivity is greater than that of the tracers. The Péclet number describes the ratio of advective to diffusive transport and is given by $Pe = Sc \cdot Re \approx 8.0457 \times 10^4$.

In each of the simulations, the reaction term is

$$F(\theta) = 0.1 \cdot \theta(1 - \theta) \cdot \tanh(\theta/0.001), \tag{5.4}$$

where the multiplication by the hyperbolic tangent ensures that any oscillations around the unstable equilibrium $\theta = 0$ are suppressed. The reaction timescale parameter $\alpha = 0.1$ was chosen so that the Damköhler number, which we define as $Da = \frac{\alpha L}{U} \approx 2.3273$, is $O(1)$. The order of Da was chosen to balance the reaction and advective timescales for the purposes of illustration. A fast reaction (e.g. $\alpha = 1$) has $\theta \to 1$ too quickly for structures created from turbulent mixing to be observed. Slow reactions (e.g. $\alpha = 0.01$) allow for the creation of sharp fronts which can be difficult to resolve.

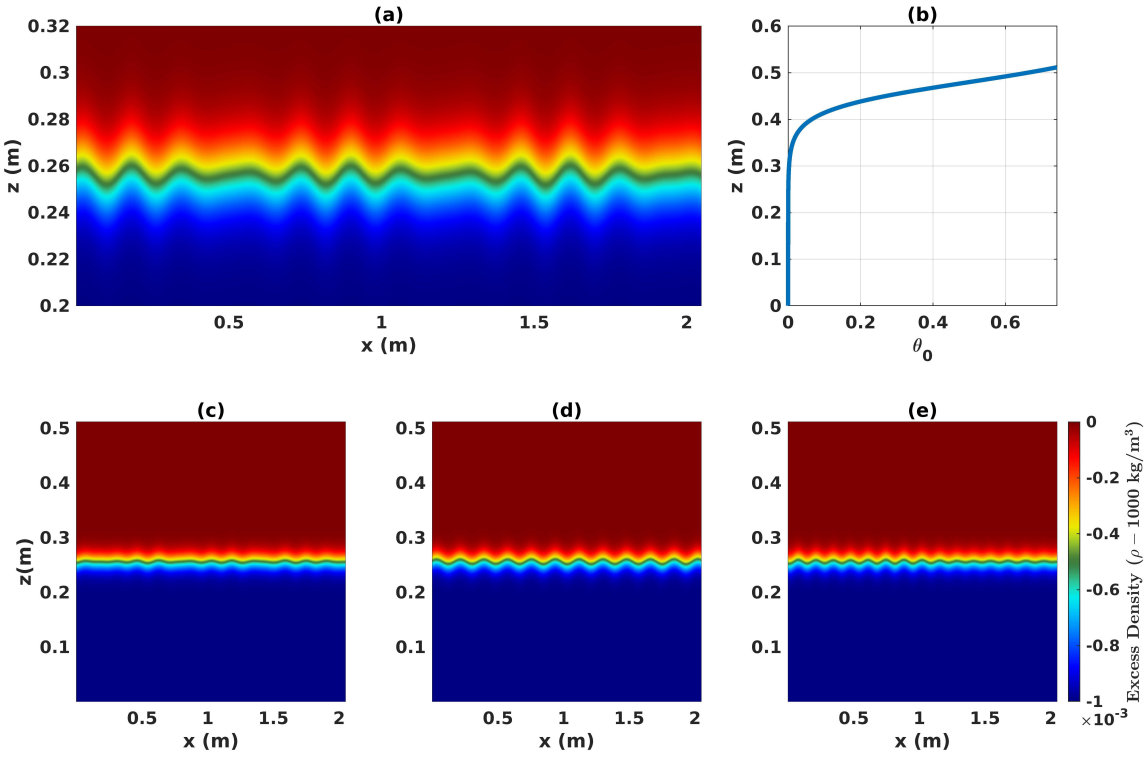


Figure 5.1: (a), (c)-(e) Sample initial density stratifications perturbed by $\varepsilon(x)$ (eq 6.7). (b) Initial tracer concentration profile.

The initial distributions of both the reactive and passive tracers are given by

$$\theta(\vec{x}, t = 0) = 0.5 \left(1 + \tanh\left(\frac{z - 0.48}{0.06}\right)\right), \tag{5.5}$$

so that the tracers lie in a band along the top of the domain as shown in panel (b) of Figure 5.1. Each simulation evolves both tracers with the same velocity fields and the tracers do not interact. The simulations are stopped after 40s when the system has reached a well-mixed state.

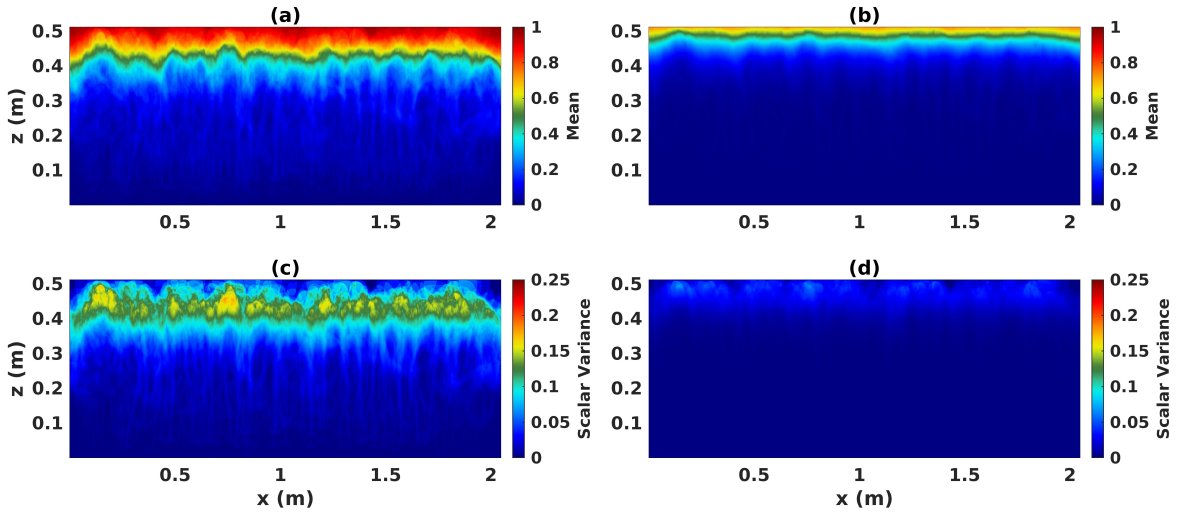


Figure 5.2: Mean and scalar variance of the reactive, (a) and (c), and passive, (b) and (d), tracers at $t = 26$s.

5.2 *A Posteriori RANS* Results

5.2.1 Tracer Mean and Scalar Variance

The reactive and passive tracers are initially distributed according to a hyperbolic tangent function varying with z so that there is a tracer band lying along the top of the domain. The system starts at rest to mimic the accumulation of a tracer in calm waters, and because this state provides a clear basis of comparison for analyzing differences in the spatial distributions of the reactive versus passive tracers. The initial density stratification is centered at $z = 0.256$m, about 0.16m below the bottom of the tracer band. There is thus a delay between the start of the simulation and the time at which the RT instabilities start advecting the tracers. During this time, the tracers begin diffusing downwards and the reactive tracer grows according to the function in equation 5.4. The reaction both increases the concentration of the tracer and accelerates its downwards spread by enhancing Fickian diffusion. Therefore, the reactive tracer front extends lower into the domain, allowing the RT plumes to reach it sooner than the passive tracer front.

Figure 5.2 shows the (a) mean and (b) scalar variance of the reactive tracer at $t = 26$s. When comparing these quantities with those of the passive tracer, panels (b) and (d), it is clear that the magnitude of the reactive tracer ensemble mean is nearly twice that of the passive tracer and that it extends further downwards. In panels (a) and (b) of Fig-

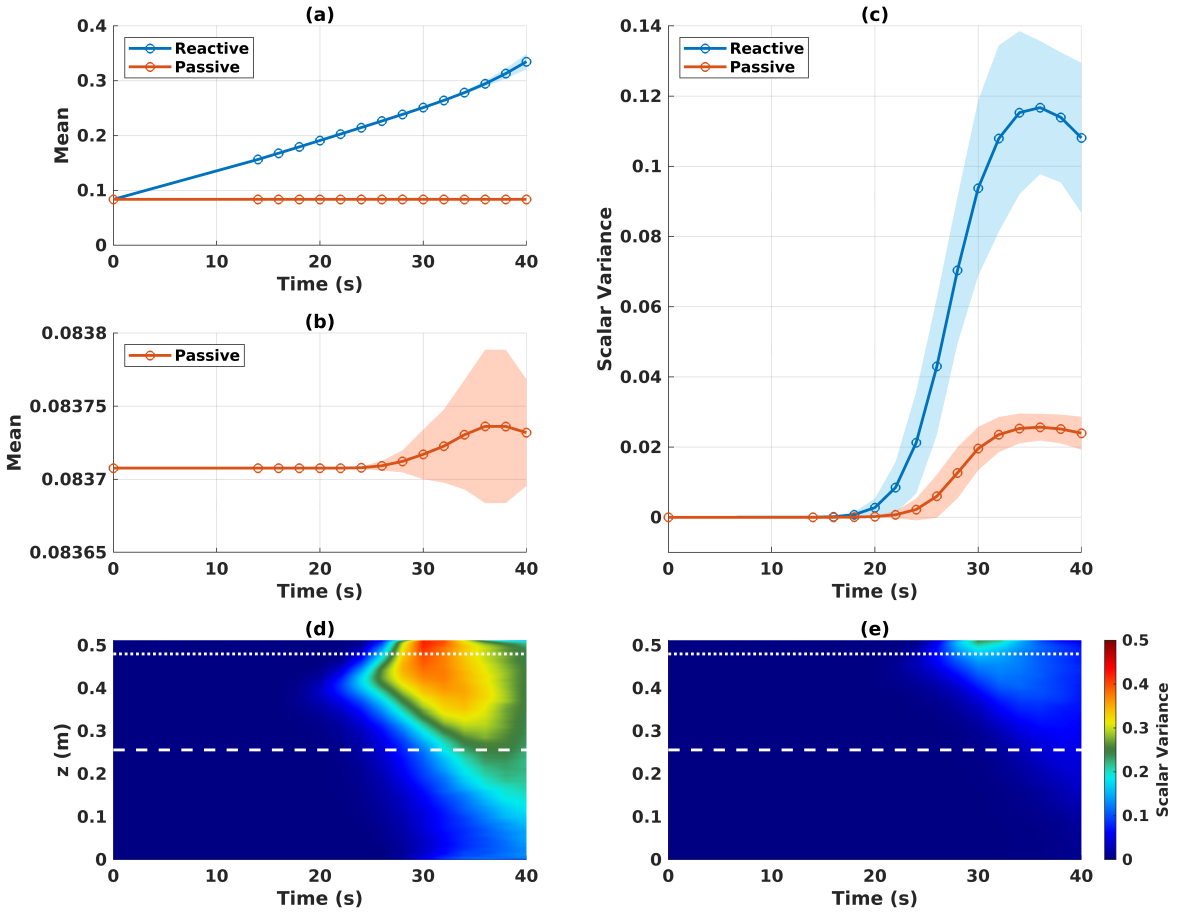


Figure 5.3: (a)-(b) Bulk mean tracer concentrations and (c) bulk scalar variances for the reactive (blue) and passive (orange) tracers. Shaded areas extend two standard deviations away from the mean. (d)-(e) Scalar variance integrated with respect to x for the reactive and passive tracers, respectively.

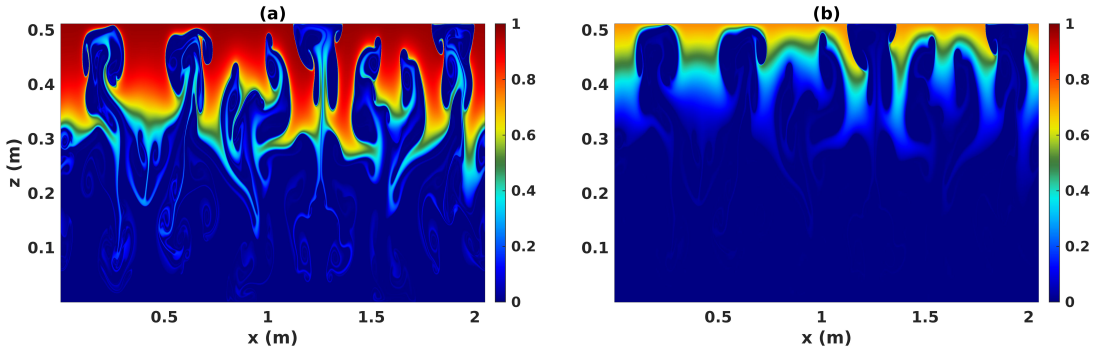


Figure 5.4: (a) Reactive and (b) passive tracer distributions in a sample ensemble member at $t = 26$ s.

ure 5.3 the values of the means of the reactive (blue) and passive (orange) tracers are integrated over the domain and plotted as functions of time. The mean reactive tracer concentration increases by nearly 400% while changes in the mean passive tracer concentration are $O(10^{-5})$ and likely due to the filter used in the numerical method. Note that in all Figures presented herein, shaded areas extend two standard deviations away from the corresponding ensemble means.

The ensemble is designed so that the RT plumes in each simulation have different spatial distributions. In each simulation, the RT bubbles (plumes of light fluid rising into heavy fluid with mushroom-shaped heads) push up against the tracer front and the tracer concentration is displaced upwards and outwards around the bubble, Figure 5.4. Meanwhile, spikes entrain the tracers downwards, causing the streaks observed in Figure 5.2. Shear causes vorticial structures to form on the undersides of the mushroom-shaped plume heads. These vortices are the first manifestation of turbulence in the flow and begin mixing the tracer that is displaced around the RT bubbles. While the coherent structures that characterize turbulent mixing are obvious in the ensemble members, Figure 5.4, they are not captured by the ensemble mean because they are essentially averaged out. Instead, turbulent structures are captured by the fluctuations, defined as differences between the individual simulations and the ensemble mean. The tracer fields in each of the simulations begin to differ from the mean as soon as the RT plumes start affecting their spatial distribution. Panel (c) of Figure 5.3 indicates a sharp increase in the scalar variance of the reactive tracer (blue) at $t = 18$s as the RT bubbles reach the tracer front. It takes longer for the plumes to reach the passive tracer front.

The turbulence in each of the simulations deforms and contorts material volumes of the

conserved scalar, in this case our passive tracer, and increases the magnitude of local scalar gradients. This in turn enhances molecular diffusion[109]. When this same process acts on the reactive tracer, the reaction occurring within the material volume complicates things further. For growth governed by Fisher's equation, the concentration in each material volume increases towards the stable equilibrium value $\theta = 1$ thereby increasing the rate of molecular diffusion. This doubly enhanced diffusion allows the reactive tracer to spread to areas that a passive tracer may take much longer to reach, or potentially never reach should it have a sufficiently small diffusivity and exist in a sufficiently large domain. As the process of deformation by the flow is repeated, diffusion is further enhanced.

The scalar variance of the reactive tracer acts as a sink in the mean ADR equation (equation 2.32) and as a source in the fluctuation equation (equation 2.33). The fluctuations are effectively taking concentration from the mean field while also growing according to Fisher's equation. In panels (a) and (c) of Figure 5.2 the spatial distribution of the scalar variance looks like it fits under that of the mean as if the two distributions were puzzle pieces. As the tracers are entrained deeper into the domain, concentration is inevitably transferred from the mean to the scalar variance, which evolves into a band spanning the horizontal extent of the domain. Eventually, the system becomes so well-mixed that the differences between ensemble members become less noticeable and thus the scalar variance decreases, Figure 5.3 panel (c).

In panels (d) and (e) of Figure 5.3, the reactive and passive scalar variances are integrated with respect to x and plotted as a function of depth and time. The dotted white lines indicate the inflection point of the hyperbolic tangent function describing the initial tracer distribution and the dashed lines indicate the height of the mean initial density stratification. The scalar variances begin to significantly increase once the RT plumes reach the tracer interfaces. This occurs at a greater depth and earlier for the reactive tracer due to the growth from the reaction. The scalar variance of the passive tracer reaches a maximum at the top of the domain as the RT plumes reach the upper boundary and then degrade, resulting in increased turbulence. As turbulent structures entrain the passive tracer deeper into the domain, its scalar variance propagates downwards. The scalar variance corresponding to the reactive tracer behaves similarly. However, we note that it propagates in both vertical directions and has a much larger magnitude. The upwards propagation corresponds to the transfer of concentration from the mean to the fluctuations, while the downwards propagation is uniquely due to RT induced turbulent mixing.

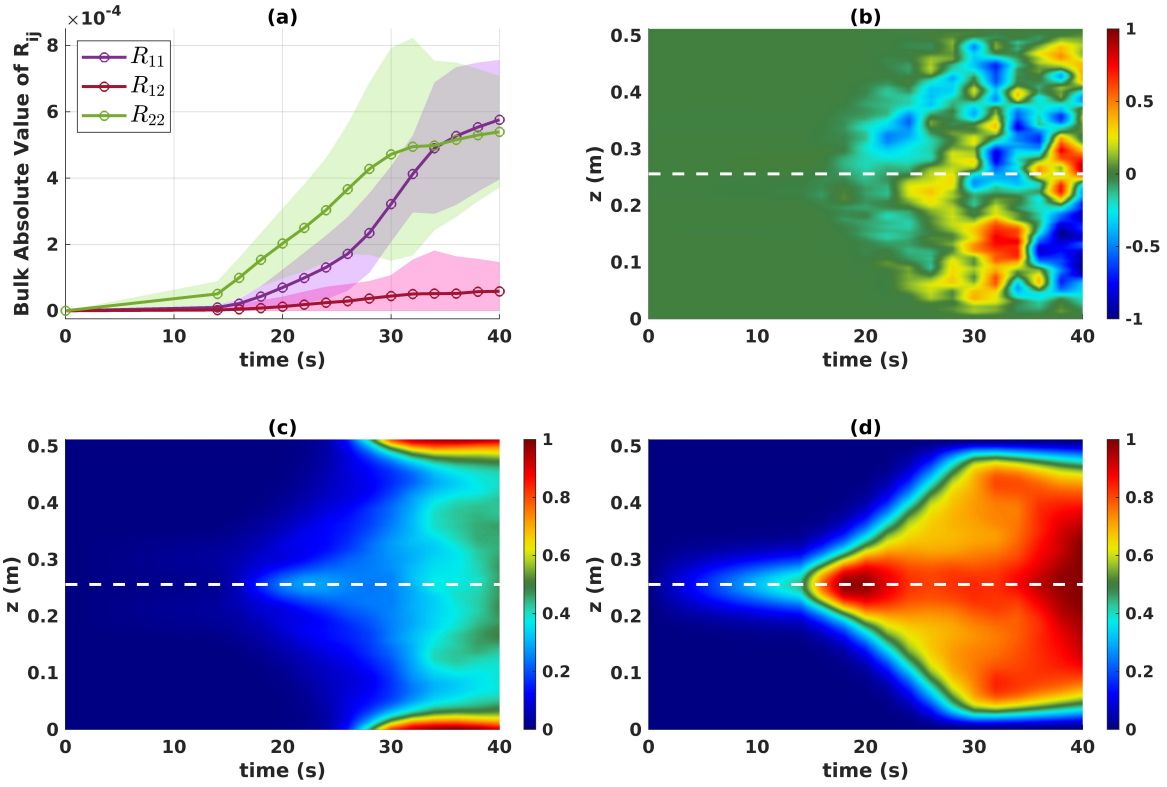


Figure 5.5: (a) Bulk absolute Reynolds stresses, with shaded areas extending two standard deviations away from the mean. Normalized Reynolds stresses (b) R_{12}, (c)R_{11}, and (d)R_{22} integrated with respect to x.

5.2.2 Reynolds Stresses

The bulk absolute values of the Reynolds stresses are depicted as functions of time in panel (a) of Figure 5.5. The shear stress is much weaker than the other stresses (though still on the same order of magnitude) and we note R_{22} varies the most between ensemble members. Panels (b) though (d) show the normalized Reynolds stresses integrated with respect to x as a function of z and time. The dashed white lines indicate the initial height of the mean density stratification. From panel (d) we see that R_{22} spreads symmetrically from the location of the initial stratification, which is in agreement with RT theory. The spatial distribution of R_{11}, panel (b), indicates that fluctuations in the horizontal velocity are symmetrical in z, greatest along the sidewalls, and take longer to increase than those in the vertical. The distribution of the shear stress is very different from those of R_{11} and R_{22}. There is no symmetry around the initial stratification, nor is there a coherent pattern.

An eddy viscosity parametrization relates the Reynolds stress tensor to the mean rate of strain and turbulent kinetic energy (TKE) as follows[72]

$$-R_{ij} = \nu_e \bar{S}_{ij} - k\delta_{ij}, \tag{5.6}$$

where

$$\bar{S}_{ij} = \frac{1}{2}\left(\frac{\partial U_i}{\partial x_j} + \frac{\partial U_j}{\partial x_i}\right), \tag{5.7}$$

is the mean rate of strain and

$$k = \frac{1}{2}(\overline{u'u'} + \overline{w'w'}). \tag{5.8}$$

is the TKE. The Kronecker delta is denoted by δ_{ij}, and ν_e is a phenomenological constant that needs to be selected as the "best" representation of the turbulence. Like the components of R_{ij}, k would be an unknown quantity in a RANS simulation. We have an ensemble of DNS simulations and so, we have access to both the averaged, and fluctuating quantities. The turbulent kinetic energy, k, is shown in Figure 5.7 as (a) a function of depth and time, and (c) as a bulk quantity. The mean kinetic energy, $K = \frac{1}{2}(U^2 + W^2)$, is similarly shown in panels (b) and (c). The turbulent kinetic energy exceeds the mean kinetic energy by two orders of magnitude and so we expect fluctuations in the velocity fields to have a significant impact on the tracer distribution.

Since we are interested in the downward propagation of the tracer front due to the

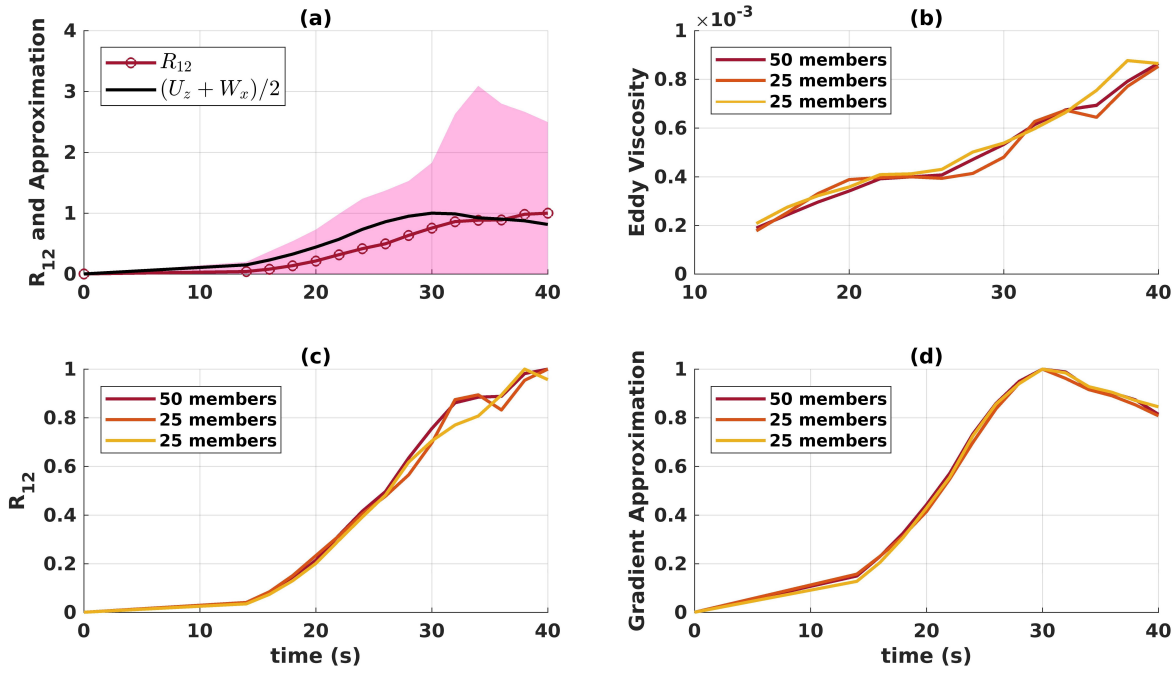


Figure 5.6: (a) Normalized bulk mean Reynolds stress R_{12} with shaded areas extending two standard deviations away from the mean and corresponding normalized bulk gradient approximation $(U_z + W_z)/2$ calculated with all 50 ensemble members. (b) Time-dependent eddy viscosities from equation 5.6. (c) Normalized R_{12} and (d) normalized gradient approximations for the entire ensemble and two unique subsets of 25 members.

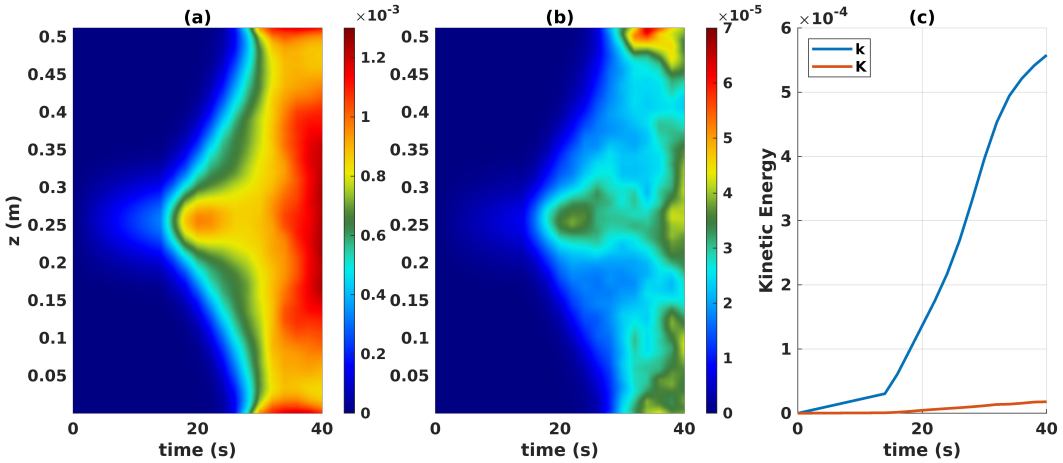


Figure 5.7: (a) Turbulent kinetic energy given by equation 5.8 integrated with respect to x. (b) Kinetic energy of the mean integrated with respect to x. (c) KEs integrated in x and z (TKE in blue and KE of mean in orange).

downward transport of horizontal momentum, we focus on the R_{12} component in what follows. The spatial distribution of R_{12} can be obtained from our data. So, we diagnose a time-dependent eddy viscosity defined as

$$\nu_e = \frac{\bar{S}_{12}}{R_{12}} \tag{5.9}$$

In panel (a) of Figure 5.6 the absolute value of the off-diagonal component of the Reynolds stress tensor is integrated in space and normalized. The shaded area extends two standard deviations (calculated using $u'w'$ from each ensemble member) away from the Reynolds stress and is scaled by $\max(|R_{12}|)$. The black line indicates the normalized eddy-viscosity approximation given by the right-hand side of equation 5.6. The trend in R_{12} is not well represented by the corresponding entry in the mean rate-of-strain tensor, $\bar{S}_{12}$. While R_{12} increases monotonically, the eddy-viscosity approximation reaches its maxima at $t = 30$s and then begins to decrease. The calculations were performed with the entire ensemble as well as two unique subsets of 25 members each. In panels (c) and (d) we see that the normalized quantities collapse to nearly the same curve no matter the number or set of ensemble members considered. Panel (b) of Figure 5.6 shows the time-dependent eddy viscosity obtained according to equation 5.9. Once again, the trend in the eddy viscosity is largely unaffected by the ensemble members used for the calculation.

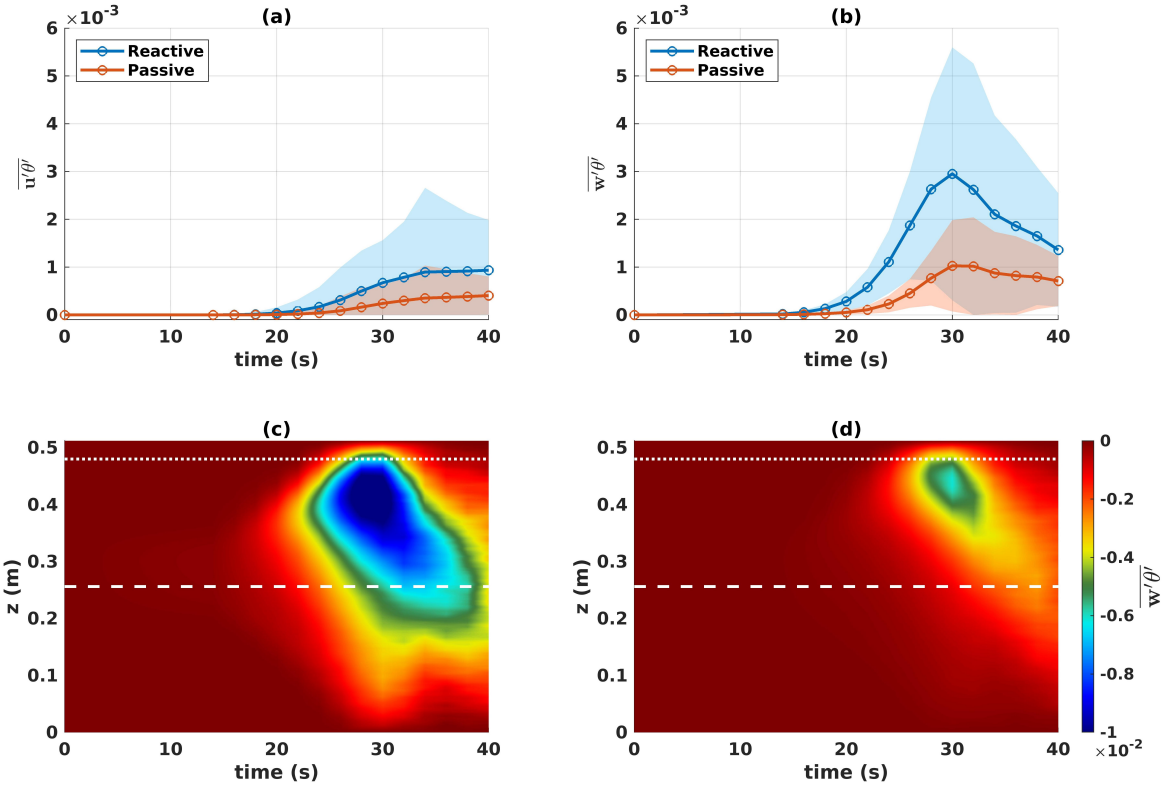


Figure 5.8: Bulk absolute value of the (a) horizontal and (b) vertical eddy fluxes of the reactive (blue) and passive (orange) tracers. Vertical eddy fluxes integrated with respect to x for the (c) reactive and (d) passive tracers.

5.2.3 Eddy Fluxes

Eddy fluxes quantify the mean transport of tracer fluctuations by fluctuations in the velocity fields. In section 5.2.2 the evolution of the fluctuations in the velocity fields was discussed. We saw that fluctuations in the vertical velocity component spread symmetrically from the location of the initial density stratification, while fluctuations in the horizontal one are largely found along the top and bottom boundaries. In Figure 5.8, we compare the bulk absolute horizontal and vertical eddy fluxes in panels (a) and (b) for the reactive (blue) and passive (orange) tracers. In section 5.2.1 we saw that reactive tracer fluctuations are larger than those of the passive tracer. It thus comes as no surprise that the eddy fluxes corresponding to the reactive tracer are larger than those of the passive tracer.

Despite the magnitudes of the horizontal, R^{11}, and vertical, R^{22}, Reynolds stresses being

similar, it is clear from Figure 5.8 that the tracer fluctuations are more closely correlated with the vertical velocity fluctuations than the horizontal ones. Around $t = 30$s, the heads of all the RT plumes have collided with the vertical boundaries. At this time, the vertical eddy fluxes reach their maxima and subsequently decrease because the tracers cannot be advected any further in the vertical. This decrease is more dramatic for the reactive tracer because it is affected by both the top and bottom boundaries having been entrained into a greater portion of the domain than the passive tracer which is not significantly affected by the RT plumes reaching the bottom boundary.

In panels (c) and (d) of Figure 5.8, the vertical eddy fluxes of the reactive and passive tracers are integrated with respect to x and shown as functions of depth and time. The dotted white lines indicate the inflection point of the hyperbolic tangent function describing the initial tracer distribution and the dashed lines indicate the initial height of the mean density stratification. For both tracers, the vertical eddy fluxes are negative because the fluctuations are travelling downwards. The heights at which the eddy fluxes first become nonzero align with the locations of the tracer fronts. The reactive tracer fluctuations and fluctuations in the vertical velocity field both propagate upwards (Figures 5.3 and 5.5) making the vertical eddy flux propagate upwards. This does not necessarily imply that the fluctuations are being transported upwards. Rather, it tells us that the fluctuations develop higher in the domain as concentration is pulled from the ensemble mean. These space-time plots further support the conclusion that the decrease seen in the bulk absolute vertical eddy flux of the reactive tracer is more dramatic because fluctuations in the passive tracer barely reach the bottom of the domain.

When running RANS simulations, eddy diffusivity parameterizations of the form

$$-\overline{u'\theta'} = \kappa_H \frac{\partial \theta}{\partial x}, \qquad -\overline{w'\theta'} = \kappa_V \frac{\partial \theta}{\partial z}, \tag{5.10}$$

are often used to model the unknown eddy fluxes. In section 5.2.2, we saw that the eddy viscosity parameterization does not capture the same trends as the off-diagonal Reynolds stresses if the eddy viscosity is assumed to be constant. This does not inspire much confidence in the performance of the analogous eddy diffusivity parameterization. In panels (a) and (b) of Figure 5.9 the normalized bulk absolute eddy fluxes are plotted along with the normalized right-hand sides of the equations in 5.10. The tracer derivatives taken with respect to x capture the general behavior of the horizontal eddy fluxes but fail to capture the details. The horizontal eddy fluxes start increasing earlier and are starting to plateau by the ends of the simulations.

The tracer derivatives taken with respect to z fail to capture even the general behavior

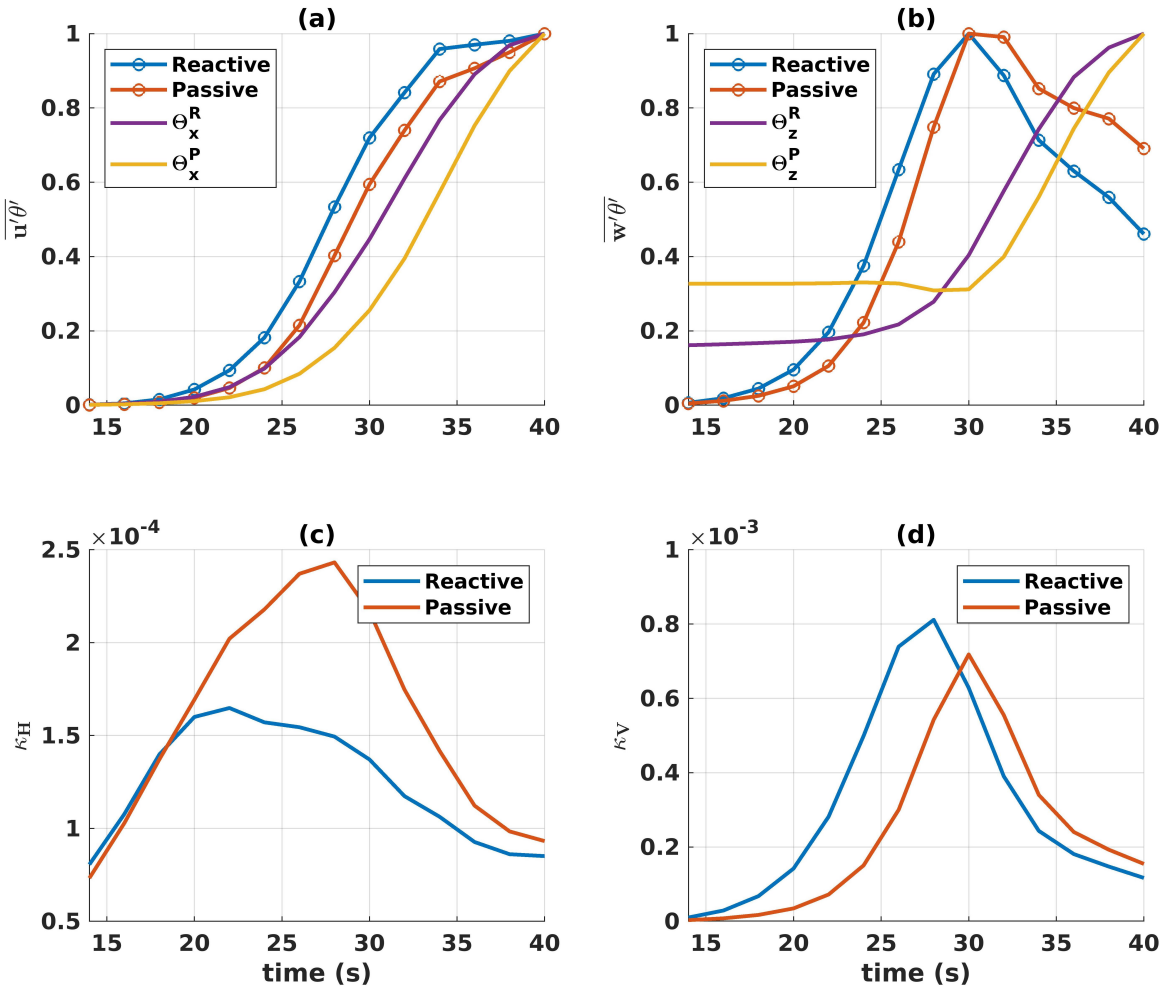


Figure 5.9: Normalized bulk absolute values of the (a) horizontal and (b) vertical, eddy fluxes of the reactive (blue) and passive (orange) tracers. The bulk absolute values of the derivatives of the mean tracers are plotted for comparison. Time-dependent (c) horizontal and (d) vertical eddy diffusivities.

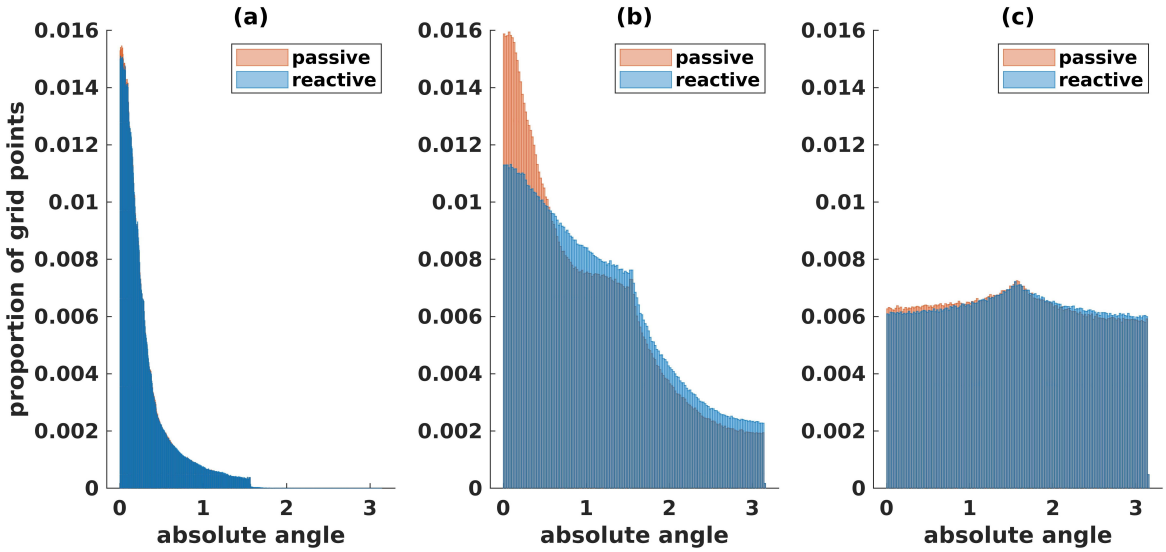


Figure 5.10: Absolute angle between the eddy flux and gradient of the mean at (a) $t = 14$s, (b) $t = 26s$, and (c) $t = 40s$ quantified as a proportion of the total number of grid points.

of the vertical eddy fluxes. In particular, they do not capture the peak and subsequent decrease shown in the blue and orange curves of panel (b) in Figure 5.9. Rather, they increase almost monotonically (the exception being in the z derivative of the mean passive tracer around $t = 30$s). Due to the initial tracer stratifications, the derivatives with respect to z are initially non-zero whereas fluctuations in the velocity and tracer fields are initially zero by construction. Fluctuations in the velocity field only begin to appear as the Rayleigh-Taylor instabilities develop. Therefore, there is a clear mismatch between the vertical eddy fluxes and their eddy diffusivity parameterizations.

As previously discussed, the vertical eddy fluxes peak when tracer fluctuations reach the bottom of the domain. Eddy diffusivity parameterizations consider the gradient of the tracer mean, which only begins to reach the bottom boundary when the simulations are stopped and the tracer is well-mixed. In panels (c) and (d), we plot the corresponding vertical and horizontal eddy diffusivities obtained from dividing the parameterizations through by the tracer derivatives. The horizontal eddy diffusivities are an order of magnitude smaller than the vertical ones. The variability in the values brings the use of constant eddy diffusivities into question.

Bulk descriptions do not capture any information about the directions of the eddy fluxes or gradients. The angle between the vectors (Θ_x, Θ_z) and $(-\overline{u'\theta'}, -\overline{w'\theta'})$ can be calculated

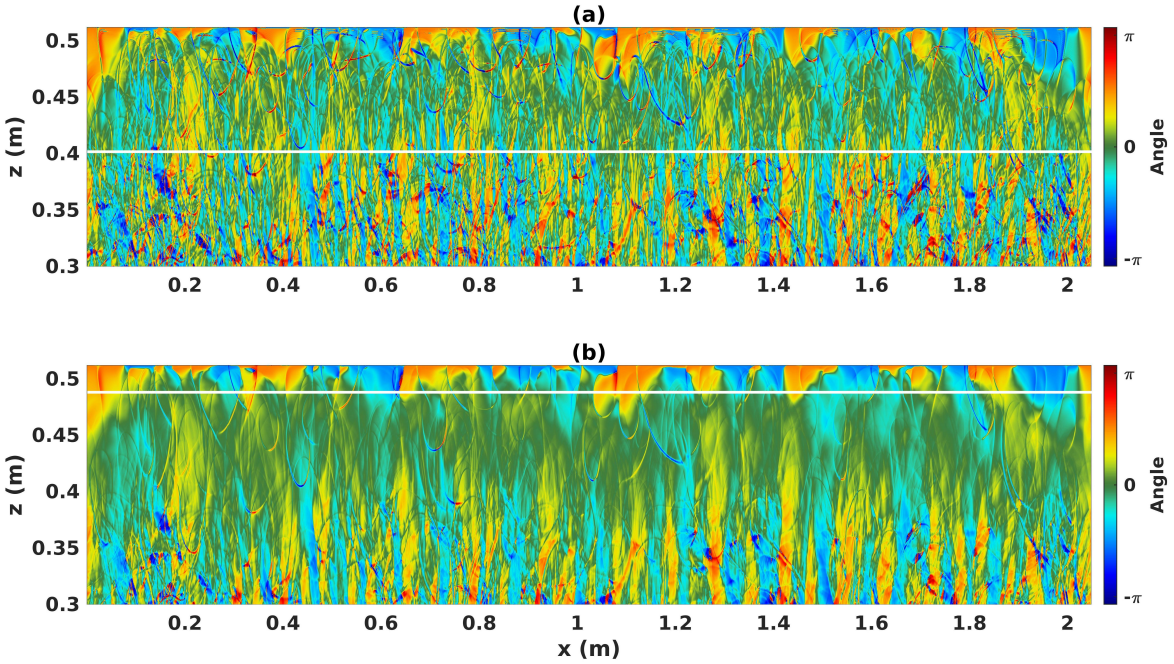


Figure 5.11: Angle between the eddy flux at gradient for the (a) reactive and (b) passive tracers at $t = 26$s.

at each grid point and indicates whether the eddy diffusivity parameterization is diffusing the tracer in the correct direction. Figure 5.10 presents the distribution of the grid points as a function of the absolute value of the angle between (Θ_x, Θ_z) and $(-\overline{u'\theta'}, -\overline{w'\theta'})$. Note that the absolute angle is in $[0, \pi]$ with a value of π indicating that the vectors are antiparallel. In this case, a negative eddy diffusivity would be required to realign them. The panels in Figure 5.10 show the distribution of angles at (a) $t = 14$s, as the RT instabilities are just forming, (b) $t = 26$s when the RT plumes are large but have not reached the boundaries, and (c) $t = 40$s when the system is well-mixed. For early times, the distribution indicates that the eddy fluxes and gradient of the mean tracers are mostly aligned. The distribution then slumps towards π and becomes fairly uniform by the end of the simulations. The eddy diffusivity parameterization performs better for the passive tracer than the reactive one, especially for intermediate times.

The spatial distribution of the angles in the upper portion of the domain is shown in Figure 5.11 at $t = 26$s for the (a) reactive and (b) passive tracers. At this time, Figure 5.2 shows that the mean front of the reactive tracer fluctuates around $z = 0.4$m and that of the passive tracer fluctuates around $z = 0.48$m (white lines in Figure 5.11). The alignment of (Θ_x, Θ_z) and $(-\overline{u'\theta'}, -\overline{w'\theta'})$ is best within the tracer band for the reactive tracer and directly beneath the tracer front for the passive tracer. Along the top boundary, the gradient and fluxes are generally perpendicular to one another. The mean tracer gradients do not take the effect of boundary conditions into account. The somewhat regular pattern in the distribution of the angle values along the top of the domain is the result of rising plume heads pushing fluid horizontally and downwards. Meanwhile, the tracer gradients are primarily pointing downwards, as the mean tracers lie in bands along the top of the domain. Therefore, the angles are primarily $\pm\pi/2$ in this region. So, while the eddy fluxes reflect properties of the flow governing the tracer transport, the gradients only reflect the spatial distribution of the mean tracer field.

The plumes formed by RT instabilities primarily move vertically, though the perturbations applied to the initial density stratification do encourage some plumes to propagate diagonally. If we consider the mean initial stratification, the perturbations average out. So, the mean effect of the RT instabilities is to transport the tracers vertically until turbulent mixing becomes strong enough to induce horizontal transport. At $t = 26$s, the mixing is strongest in the region where the eddy flux and gradient vectors are most aligned. In the passive tracer case, panel (b), we note that between $z = 0.3$m and $z = 0.4$m, the angle distribution is loosely arranged into columns. This is also true for the reactive tracer, panel (a), but less obvious because the reactive tracer fluctuations are larger and spread lower into the domain as the RT bubbles have already reached the tracer front, making the angle distribution more disordered. As previously mentioned, the increased Fickian

diffusion exhibited by the reactive tracer will allow it to diffuse into turbulent structures and then be transported to regions the passive tracer may struggle to reach. The reaction then causes this process to be repeated, enriching the fluctuation field.

5.3 Reynolds Averaged ADR Simulations

Performing *a priori* RANS was useful for developing intuition around how Reynolds averaging affects the representation of a reactive tracer within a turbulent environment. We now wish to investigate whether solving the RAADR equation will generate tracer distributions similar to the Reynolds averaged ones calculated from the solution to the full ADR equation.

Rather than solve the RANS equations, we use the ensemble mean velocity field in the RAADR equation. The data from the ensemble allows us to calculate eddy flux and eddy reaction terms rather than having to rely on parameterizations. By calculating these values from the ensemble data, we retain some level of consistency between the ensemble mean representation of the reactive tracer field and the values generated by the RAADR equation.

In solving the RAADR equation, we keep the domain and resolution consistent with the ensemble. All parameters have the same values as those used for the ensemble, given in table 5.1. We use the same reaction function given by equation 5.4. The velocity fields are taken to be the ensemble mean velocities. The ensemble outputs data every 2 seconds starting at $t = 14$s and ending at $t = 40$s, so the velocity values are updated every 2 seconds in the RAADR simulation as are the eddy flux and eddy reaction terms. We take the mean state of the ensemble at $t = 14$ s to be the initial condition and solve the RAADR equation with the numerical method described in section 3.3. The timestep is taken to be $dt = 1 \times 10^{-3}$s and simulation data are saved every 2 seconds so that the output times are the same as those of the ensemble. It may be argued that this is somewhat of a crude solution method, but it proves to be sufficient for identifying the qualitative differences between the RAADR solution and the ensemble mean. To isolate the effects of the eddy fluxes and eddy reactions, we run four simulations:

S – Base simulation with eddy fluxes and eddy reactions set to zero.

SF – Simulation with eddy fluxes calculated from ensemble data and eddy reactions set to zero.

SR – Simulation with eddy fluxes set to zero and eddy reactions calculated from the ensemble data.

SFR – Simulation with both eddy fluxes and eddy reactions calculated from the ensemble data.

By constructing the simulations in this way, we can identify the individual impacts of the eddy fluxes and eddy reaction on the reactive tracer and any feedbacks that result from the combination of both terms. Note that since there are no eddy reaction terms in the equation for the passive tracer, we only need to consider simulations S and SF to observe the effect of the eddy fluxes.

5.3.1 RAADR Simulation Results

In Figure 5.12, we show the passive tracer integrated over x as a function of depth and time. In panel (a) we have a sample ensemble member. We see that around $t = 30$s the tracer begins to be transported downwards. Looking at the ensemble mean, panel (b), we see that the downward transport of the tracer is smoothed. We can therefore deduce that the pattern in (a) is, unsurprisingly, the result of fluctuations. The solution to the RAADR equation (with a reaction term of 0 for the passive tracer), neglecting the eddy fluxes is shown in panel (c). The tracer evolution differs significantly from that demonstrated by the ensemble mean. We see a uniform front at nearly all times and no downwards propagation. In panel (d), we have the RAADR solution, this time including the effects of eddy fluxes. The eddy fluxes push the tracer front upwards and sharpen it, but do little to encourage the downward transport observed in panels (a) and (b).

Figure 5.13, panels (a)-(d), show the analogous quantities for the reactive tracer. Once again, in panel (a) we observe fluctuations in the downward transport of the reactive tracer in a sample ensemble member. This transport is smoothed in the ensemble mean, panel (b), but otherwise remains qualitatively similar. When we consider the result of simulation S, panel (c), we see a strong tracer front that grows downwards, but it is not transported into the lower portion of the domain. The effect of the eddy fluxes in simulation SF is to once again push the tracer front upwards, panel (d). When the eddy reactions are considered alone, panel (e), we see a similar effect in slowing the downwards propagation of the tracer. The combined effect of the eddy flux and reaction terms is to push the tracer front even higher for later times so that it reaches its deepest point near the middle of the simulation.

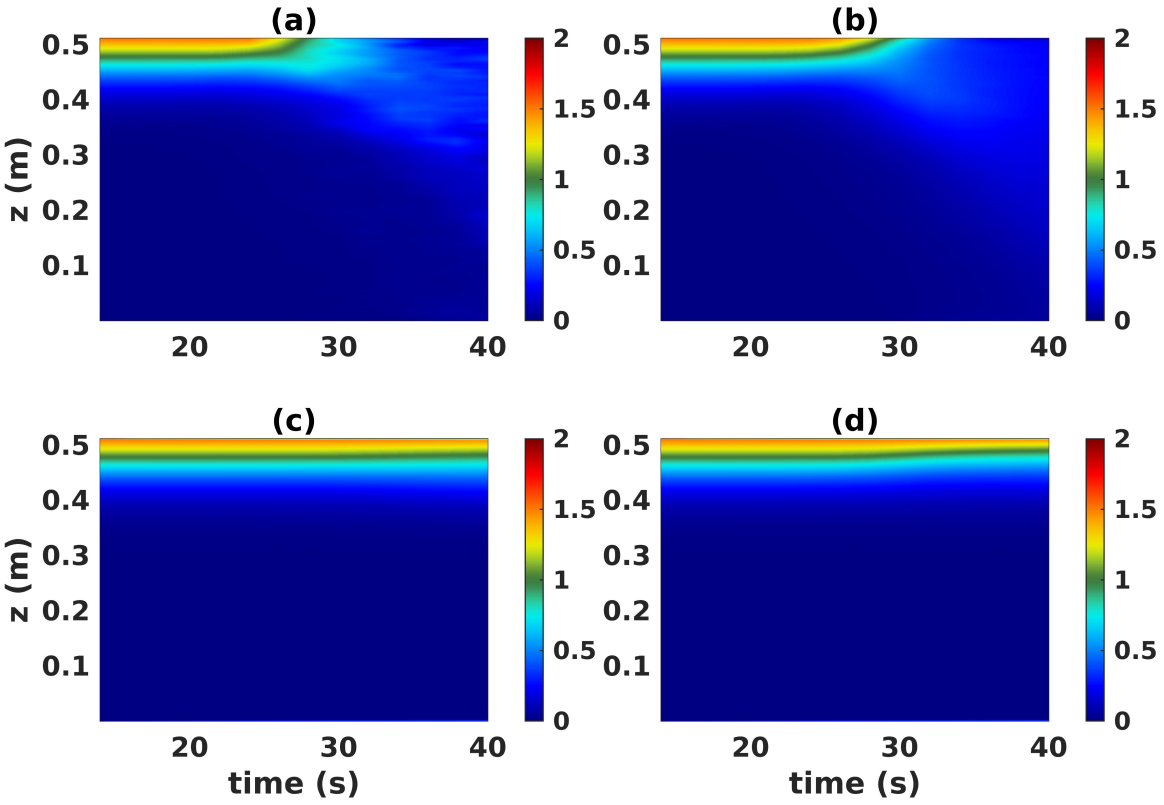


Figure 5.12: Passive tracer concentration integrated with respect to x from (a) a sample member, (b) the ensemble mean, (c) simulation S, and (d) simulation SF.

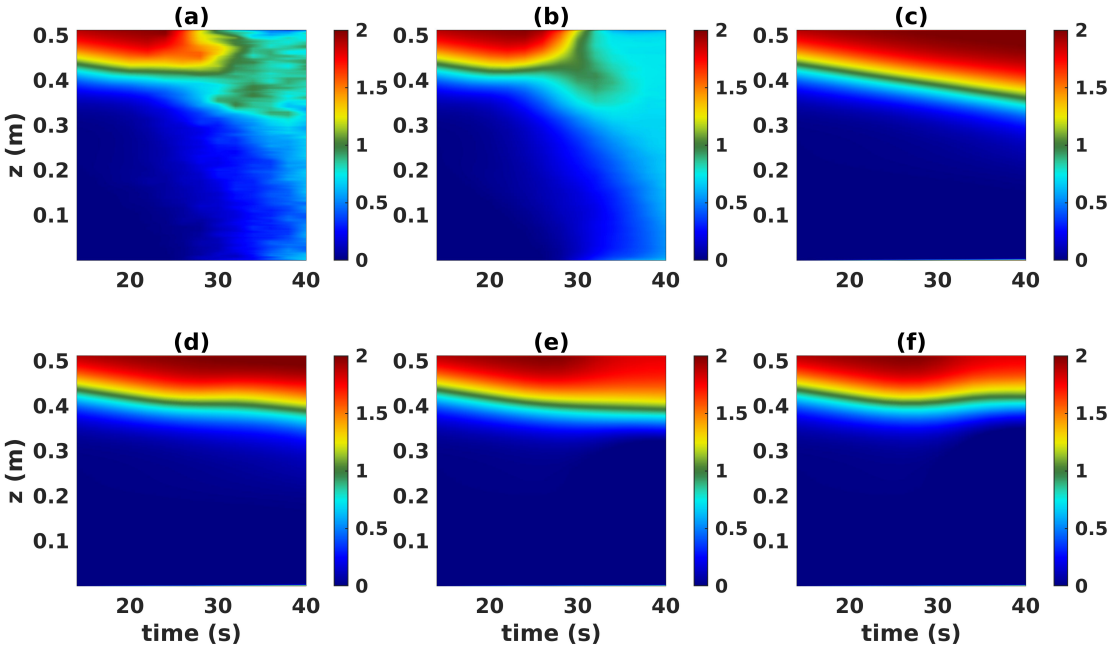


Figure 5.13: Reactive tracer concentration integrated with respect to x and plotted as a function of z and time. The panels correspond to (a) a sample member, (b) the ensemble mean, and simulations (c) S, (d) SF, (e) SR, and (f) SFR.

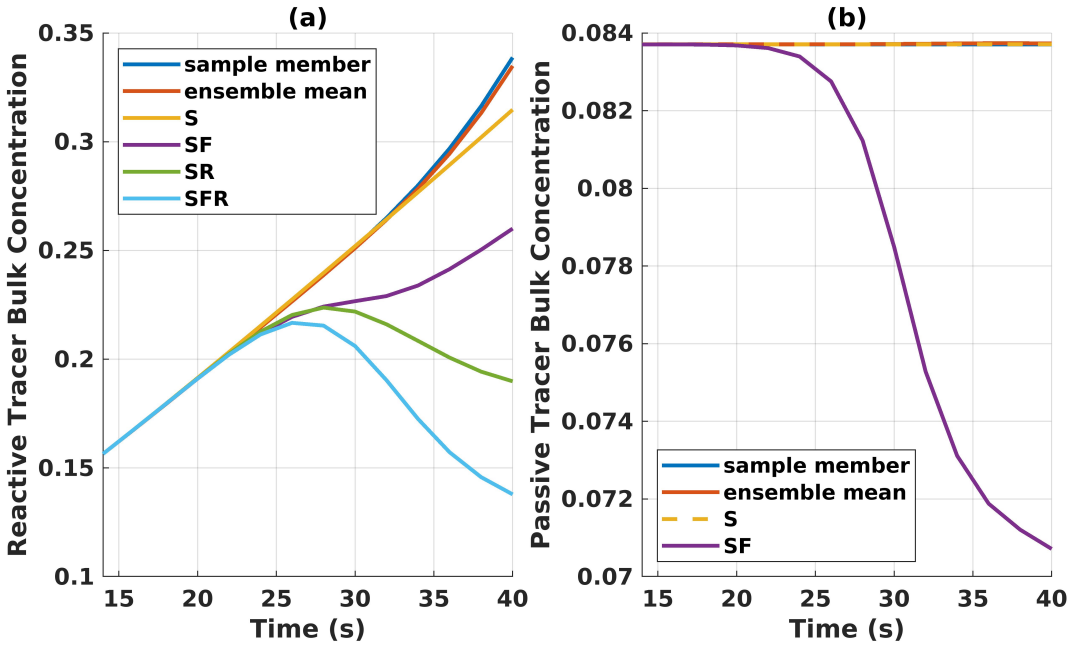


Figure 5.14: Bulk (a) reactive and (b) passive tracer concentrations for a sample member, the ensemble mean, and the pseudo-RANS simulations.

In Figure 5.14, the differences in the bulk concentrations of the (a) reactive and (b) passive tracers can be observed for each of the simulations we have just discussed. The pseudo-RANS simulations under-estimate the amount of reactive tracer in the domain, especially when both eddy fluxes and reactions are considered. It is not surprising that the eddy reactions should reduce the amount of tracer given that they introduce a sink into the equation governing the evolution of the mean. However, it is perhaps unexpected that the eddy fluxes would cause the amounts of both the reactive and passive tracers to be reduced. As indicated by the space-time plots, it seems the effect of the eddy fluxes is to push the tracers against their gradients and prevent their spread lower into the domain. This implies that any areas with non-zero reactive tracer concentration are more likely to have concentration values near the stable equilibrium of one (i.e. the tracer is distributed over a smaller area and thus more concentrated). The eddy fluxes therefore prevent both the downward spread of the tracer and the increase in the total amount of reactive tracer.

In Figure 5.15, the final reactive tracer field in each of the simulations is shown. By comparing (a) the sample member with (b) the ensemble mean and (f) simulation SF, we see that the three are simply not comparable. This will be revisited in the discussion.

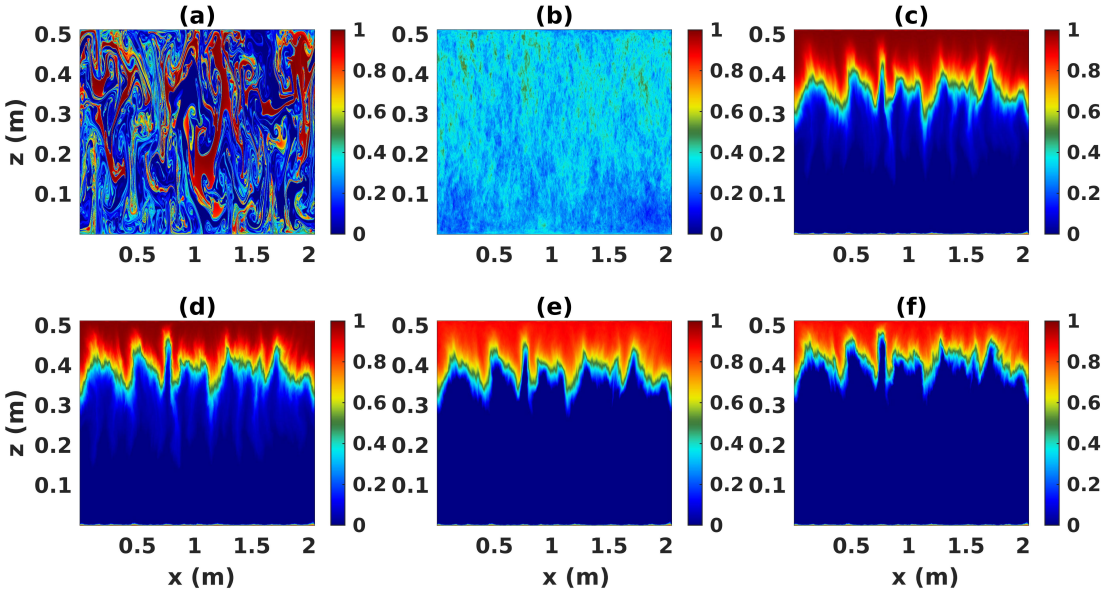


Figure 5.15: Reactive tracer concentration at $t = 40$s. The panels correspond to (a) a sample member, (b) the ensemble mean, and simulations (c) S, (d) SF, (e) SR, and (f) SFR.

5.4 Conclusions

Turbulent flows are highly unpredictable and disordered. Small $O(10^{-2})$ perturbations to the shape of the initially unstable density stratification were enough to produce significant variability within an ensemble of 50 well-resolved simulations. RANS simulations implicitly assume that the most important dynamics are captured by the mean. We have shown that this assumption fails when considering the transport of a reactive tracer growing according to Fisher's equation.

Under Reynolds averaging, the mean reaction equation is altered by the introduction of eddy reaction terms. The procedure in Section 2.4.2 can be applied to any polynomial reaction function and extended to non-polynomial functions if they can be approximated with a Taylor polynomial. The procedure allows the roles of the mean, fluctuations, and mean-fluctuation interactions in the Reynolds-averaged reaction function to be isolated. It also tells us that any terms raised to an even power will introduce fluctuation dependent sources or sinks (depending on the sign of the coefficient) into the mean ADR equation. For Fisher's equation, a sink in the mean ADR equation transfers concentration from the mean to the fluctuations. Growth, whether in the mean or fluctuations, increases diffusion, allowing the reactive tracer to spread to parts of the domain that the passive tracer may struggle to reach. These areas may include turbulent structures, further transferring concentration from the mean to the fluctuations. Diffusion and turbulent mixing push the tracer concentration away from its stable equilibrium, $\theta = 1$, thereby promoting further growth and creating a positive feedback loop. Numerical dispersion, while not significant in our pseudospectral simulations, has the potential to artificially increase the diffusivity of a tracer. The positive feedback would, thus, be intensified in an inherently dissipative model (i.e., one based on finite volumes) such as ROMS [17].

Due to the flux of concentration from the mean to the fluctuations, the mean underestimates the tracer concentrations in the individual simulations. Further, as shown by the supplementary movies, the downwards propagation of the reactive tracer is captured by the fluctuations and not the mean. In a true RANS simulation, one has no knowledge of the Reynolds stresses, eddy fluxes, or eddy reactions. In our numerical experiment, these quantities have proven to have a significant effect on the downward propagation of the reactive tracer. The bulk scalar variances (which are also the eddy reactions for Fisher's equation) for both the passive and reactive tracers are approximately one quarter of the magnitude of the corresponding bulk mean and, thus, certainly non-negligible.

Given the initial distribution of the tracers (panel (b) of Figure 5.1), the generation of turbulent mixing with an RT instability doomed the eddy diffusivity relations to fail. RT

bubbles pushed up against the tracer fronts, causing counter-gradient fluxes and negative eddy diffusivities. As the fronts of the RT plumes hit the top and bottom of the domain, the flow transitioned from a state dominated by large-scale motions to one dominated by smaller-scale turbulent mixing. In the latter state, negative eddy diffusivities continue to be observed because the largest eddies are larger than the curvature of the mean vertical tracer profiles [52]. The reactive tracer fluctuations associated with the reaction–turbulence–diffusion feedback that was previously discussed can spread into large turbulent structures more easily than passive tracer fluctuations. Therefore, one would expect more counter-gradient flux associated with the reactive tracer, which is exactly what is observed in Figure 5.10. Negative eddy diffusivities have been observed in numerical studies of non-passive oceanic tracers and attributed to symmetric instabilities and other submesoscale phenomena [84], in agreement with the results presented herein. We would expect an eddy diffusivity parameterization to perform just as badly if not worse for the same setup in three dimensions since the eddy diffusivity parameterization does not account for vortex tilting [109].

When comparing the results from a single simulation, the *a priori* RANS quantities, and the quantities obtained from solving the RAADR equation, Figure 5.15, we see that the three provide entirely different representations of a system. Despite the eddy fluxes and eddy reactions being calculated from the ensemble data, the quantities from the pseudo-RANS simulations are very different from the Reynolds averaged quantities obtained from the data. In particular, there is a lack of downward transport for both the reactive and passive tracer, likely due to cancellations in the calculation of the averaged vertical velocity. The inclusion of the eddy reactions and fluxes reduced the downward transport even further, contrary to what one might expect.

The simulations presented herein are two-dimensional and thus cannot capture some aspects of oceanic flows. However, they do provide a simple turbulent $x - z$ flow and demonstrate that the coupling between turbulence and the reaction dynamics should not be ignored. This is an improvement over the toy flows that have been used to study the reaction dynamics of phytoplankton, for example [93]. Rayleigh–Taylor flows were chosen because they result in primarily vertical transport and the downward propagation of the reactive tracer front. To keep the computational demand of running the ensemble reasonable, our simulations and performed in a relatively small domain due to the requirement of 0.5 mm resolution for resolving the sharp reactive tracer fronts. Other flows may be more appropriate for representing convection in the oceanic boundary layer, and this is an area for future work.

5.5 Discussion

Due to the feedbacks observed between turbulent mixing and the reaction dynamics, we stress the importance of conducting studies of reactive tracers within turbulent flows. The use of convective cells to approximate turbulence is problematic, primarily because the cells introduce streamlines that the tracer can only diffuse across [93, 94]. In our study, turbulent RT-induced mixing created small, irregular structures that pulled the reactive tracer into parts of the domain it otherwise would have only reached due to diffusion. There was a significant amount of variability in the tracer distributions of our ensemble members. With pre-specified velocity fields, it would be nearly impossible to capture the structures that characterize turbulent mixing, and thus, variability in the tracer distribution would be underestimated.

In addition to the flow used to induce turbulent mixing, the results of this study are highly specific to the reaction and Damköhler number selected. We chose $Da \sim O(1)$ to balance the effects of advection with those of the reaction. The balance causes growth and mixing processes to become coupled and eddy diffusivity parameterizations to fail [74]. Ocean tracer dynamics are complex, so interactions between turbulent mixing and reaction dynamics are not as simple as the positive feedback we observed in our study [78, 44, 15].

When considering a slow reaction with $Da \sim O(0.1)$ or smaller, the coupling will be weaker, but new challenges arise as turbulent mixing creates sharp tracer filaments. Decreasing Da to $O(0.1)$ made our 0.5 mm grid spacing insufficient to resolve the tracer filaments. This is problematic given the large disparity between the scale of our simulations and those of any regional modeling study. Increasing the diffusivity of the tracer would smooth out the fronts, thereby reducing the demand for a higher resolution. In a RANS simulation, this is achieved through eddy diffusivity parameterizations. Modeling studies based on ROMS generally have a $O(1)$ to $O(10)$-kilometer horizontal resolution and $O(1)$ to $O(100)$-meter vertical resolution [51, 79, 89]. Therefore, it should be assumed that tracer distributions in these models have been over-smoothed. Further, the spacing between ROMS grid points is not uniform and the vertical resolution is often better near the surface than at the bottom (O(1 m) versus O(200 m) [44]). A possible improvement may be simulating near surface effects, which are weighted more heavily due to the grid spacing, while parameterizing those deeper in the domain.

Thanks to our relatively small simulations, we were able to run an ensemble with 50 members. However, for larger, more complex simulations, the question of how many ensemble members to run is a tricky one to answer. In the limit of infinite ensemble members, we would expect quantities such as $\partial\Theta/\partial x$ and $\partial U/\partial z$ to vanish. In fact, when

computing our results, we found that the mean tracer derivatives calculated with only half of the ensemble members demonstrated the same time-dependent trends, but had larger magnitudes. This was similar for R_{12} and the derivatives of the mean velocities. Therefore, we present the results of Figures 5.6 and 5.9 as normalized quantities and note that the eddy viscosity and diffusivities presented are functions of the ensemble members considered, though their orders of magnitude remain unaffected. This brings into question how many ensemble members one should run when conducting studies of this form. The limiting behavior of an infinitely large ensemble varies drastically from the behavior observed in an individual simulation. Perhaps this is a reason to consider large eddy simulations over interpretations based on Reynolds averaging.

Chapter 6

Large Eddy Simulations

In this chapter, we will be considering how spatial filtering affects the details conveyed by a dataset. To start, we will consider a simple two-dimensional toy model with a prescribed velocity field as described in section 6.1.1. The velocity field is intentionally chosen to only have two wavenumbers (one small and one large). This allows us to examine how the components of the residual stress tensor, the **sfs** flux term, and the **sfs** reaction term respond to the coarseness of a low-pass filter.

Next, we will extend the two-dimensional RT simulations discussed in Chapter 5 to three dimensions to create a truly turbulent flow and a sample dataset. The details are presented in section 6.2.1. We will consider the implications of various filter choices by examining the **sfs** flux and reaction terms.

6.1 Two-Dimensional Toy Model

6.1.1 Toy Model Setup

Table 6.1: Simulation parameters and dimensionless numbers for Toy Model

Simulation Parameter	Value
L_x	2 m
L_z	2 m
N_x	256
N_z	256
κ	1×10^{-2} m^2/s

In this section, we present a toy model in which the velocity fields are prescribed with known large scale and small scale components. The stream function used to define the velocity fields is

$$\psi(\vec{x},t) = 0.01 \sin\left(\frac{2\pi x}{L_x}\right) \sin\left(\frac{2\pi z}{L_z}\right) + 0.01 \sin\left(\frac{2\pi t}{T}\right) \sin\left(\frac{8\pi x}{L_x} + a\right) \sin\left(\frac{8\pi z}{L_z} + b\right). \tag{6.1}$$

The domain is $L_x = 2$m wide by $L_z = 2$m tall, with $N = 256$ grid points in either direction. We choose a timescale of $T = 0.1$ with which the magnitude of the small scale component of the stream function oscillates. The parameters a and b are randomly selected from a uniform distribution between 0 and 1 at each time step to randomly shift the spatial distribution of the small scale component. This introduces some stochasticity into the model to mimic the unpredictable nature of turbulence. The results derived from the toy model are independent of these parameters, and remain unchanged if the small-scale component of the velocity field is not shifted in space. Note that for the horizontal velocity component, u, we take $a \neq 0$ and $b = 0$ so that it is only shifted in the horizontal. Similarly, for the vertical velocity component, v, we take $a = 0$ and $b \neq 0$ so that it is only shifted in the vertical.

The initial tracer distribution for both the reactive and passive tracers is

$$\theta(\vec{x}, t = 0) = \exp(-20(x^2 + z^2))^4. \tag{6.2}$$

Figure 6.1 shows (a) the initial distribution of the tracer and (b) the large and (c) small components of the stream function.

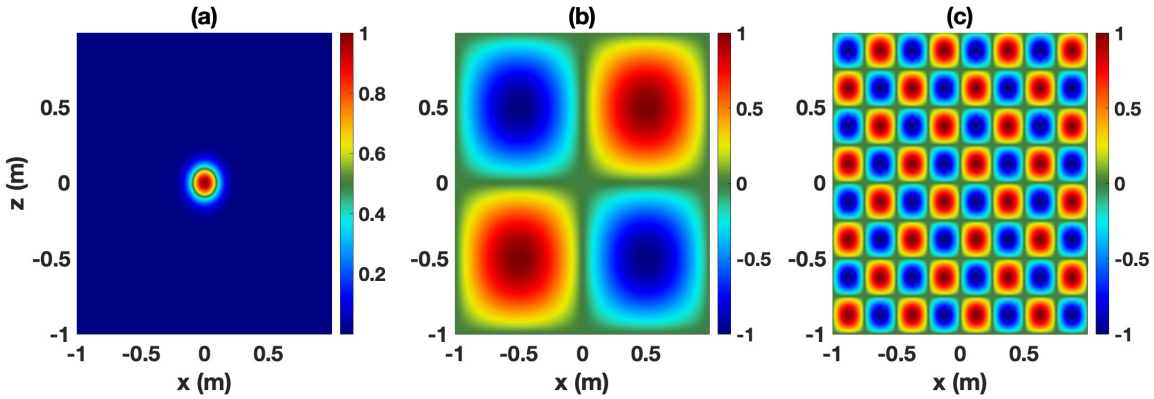


Figure 6.1: (a) Initial tracer distribution for both the reactive and passive tracers. (b) Large and (c) small scale components of the stream function.

The ADR equation is solved with Fisher's equation modified with a hyperbolic tangent,

$$F(\theta) = \alpha\theta(1-\theta)\tanh(\theta/0.001), \tag{6.3}$$

as the reaction term. The reaction rate is varied by using $\alpha = 0.1$, $\alpha = 1$, or $\alpha = 10$ in order to vary Da. The tracer diffusivity is taken to be $\kappa = 1 \times 10^{-2}$. The ADR equation is integrated with the numerical method described in section 3.3.

6.1.2 Spatial Filtering

The toy model has $N = 256$ grid points in both the x and z directions. The wavenumbers range from $(-N/2+1)\pi = -127\pi$ to $(N/2-1)\pi = 127\pi$. A low-pass filter is implemented which takes a cutoff wavenumber value as input. We define a "square" low-pass filter as

$$\hat{G}(k^{cut}) = (|k| < k^{cut}) \ \texttt{AND} \ (|l| < k^{cut}), \tag{6.4}$$

and a "circular" low-pass filter as

$$\hat{G}(k^{cut}) = \sqrt{k^2 + l^2} < k^{cut}. \tag{6.5}$$

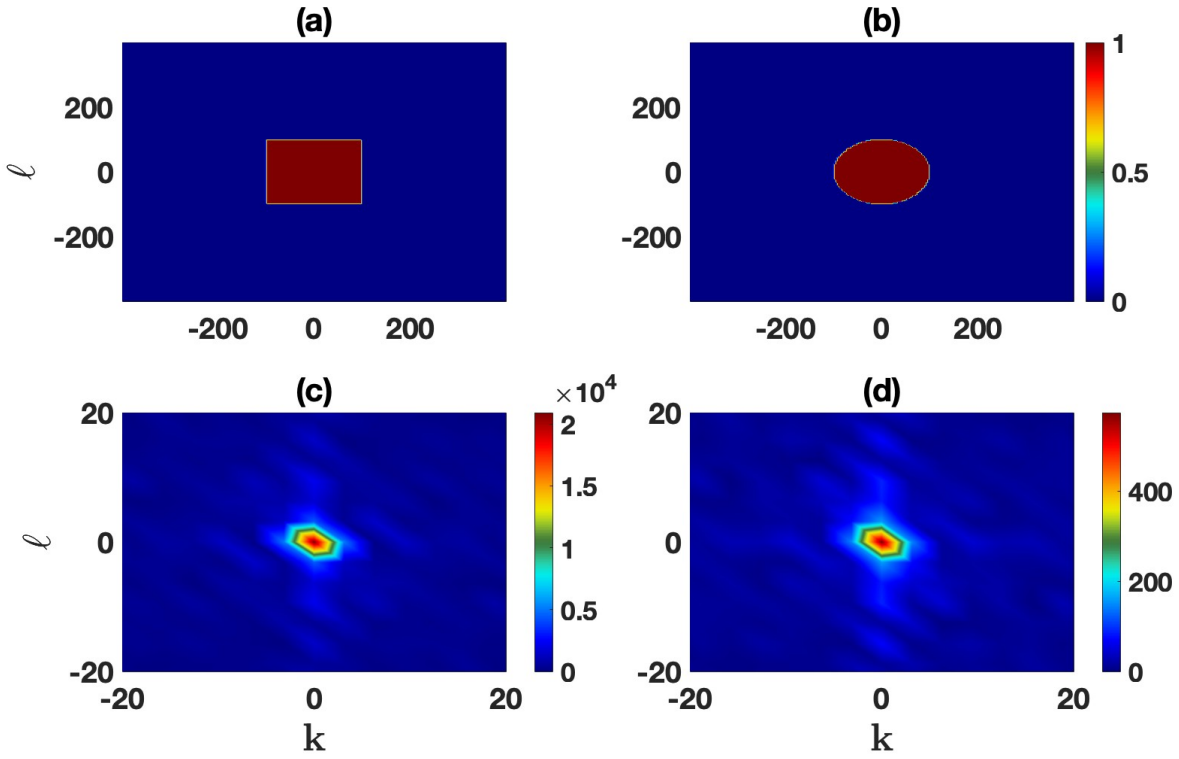


Figure 6.2: (a) Square and (b) circular filters with cutoff values of 100. (c) Reactive and (d) passive tracer power spectral densities at $t = 0.5$s.

For simplicity, we always take the cutoff value to be the same in all directions. Figure 6.2 shows the (a) square and (b) circular filters with $k^{cut} = 100$. For a square filter, the number of Fourier components retained after low-pass filtering can be calculated from the cutoff value as $n = 2(\lfloor k^{cut}/\pi \rfloor + 1)$. For a cutoff value of 100, only 64 Fourier components are retained.

Panels (c) and (d) of Figure 6.2 show the two-dimensional power spectral density of the reactive and passive tracers at the end of a simulation. The majority of the spectral power of the signals is contained in the smallest wavenumbers. With wavenumbers less than 20, nearly all of the signal can be captured.

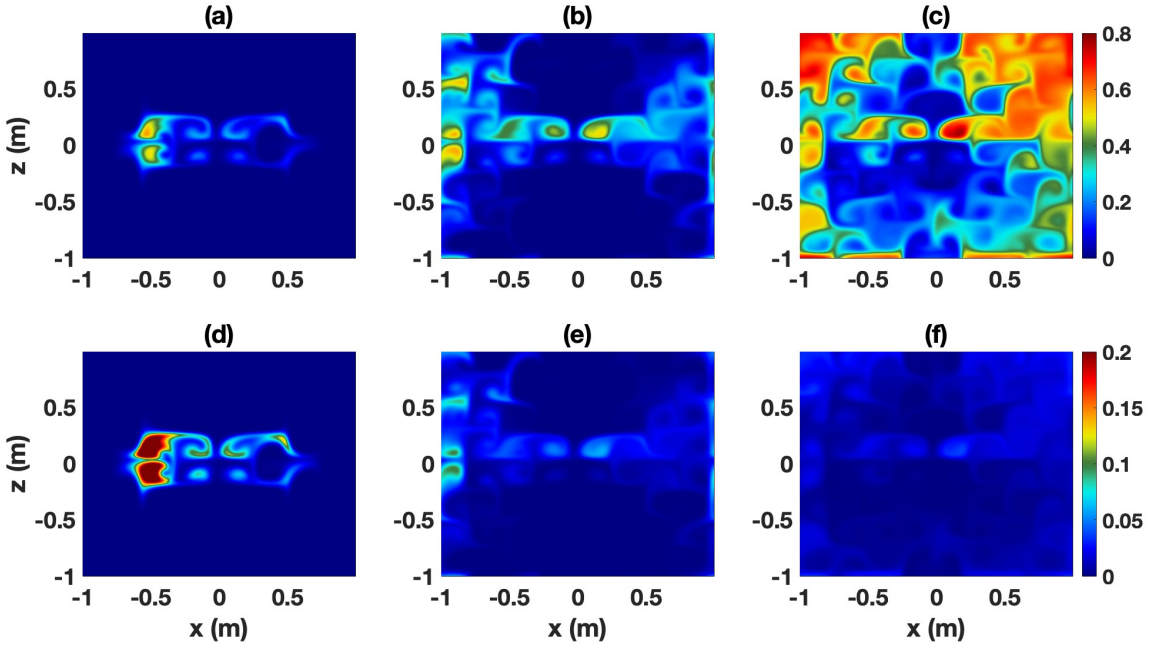


Figure 6.3: Evolution of the reactive (first row) and passive (second row) tracer distributions at $t = 0.1$s (a, d), $t = 0.3$s (b, e), and $t = 0.5$s (c, f). Note the difference in the colorbar limits in the two rows.

6.1.3 Toy Model Results

To understand the effects of spatial filtering, we must first establish a basis of comparison by considering the unfiltered data. In Figure 6.3, the evolution of the reactive (first row) and passive (second row) tracers is shown. Note the differences in the colorbar limits in each of the rows. The reactive tracer distribution spreads via advection and diffusion, resulting in growth in new parts of the domain. This behavior is consistent with what we observed in the two-dimensional Rayleigh-Taylor simulations in Chapter 5 though in this case we have a controlled, analytically specified velocity field. The large and small cells in the velocity field illustrate how the reactive tracer grows within a material volume (advective cell). The passive tracer exhibits simpler behavior in that advection and diffusion cause its distribution to tend towards a uniform state.

Prescribing the velocities allows us to control the scales present in the toy flow. The large scale component has a wavenumber of π while that of the small component is 4π. So we expect that for $k^{cut} > 4\pi$, the **sfs** components of the residual stress tensor will

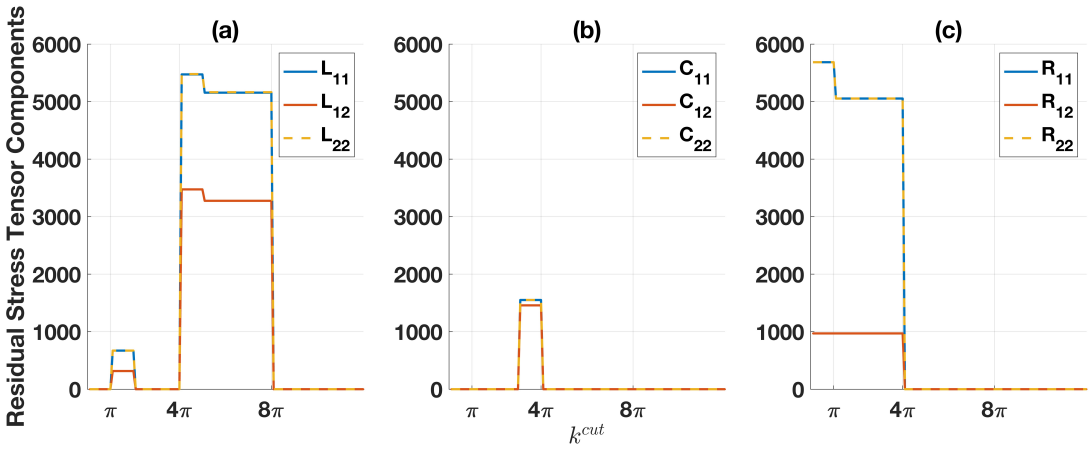


Figure 6.4: Time-averaged absolute (a) resolved, (b) cross-scale, and (c) sub-filter-scale components of the residual stress tensor plotted as a function of the wavenumber cutoff, k^{cut}.

go to zero. This is precisely what is observed in Figure 6.4 which shows the norm of the time-averaged absolute residual stress tensor components as a function of k^{cut}. In panel (c), the **sfs** components go to zero for $k^{cut} > 4\pi$. For $k^{cut} < \pi$, we see that only the **sfs** components are nonzero. Recall from section 4.2.2 that multiplication alters the active wavenumbers in a system. For the cross-scale terms to be non-zero we require that both $\langle u_i \rangle$ and u_j' be non-zero, which is the case for $\pi < k^{cut} \leq 4\pi$. Additionally, the multiplication of the two components must result in a resolvable wavenumber. Since $\sin(\pi x)\cos(4\pi x) = (\sin(3\pi x) + \sin(5\pi x))/2$, C_{ij} is only non-zero for $3\pi < k^{cut} \leq 4\pi$. The resolved components of the residual stress tensor are zero when $\langle\langle u \rangle\langle v \rangle\rangle = \langle u \rangle\langle v \rangle$ which occurs for $2\pi < k^{cut} < 4\pi$. Otherwise, as long as at least one component of each of u and v can be resolved, L_{ij} will be non-zero.

In Figure 6.5 we compare the unfiltered reactive tracer distribution, panel (a), with its low-pass filtered counterparts. The wavenumber cutoff used in the low-pass filter determines the amount of detail retained in the distribution. A particularly harsh filter with $k^{cut} = 10$, panel (b), results in a smeared distribution and makes it easy to identify differences between the filtered and unfiltered data. As k^{cut} is increased from 10 to 40, there is a clear improvement in the details captured by the filtered data. However, as k^{cut} is increased to 60 or 100, the details gained are not quite as obvious. This is not surprising since Figure 6.2 showed that the power spectral density is highly concentrated around low wavenumbers.

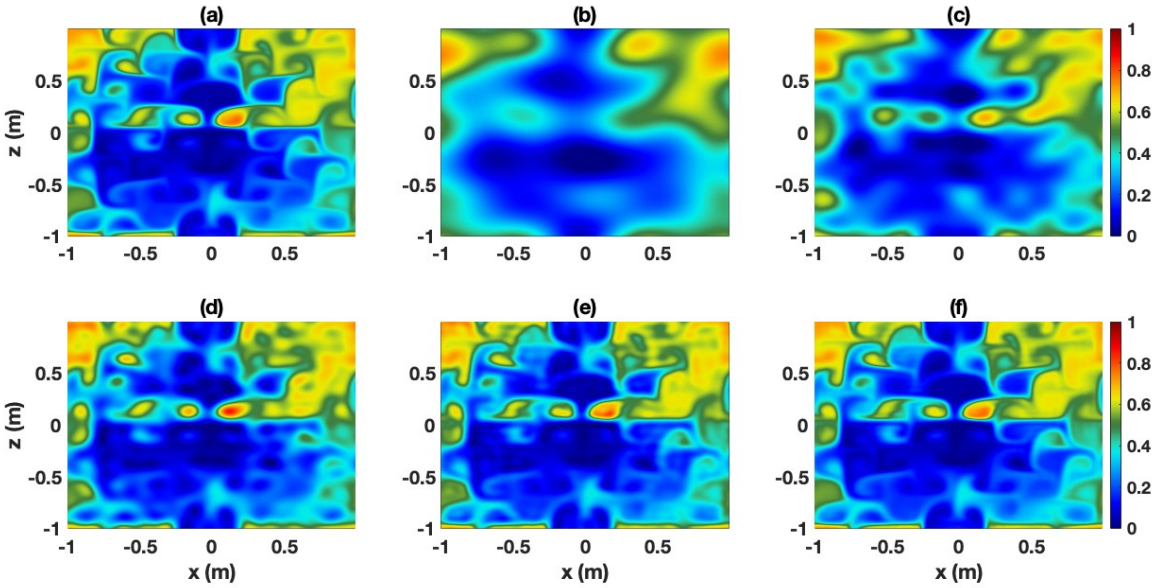


Figure 6.5: Figure 6.5: (a) Reactive tracer concentration at t = 0.5 s. Low-pass filtered reactive tracer concentration with cutoffs of (b) 10, (c) 20, (d) 40, (e) 60, (f) 100.

While the low-pass filter is a simple and commonly used choice, we could have chosen from numerous other filters. The differences that arise from filtering with the square versus circular filters introduced in section 6.1.2 are presented in Figure 6.6 which shows (a) the unfiltered data, and differences for cutoff values of (b) 10, (c) 20, (d) 40, (e) 60, (f) 100. The circular filter discards the Fourier components captured in the corners of the square filter. For small cutoff wavenumbers, this causes the differences to be larger because the number of Fourier components retained is already very limited.

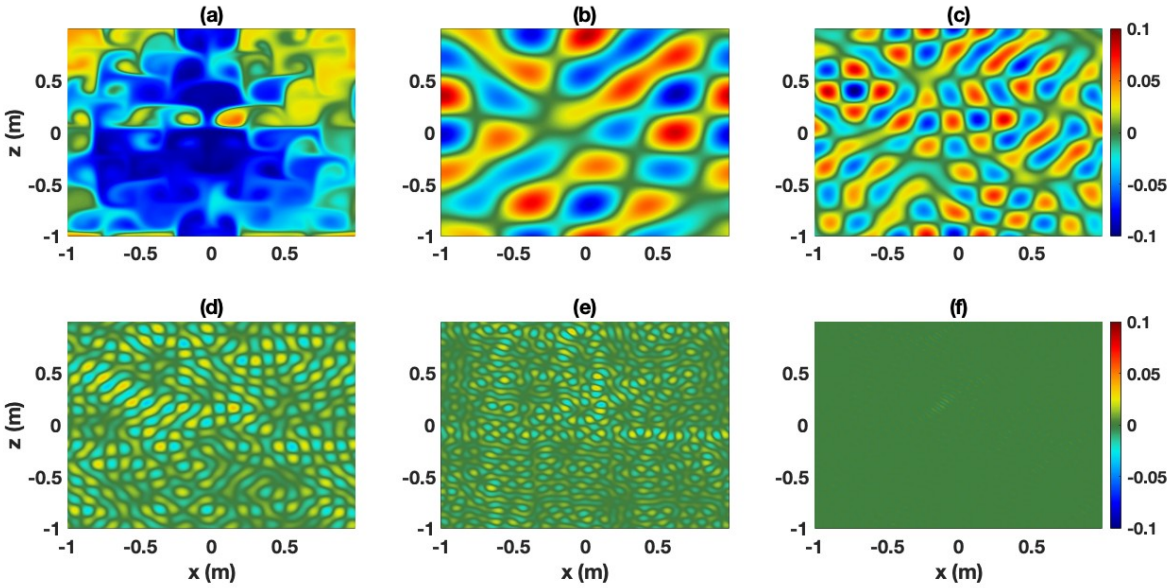


Figure 6.6: (a) Unfiltered reactive tracer concentration at $t = 0.3$ s. Differences between reactive tracer data filtered with the square and circular filters for cutoffs of (b) 10, (c) 20, (d) 40, (e) 60, (f) 100.

Effects of Varying the Damköhler Number

We now want to consider how changing the timescale of a reaction (thereby changing the Damköhler number) affects the filtered reactive tracer distribution and the **sfs** flux and reaction terms. Up to this point, we have had a passive tracer, $Da \to 0$, and a reactive tracer with $Da \sim O(1)$. Consider two additional simulations in which $Da \sim O(0.1)$ and $Da \sim O(10)$. We simply change α by an order of magnitude to scale Da. The extreme cutoff values of $k^{cut} = 10$ and $k^{cut} = 100$ shown in Figure 6.5 will be used to demonstrate the range of possible outcomes when low-pass filtering is applied.

In Chapter 5 we discussed the existence of positive feedback between turbulent mixing and tracer growth. Naturally, one might wonder how this is affected by the reaction rate since the simulations presented were constructed with the advective and reactive timescales on the same order of magnitude. The effect of the reaction rate on the **sfs** flux is important for understanding how LES might perform for various systems with reactions of different rates. In Figure 6.7, we show the norm of the time-averaged **sfs** fluxes as a function of the wavenumber cutoff. The magnitudes of the **sfs** fluxes increase with the reaction rate,

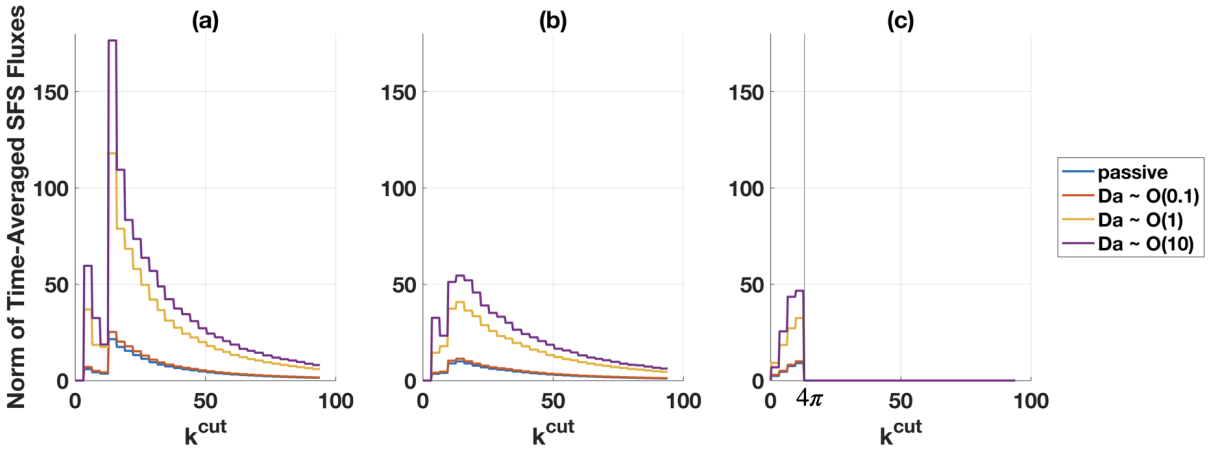


Figure 6.7: Sum of the norm of the time-averaged components of the **sfs** fluxes, $\vec{f}^A$, on the (a) resolved-scale, (b) cross-scale, and (c) sub-filter-scale. The vertical line in panel (c) at a wavenumber of 4π indicates the point at which the sub-filter-scale fluxes go to zero.

though it is not a linear relationship. The resolved-scale component of $\vec{f}^A$ (defined in equation 2.72) is largest for all values of k^{cut}, panel (a). For small values of k^{cut}, the cross-scale contributions to $\vec{f}^A$, panel (b), are smaller than those on the resolved-scale. However, as the wavenumber cutoff is increased, the contributions become similar in magnitude. For a cutoff greater than 4π the sub-filter-scale components, panel (c), drop off to zero because $\vec{u}' \to 0$. In the absence of turbulence, the velocity field limits the contributions of the sub-filter-scale components.

The non-linearity of Fisher's equation makes $\theta' \neq 0$ despite there not being any turbulence in the system. In Figure 6.8, we consider the norm of the time-averaged **sfs** reactions versus cutoff wavenumber for (a) $Da \sim O(0.1)$, (b) $Da \sim O(1)$, and (c) $Da \sim O(10)$. The **sfs** components are most significant for small values of k^{cut}. The vertical dotted lines indicate cutoff values for which the **sfs** component becomes less significant than the resolved-scale (first line) and cross-scale (second line, second row of panels) components. As expected, the magnitudes of the components scale with the reaction rate, though not linearly. Fast reactions reach a spatially uniform equilibrium state more quickly. Since the quantities in Figure 6.8 are averages over time, in the $Da \sim O(10)$ case, the contribution of the **sfs** component becomes smaller than those of the resolved or cross-scale components for a smaller value of k^{cut}.

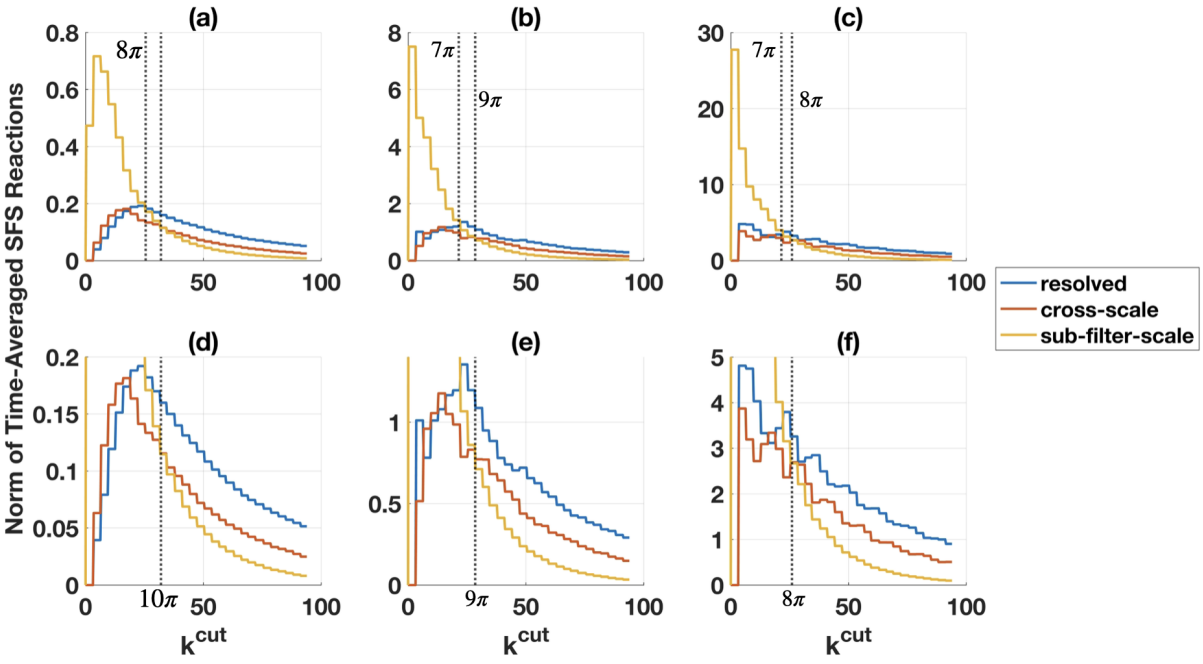


Figure 6.8: Norm of the time-averaged components of the **sfs** reactions, f^R, for (a) $Da \sim O(0.1)$, (b) $Da \sim O(1)$, and (c) $Da \sim O(10)$. The first vertical black line indicates the wavenumber for which the sum of the resolved components becomes equal to that of the sub-filter-scale components. The second line shows the same for the cross-scale components. The second row of panels provides a close up of the same data for the cases (d) $Da \sim O(0.1)$, (e) $Da \sim O(1)$, and (f) $Da \sim O(10)$.

In Figure 6.9, the norms of the components of the **sfs** reactions with $k^{cut} = 10$ (first row) and $k^{cut} = 100$ (second row) are integrated and shown as a function of time. The **sfs** reactions capture the time-dependent fluctuations in the higher frequency components of the prescribed velocities if k^{cut} is greater than 4π. The **sfs** reaction terms are largest when the smallest features in the velocity fields induce the most mixing. When $Da \sim O(1)$, advection and the reaction are tightly coupled. The tracer is spread into the finest flow structures via advection and diffusion and then growth enhances the development of sharp fronts. Thus, the magnitude of the **sfs** reaction term is sustained over the duration of the simulation. For $Da \sim O(10)$, $f^R \to 0$ because the system approaches a spatially uniform equilibrium state. In the $Da \sim O(0.1)$ case, mixing dominates, spreading the tracer through the domain. Compared to the $Da \sim O(1)$ case, fewer sharp fronts are formed. The **sfs** reaction term thus tends towards zero due to the lack of sharp, fine structures in the tracer distribution.

In Figure 6.10, the norms of the **sfs** flux components are integrated over the domain and shown as a function of time. Note that here we consider the vertical component of flux, but the horizontal component shows the same behavior. When $k^{cut} = 10$ the time dependent oscillations in the velocity field are captured by the **sfs** and cross-scale components. When k^{cut} is increased to 100 the oscillations are captured by the resolved and cross-scale components. The distribution between the components of the **sfs** flux is highly dependent on k^{cut}, but interestingly, the qualitative behavior exhibited by the total **sfs** flux seems relatively unaffected.

Integrating the **sfs** reaction and **sfs** flux quantities without taking their norms (thus allowing for cancellations) yields the results shown in Figures 6.11 and 6.12. For all values of k^{cut}, the resolved and cross-scale components of both the **sfs** reaction and flux terms are negligible. This indicates that while the terms are non-zero, local balances result in cancellations. The **sfs** component of the **sfs** reaction term is non-negligible for both $k^{cut} = 10$ and $k^{cut} = 100$, though its magnitude decreases with the increased wavenumber cutoff. The **sfs** component of the **sfs** flux term is non-negligible for $k^{cut} = 10$, but is on the order of machine precision for $k^{cut} = 100$. This is due to the fact that $\vec{u}' = 0$ for $k^{cut} = 100$.

6.1.4 Toy Model Takeaways

The toy model has proven to be an effective tool for investigating spatial filtering. The cutoff wavenumber used in a low-pass filter determines the degree to which a filtered distribution appears smeared compared to the unfiltered distribution. Using too harsh of a wavenumber cutoff results in a loss of detail. The cutoff value also determines the relative

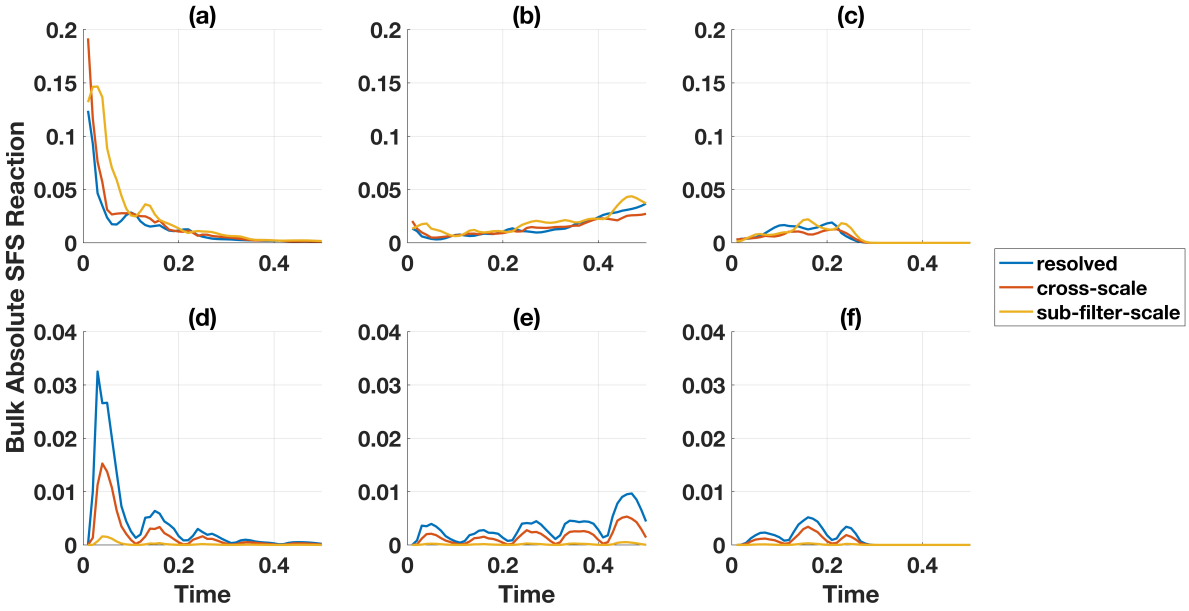


Figure 6.9: The norms of the components of the **sfs** reaction term integrated over the domain and scaled by Da. The first row has $k^{cut} = 10$ and the second has $k^{cut} = 100$. The columns, from left to right, correspond to the simulations with $Da \sim O(0.1)$, $Da \sim O(1)$, and $Da \sim O(10)$.

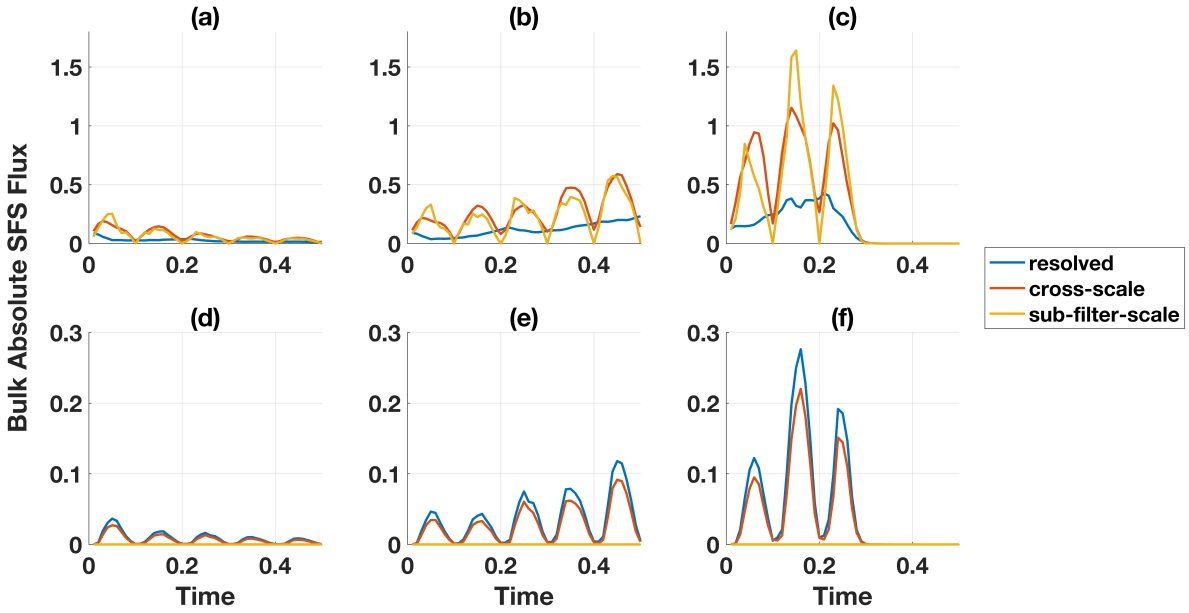


Figure 6.10: The norms of the components of the vertical **sfs** flux integrated over the domain. The first row has $k^{cut} = 10$ and the second has $k^{cut} = 100$. The columns, from left to right, correspond to the simulations with $Da \sim O(0.1)$, $Da \sim O(1)$, and $Da \sim O(10)$.

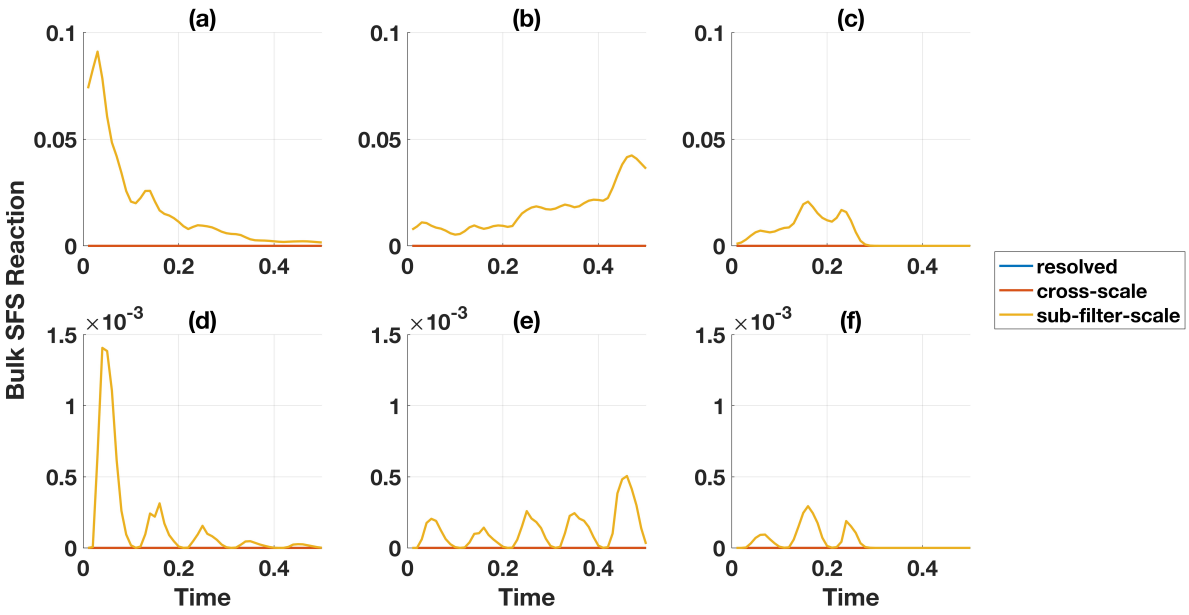


Figure 6.11: The components of the **sfs** reaction term integrated over the domain and scaled by Da. The first row has $k^{cut} = 10$ and the second has $k^{cut} = 100$. The columns, from left to right, correspond to the simulations with $Da \sim O(0.1)$, $Da \sim O(1)$, and $Da \sim O(10)$. Note that only the yellow curves are observable since the blue and red curves have tiny values.

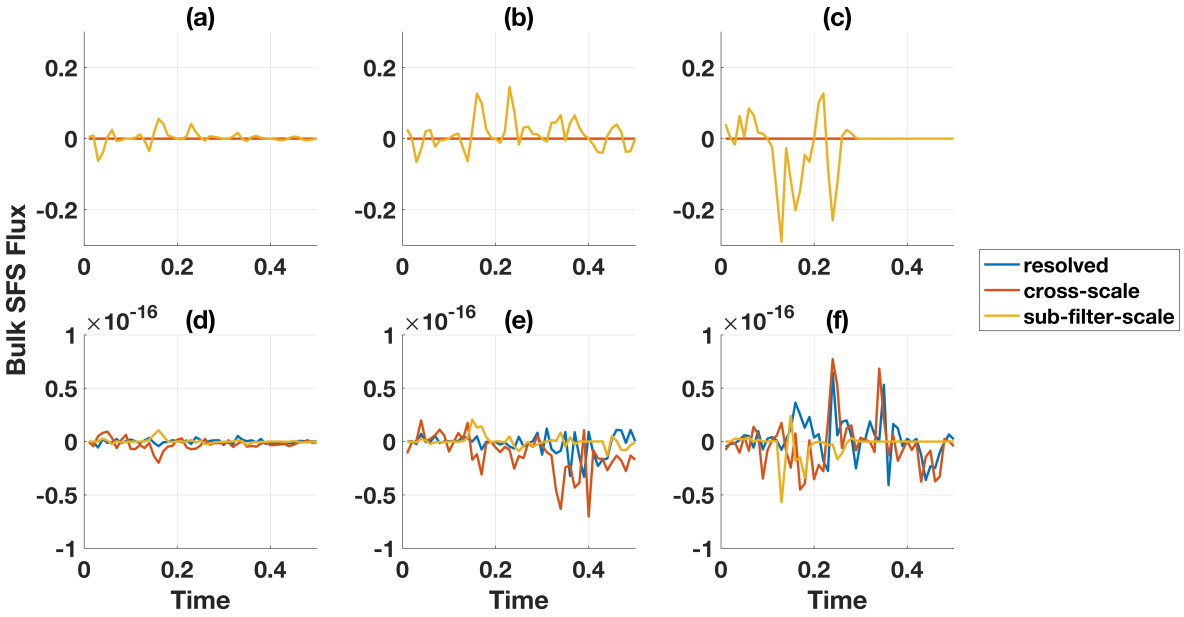


Figure 6.12: The components of the vertical **sfs** flux integrated over the domain.The first row has $k^{cut} = 10$ and the second has $k^{cut} = 100$. The columns, from left to right, correspond to the simulations with $Da \sim O(0.1)$, $Da \sim O(1)$, and $Da \sim O(10)$. Note that the values in the second row are on the order of machine precision.

importance of the resolved, cross-scale and **sfs** components of the **sfs** flux and reaction terms. The time-dependence of the small-scale component of the velocity field is reflected by the vertical **sfs** flux and, if the cutoff is sufficiently large, by the **sfs** reaction term. Cancellations in the resolved and cross-scale components cause the **sfs** component of the **sfs** reaction term to dominate. For the **sfs** flux term, this is only the case for relatively small cutoff values.

6.2 *A Posteriori* LES on 3D Rayleigh-Taylor Simulations

The two-dimensional toy model allowed us to understand the effect of spatial filtering and to begin investigating the **sfs** flux and reaction terms. Prescribing a multi-scale velocity field was helpful for analyzing the **sfs** quantities, but ultimately limiting because $\vec{u}'$ went to zero for small values of k^{cut}. In Chapter 5, we spent a significant amount of time understanding the evolution of a reactive tracer within a RT flow. Two-dimensional simulations are limited in their representation of turbulence because vortex tilting and stretching cannot be accounted for. In this section, we wish to consider a truly turbulent flow, so we extend the two-dimensional RT setup to three dimensions and then perform *a priori* LES analysis on the data.

6.2.1 3D Rayleigh-Taylor Simulation Setup

A three-dimensional RT simulation was run with a 1536 x 1536 x 384 grid and domain size 1.024m x 1.024m x 0.512m. The resolution in the horizontal is 6.67×10^{-4}m and that in the vertical is 1.3×10^{-3}m. Rayleigh-Taylor mixing was chosen as a real, well-studied example of a flow that induces primarily vertical mixing. The system starts from $\vec{u}(\vec{x}, t = 0) = 0$. A heavy layer of fluid overlies a lighter layer ($\Delta\rho = 1 \times 10^{-3}$) with the interface centered at $z = 0.256$m. The mean excess density profile with respect to the vertical is shown in panel (b) of Fig 6.13. To destabilize the stratification, the interface is perturbed symmetrically in both the x and y directions.

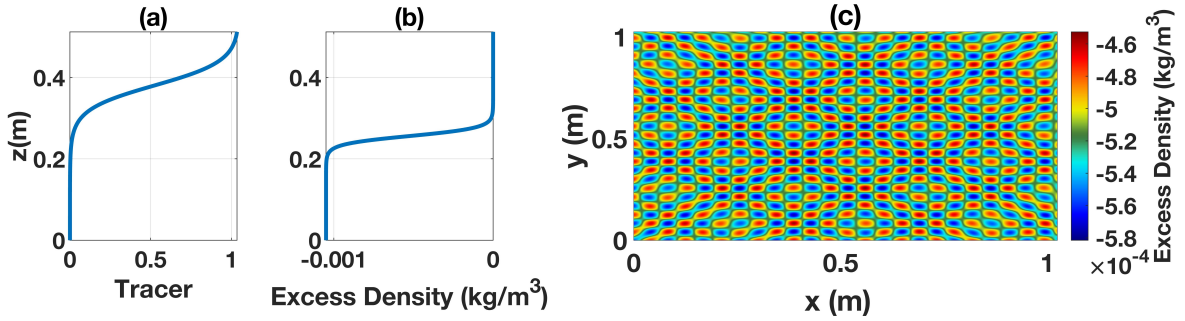


Figure 6.13: (a) The initial reactive and passive tracer profiles with respect to the vertical. (b) The mean initial excess density profile with respect to the vertical. (c) The excess density at $z = 0.256$ m.

$$\rho_E(\vec{x}, t = 0) = -5 \times 10^{-4} \left(1 - \tanh\left(\frac{z - 0.256 - \varepsilon(\vec{x})}{0.02}\right)\right), \tag{6.6}$$

$$\varepsilon(\vec{x}) = 2.5 \times 10^{-3} \sum_{i=1}^{3} Y_{1i} \sin\left(\frac{16\pi(Y_{2i} + 1)}{L_x} x + 2\pi Y_{3i}\right) \cdot \sin\left(\frac{16\pi(Y_{2i} + 1)}{L_y} y + 2\pi Y_{3i}\right), \tag{6.7}$$

where $Y_{ji} \sim U(0, 1)$ is a random variable chosen from a uniform distribution between 0 and 1 and $L_x = L_y = 1.024$m. An x-y slice showing the pattern the perturbations form is shown as panel (c) of Fig 6.13.

The initial tracer distribution is given by

$$\theta(\vec{x}, t = 0) = 0.5 \left(1 + \tanh\left(\frac{z - 0.38}{0.06}\right)\right) \tag{6.8}$$

and is shown in panel (a) of Fig 6.13. The reaction function is modified with a hyperbolic tangent as in Equation 5.4 with $\alpha = 0.1\text{s}^{-1}$.

Table 6.2 provides an overview of the parameters and dimensionless numbers relevant to the three-dimensional simulation. We take the Damköhler number, which is the ratio of reactive to advective timescales, to be $Da = \alpha L/U$. Using the root-mean-square vertical velocity at $t = 22$s (the latest output time we consider in the Results section) as the velocity scale and L_z as our characteristic length scale, then $Da \approx 5.95 \sim O(1)$.

Parameter	Value	Dimensionless Number	Value
L_x x L_y x L_z	1.024m x 1.024m x 0.512m	Re	4.5834×10^3
N_x x N_y x N_z	1536 x 1526 x 384	Sc	1
ν	1×10^{-6} m^2/s	Pe	4.5834×10^3
ρ_0	1000 kg/m^3	Da	5.9535
$\Delta\rho$	1×10^{-3} kg/m^3		
g	9.81 m/s^2		
κ	1×10^{-6} m^2/s		
α	0.1 /s		

Table 6.2: Parameters and Dimensionless numbers corresponding to the 3D simulation.

A priori LES is performed on the 3D simulations using the following filters:

$$\mathcal{G}_{\text{sharp}}(\vec{k}) = \begin{cases} 1, & k_i < k_i^{cut} \\ 0, & k_i \geq k_i^{cut} \end{cases} \tag{6.9}$$

$$\mathcal{G}_{\text{smoothed}}(\vec{k}) = \begin{cases} 1, & k_i < k_i^{cut} \\ \exp\left(-\alpha\left(\frac{|k_i|-k_i^{cut}}{1-k_1^{cut}}\right)^{\beta}\right), & k_i \geq k_i^{cut} \end{cases} \tag{6.10}$$

$$\mathcal{G}_{\text{wide smoothed}}(\vec{k}) = \begin{cases} 1, & k_i < k_i^{cut} \\ \exp\left(-\alpha\left(\frac{|k_i|-k_i^{cut}}{k_i^{nyq}-k_i^{cut}}\right)^{\beta}\right), & k_i \geq k_i^{cut} \end{cases} \tag{6.11}$$

$$\mathcal{G}_{\text{Gaussian}}(\vec{k}) = \exp\left(-2\left(\frac{|k_i|}{1-k_i^{cut}}\right)^2\right) \tag{6.12}$$

The value of k_i^{cut} corresponding to the $\mathcal{G}_{\text{sharp}}$ filter reduces the equivalent resolution of the filtered data by an order of magnitude ($k_i^{cut} \approx k_i^{nyq}/10$). The $\mathcal{G}_{\text{smoothed}}$ filter uses the same cutoff value and has parameter values $\alpha = 4.6052$, and $\beta = 2$. The $\mathcal{G}_{\text{Gaussian}}$ and $\mathcal{G}_{\text{wide smoothed}}$ filters use $k_i^{cut} = 0.5k_i^{nyq}$. This loosely corresponds to halving the equivalent resolution. In $\mathcal{G}_{\text{wide smoothed}}$, the parameter values are $\alpha = 20$, and $\beta = 2$. The filters are shown in Figure 6.14.

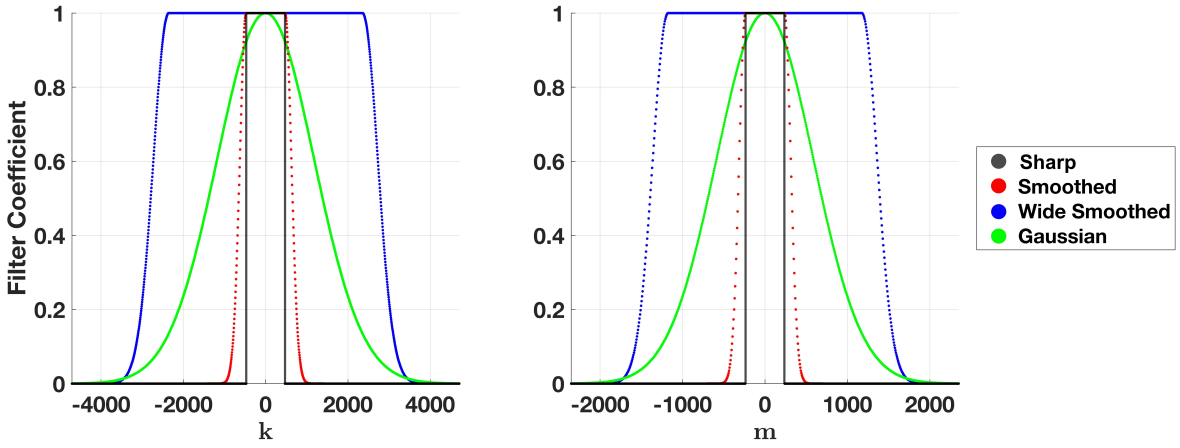


Figure 6.14: Filters used on the 3D data in the (a) k and l directions and (b) m direction. The smoothed and sharp filters retain all wavenumbers between the cutoff lines. The wide smoothed filter is the least harsh, as it retains a larger range of wavenumbers.

6.2.2 3D Filtering Results

Let us start by considering the evolution of the unfiltered reactive tracer distribution within the RT flow. Figure 6.15 shows $x-z$ (first row) and $x-y$ (second row) slices of the reactive tracer at three outputs. The $x-z$ panels are comparable to what was observed in the two-dimensional simulations. The reactive tracer concentration increases and it is entrained by structures that form due to the RT instability. For later times, panel (c), we observe more disordered turbulent structures as compared to the two-dimensional simulations due to the additional degrees of freedom in the system. Note that the $x-y$ panels retain some evidence of the perturbations applied to the density interface when the simulation was initialized, though this becomes less evident for later times.

We now take the reactive tracer distribution shown in panel (c) of Figure 6.15 and apply each of the four LES filters outlined in section 6.2.1. The normalized differences between the unfiltered data and the filtered data are shown in Figure 6.16. Filtering introduces oscillations because the Fourier series describing the data are truncated. In panel (a) of Figure 6.16, a sharp cutoff filter corresponding to an order of magnitude reduction in grid resolution has been applied. As a result, large oscillations are observed throughout the domain. When the low-pass filter is smoothed, a significant improvement can be observed, panel (b), in that the oscillations are distributed around the fine turbulent structures rather than throughout the entire domain. The Gaussian filter performs similarly to the

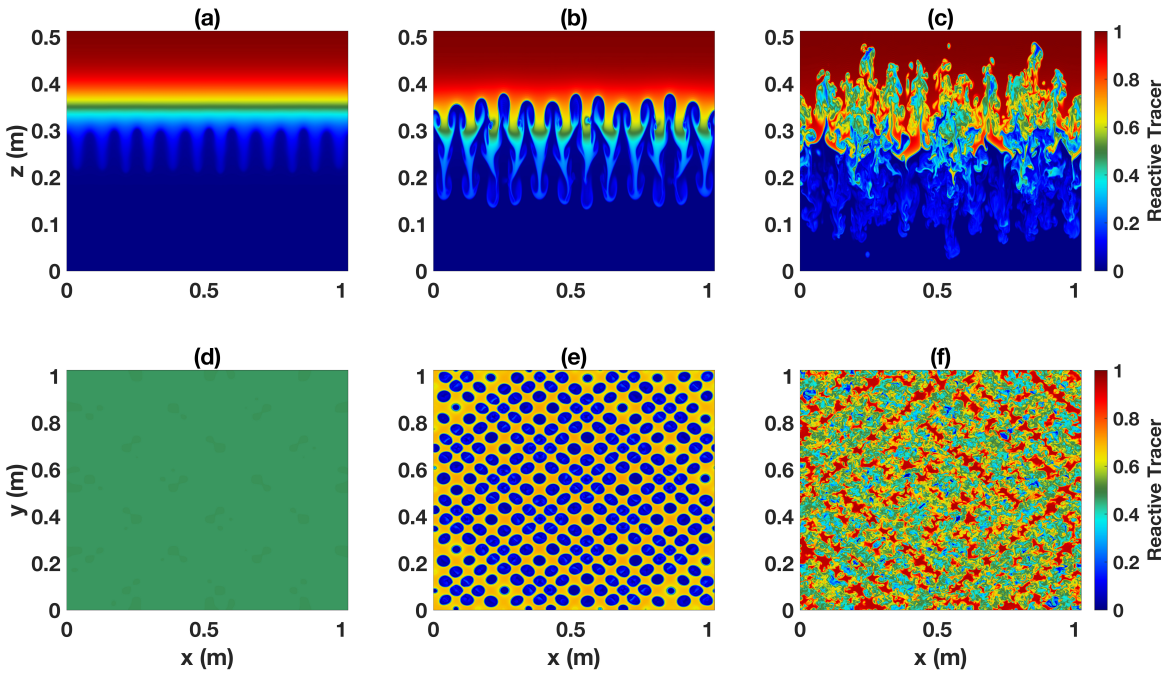


Figure 6.15: Evolution of the reactive tracer field. $x-z$ slices are taken at $y = 0.512$ m and at (a) $t = 10$ s, (b) $t = 16$ s, and (c) $t = 22$ s. $x-y$ slices are taken at $z = 0.3462$ m at the same times.

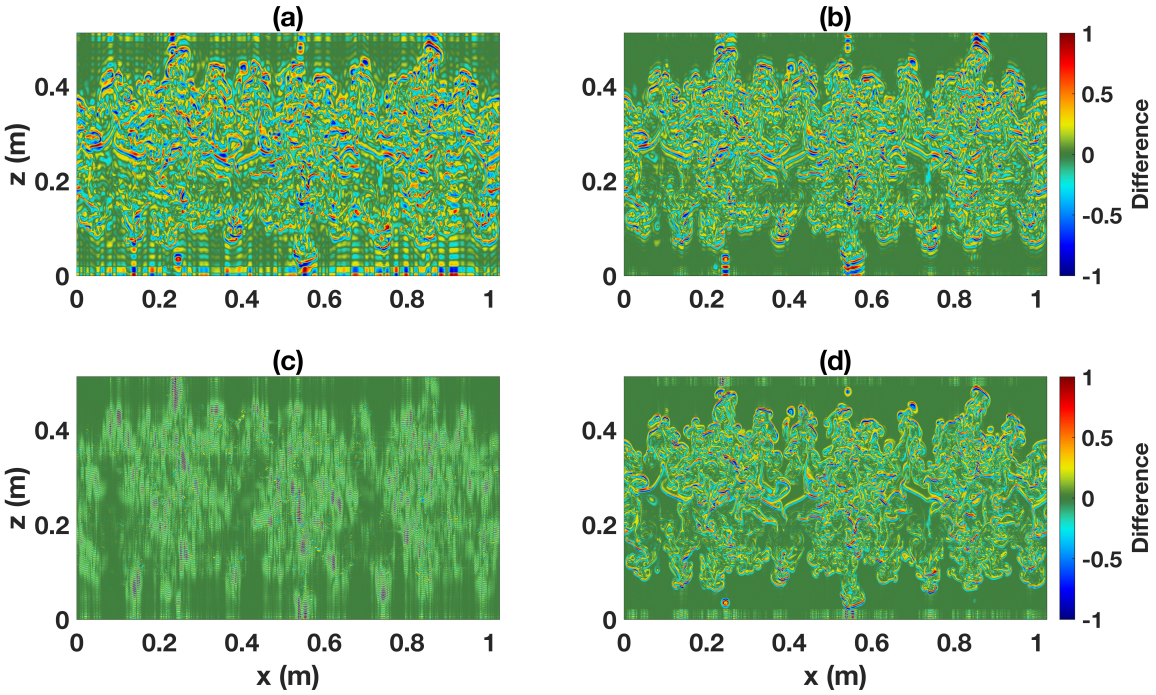


Figure 6.16: Normalized differences between the unfiltered reactive tracer field at $t = 22$ s and $y = 0.512$ m and data filtered with (a) the sharp filter, (b) the smoothed filter, (c) the wide smoothed filter, and (d) the Gaussian filter.

smoothed filter but, as expected, the wide smoothed filter (which retains the most Fourier components and corresponds to the smallest decrease in resolution) results in the fewest large scale oscillations.

In Chapter 5, we noted that both the *a priori* RANS analysis and the pseudo-RANS solution underestimated the rate at which the reactive tracer spread deeper into the domain. Under *a priori* LES, we expect the filtered data to capture the rate at which the reactive tracer spreads fairly well. This can be quantified by considering the vertical profiles of the unfiltered and filtered reactive tracer distributions. In panels (a), (d), (g) of Figure 6.17 we show the reactive tracer profile with respect to the vertical for each of the times shown in Figure 6.15. The profile is calculated by integrating in the x and y directions. The second column of Figure 6.17 shows the profile of the differences between the filtered and unfiltered data. The third column shows the profile of the norm of the differences. Once again, using the wide smoothed filter is most advantageous, with the Gaussian filter being the next best choice since these result in the smallest amplitude oscillations and the smallest

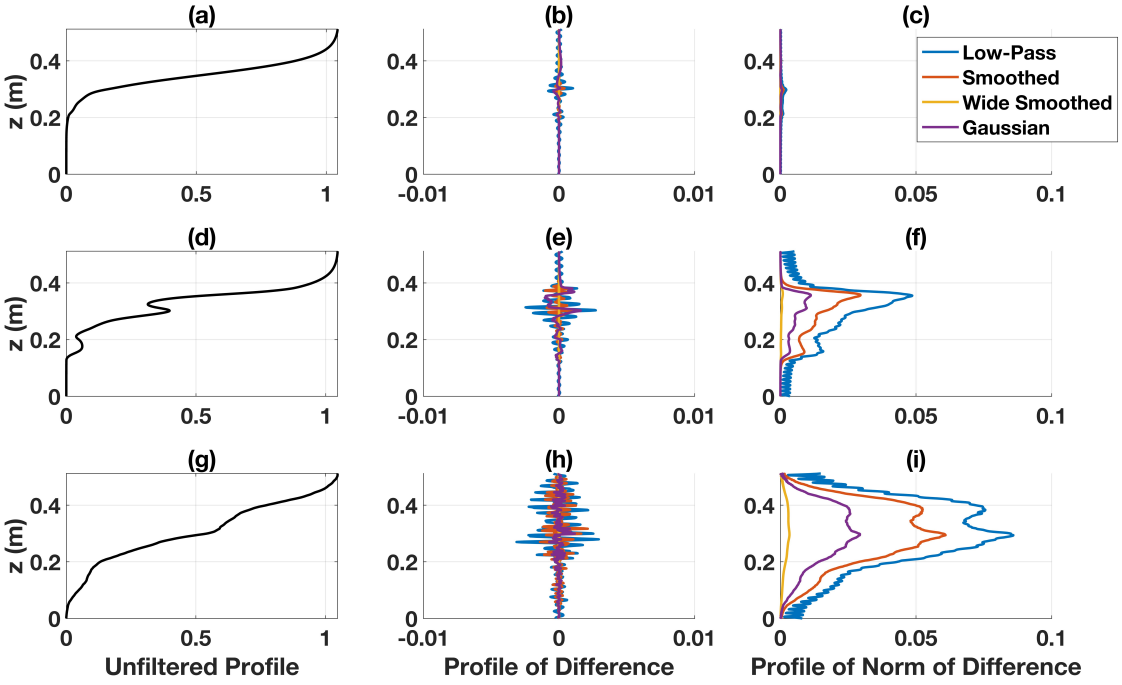


Figure 6.17: Unfiltered reactive tracer norm integrated in x and y at (a) $t = 10$ s, (d) $t = 16$s, and (g) $t = 22$ s. The second column shows the differences between the profiles of the unfiltered data and data filtered with the various filter choices at the corresponding times. The third column shows the profiles of the norm of the differences between the unfiltered data and filtered data.

differences. For coarser filters, the differences are largest in areas where the tracer is most affected by turbulent mixing. Harsh filters result in larger oscillations and thus choppy tracer profiles. For models that implement filters as part of their numerical method, for example as a de-aliasing strategy, it is ideal to choose the least harsh filter allowable.

Taking the reactive tracer data at $t = 22$ s, we can investigate how each of the four filters we have been considering affects the **sfs** reaction term. The vertical profiles of the components are shown in Figure 6.18. When the sharp cutoff filter is used, panel (a), the **sfs** component of the **sfs** reaction term is dominant. The resolved and cross-scale profiles oscillate around zero, suggesting that local balances result in cancellations. When the filter is smoothed, panel (b), the cross-scale component begins to contribute more. In the cases of the wide smoothed, panel (c), and Gaussian, panel (d), filters the cross-scale component dominates. Note that the **sfs** term produced by the wide smoothed filter is two orders of

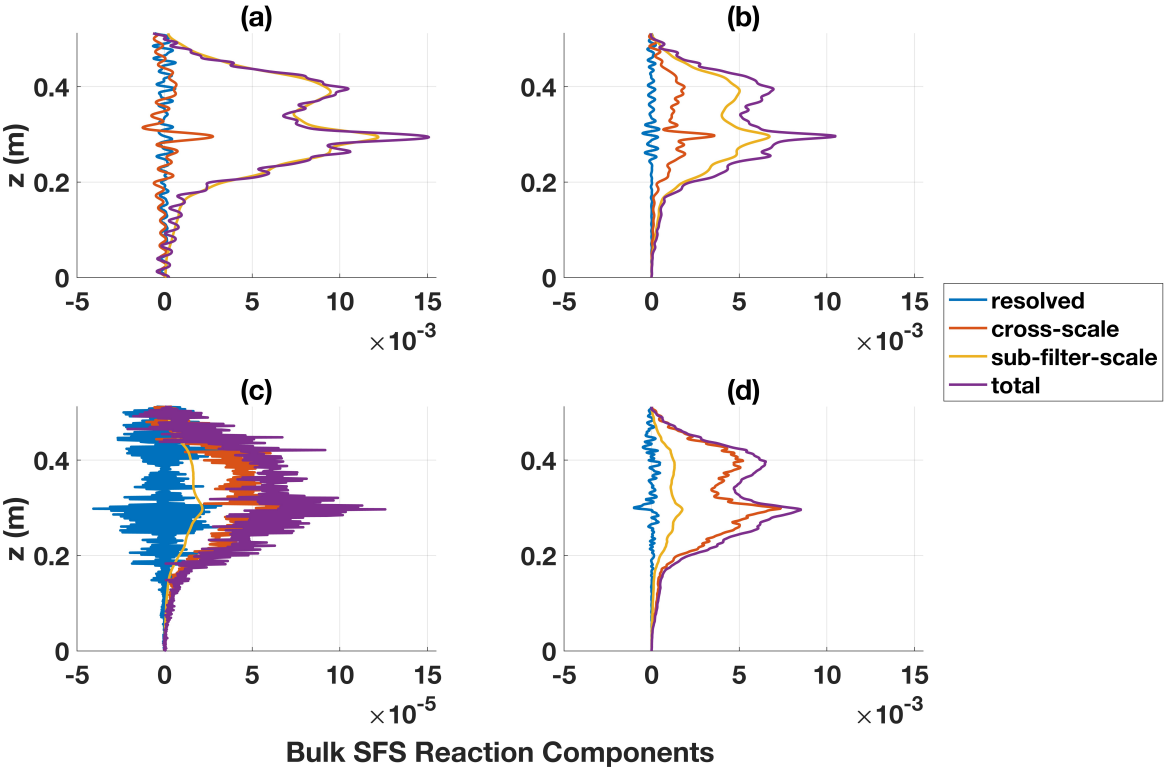


Figure 6.18: The **sfs** reaction components at $t = 22$ s integrated with respect to x and y for the data filtered with the (a) sharp filter, (b) smoothed filter, (c) wide smoothed filter, and (d) Gaussian filter.

magnitude smaller than those produced by the other filters. For the modeller limited to a coarse resolution simulation, the local balances in the resolved and cross-scale components of the **sfs** reaction term are good news. Parameterization efforts can be concentrated on the **sfs** component. It is likely also the easiest term to parameterize, considering $(\theta')^2$ is positive semi-definite.

It is, of course, advantageous to retain as much information as possible when filtering. However, LES is generally used when the resolution of a simulation is limited. The unfiltered data we are working with has millimeter scale resolution. Applying the sharp cutoff filter brings this to centimeter scale resolution. In any physical context, this is still extremely well resolved (though usually such contexts involve much larger domains). For instance, large eddy simulations of submesoscale ocean dynamics are considered to be

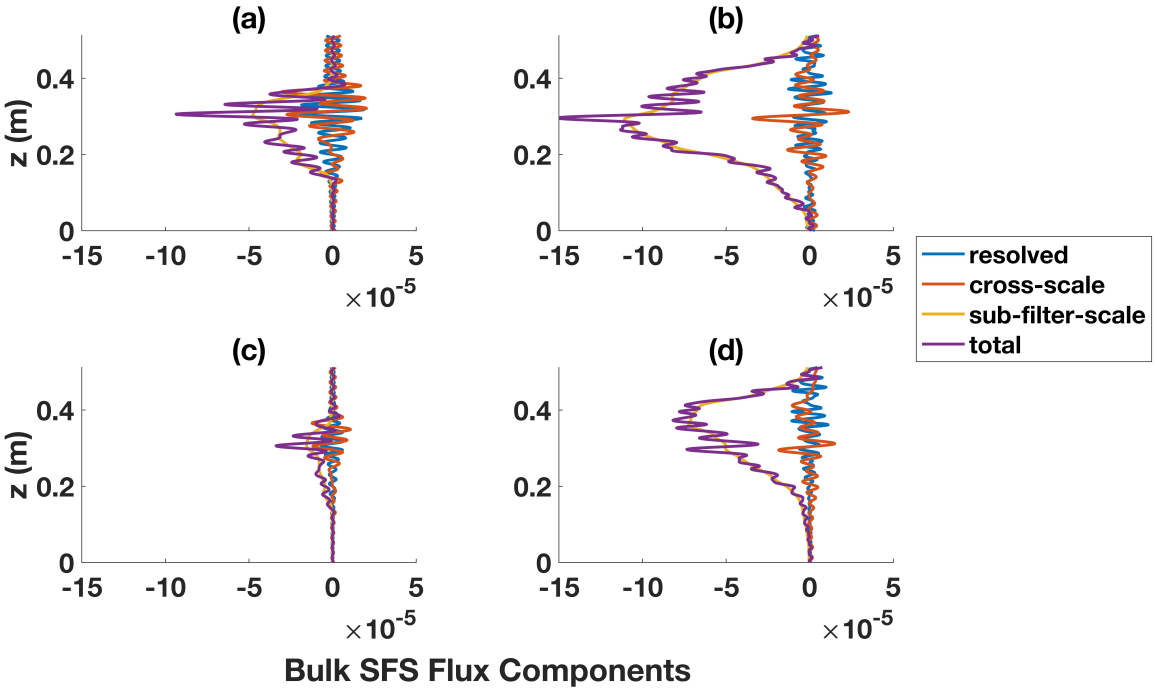


Figure 6.19: Profiles of the components of the vertical **sfs** flux term under the sharp filter. Panels (a) and (c) show the reactive and passive tracers, respectively, at $t = 16$ s. The second column corresponds to $t = 22$ s.

highly resolved with resolutions of 0.5 to 2 meters[91, 107] even though three-dimensional turbulence is known to extend to much smaller scales. Therefore, for the remainder of this chapter, we will use only the sharp cutoff filter to consider the effect of decreasing the LES resolution by an order of magnitude.

Turning to the vertical **sfs** flux term that results from applying the sharp cutoff filter, we once again find that the **sfs** component dominates. In Figure 6.19, the components of the vertical **sfs** flux term are plotted for the reactive (first row) and passive (second row) tracers at $t = 16$ s (first column) and $t = 22$ s (second column). As the flow becomes more turbulent, the total **sfs** flux increases, as does the contribution of the **sfs** component. The contributions of the resolved and cross scale components remain largely unchanged, though the magnitude of the cross-scale component does increase around the mid-depth.

If we compare the spatial distributions of the components of the **sfs** reaction and flux terms produced with the sharp cutoff filter, Figure 6.20, to the reactive tracer distribution

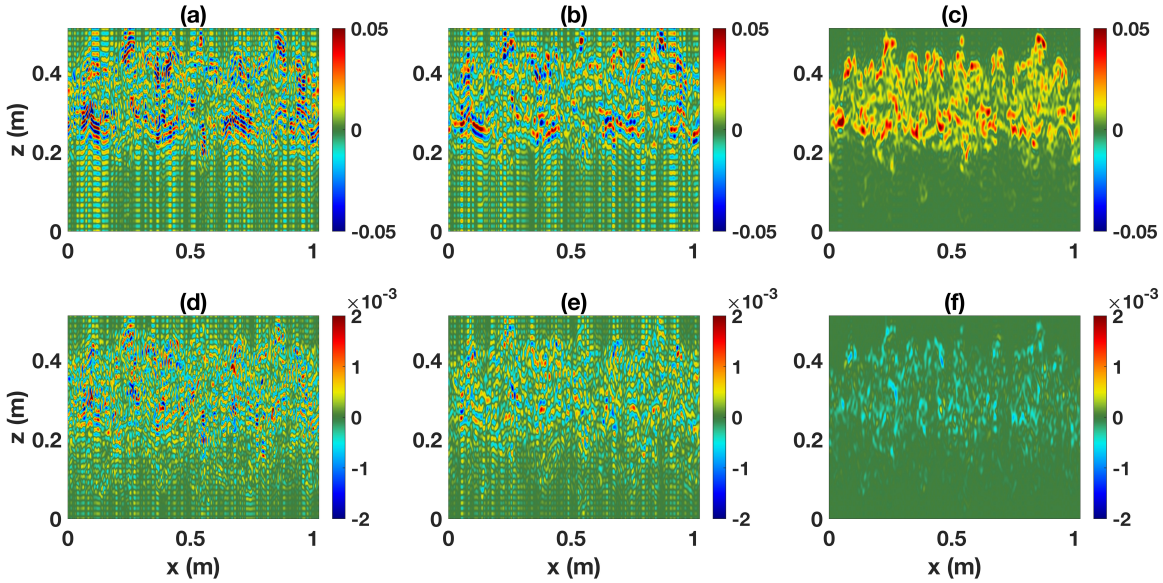


Figure 6.20: (a, d) Resolved-scale, (b, e) cross-scale, and (c,f) **sfs** components of the **sfs** reaction term (first row) and the vertical **sfs** flux term (second row) at $y = 0.512$ m and $t = 22$ s. The **sfs** terms are obtained using the sharp cutoff filter. Both the **sfs** flux and reaction terms have a negative coefficient in the filtered equations that is not being accounted for in this figure.

in panel (c) of Figure 6.15, we see that the magnitudes of the components are largest around the edges of the turbulent structures that have managed to entrain the tracer. The resolved and cross scale components for both the **sfs** reaction and flux terms have a highly oscillatory spatial distributions. Local balances thus play a large role in reducing their contributions to the overall **sfs** reaction and flux terms. The **sfs** component of the **sfs** reaction term, panel (c) of Figure 6.20 is mostly non-negative and its magnitude is largest within the bubbles and spikes of the RT plumes. Recall from equation 2.63 that the non-negativity of the **sfs** component actually implies that it acts primarily as a sink in the filtered ADR equation. Since applying the sharp cutoff filter to the reactive tracer field results in a smearing of the tracer distribution, we can interpret the effect of the **sfs** component of the **sfs** reaction term as maintaining the sharpness of the tracer fronts by decreasing the amount of tracer outside the material volumes that are present in the unfiltered dataset. The effect of the **sfs** component of the **sfs** flux term is less clear, but it seems to mostly push the reactive tracer up-gradient out of the RT plumes.

6.3 Conclusions

Spatial filtering applied in spectral space either truncates the Fourier series representation of the data or limits the amplitudes of the terms in the Fourier series (or some combination of both). The harshness of a filter is the result of its wavenumber cutoff and whether it is a sharp cutoff filter or smoothed. Harsh filters retain only the features with the lowest wavenumbers making distributions look smeared. For a sharp-cutoff filter, differences between the unfiltered and filtered data are contained in the truncated portion of the Fourier series. In general, the differences between unfiltered and filtered data will take the form of oscillations around the fine features visible in the physical distribution.

From the two-dimensional toy model we were able to investigate the impact of the reaction rate on the **sfs** quantities. The Damköhler number determines the rate at which the reactive tracer approaches a spatially uniform equilibrium state. The absorption of fine spatial features into the uniform tracer distribution corresponds to the effective shortening of the Fourier series representation of the data. In Chapter 4 we saw that the non-linearity in the reaction term activates higher wavenumbers. If a reaction is fast enough (or a simulation long enough) for the reactive tracer distribution to reach a spatially homogeneous equilibrium state, then the reaction can also have the opposite effect.

We found that the magnitudes of the **sfs** flux and **sfs** reaction terms scale with the Damköhler number, though not linearly. Both terms captured the time-dependence of the small-scale features in the analytically specified velocities. There are local balances in the resolved and cross-scale components of both the **sfs** flux and **sfs** reaction terms. Therefore, the **sfs** components are most important to consider when conceptualizing parameterizations.

Unfortunately, the intuition that can be derived from the two-dimensional toy simulation is limited by the fact that the **sfs** components of the velocities go to zero for small values of k^{cut} and thus so do the **sfs** flux terms. Constructing a more complex toy model with an increased number of advective scales may be a worthwhile avenue for future work if it can be used to investigate interactions between scales. The three-dimensional Rayleigh-Taylor simulation provides a better sample dataset, as it captures a greater range of scales. By applying four different spectral filters, we showed that it is advantageous to use the largest value of k^{cut} possible and, when possible, construct the filter so that it is smoothed past k^{cut}.

We found evidence of local balances in the **sfs** reaction and **sfs** flux terms calculated from the three-dimensional data. However, the balances are dependent on the filter being applied. The resolved scale component of the **sfs** reaction term fluctuates around zero

regardless of the filter, but the cross-scale component dominates over the **sfs** component when the wide smoothed or Gaussian filters are used. Both the resolved and cross-scale components of the **sfs** flux and reaction terms fluctuate around zero when the sharp cutoff filter is applied. The fluctuations are largest near the mid-depth where there is the most turbulent mixing and are larger for reactive tracers. The **sfs** components of the **sfs** reaction and flux terms are distributed around the fine turbulent structures in the flow.

6.4 Discussion

The modeller wanting to parameterize the **sfs** flux and reaction terms should find some comfort in the local balances found herein. The spatial distributions of the **sfs** components indicate that the effects of the unresolved terms are localized to (relatively) more turbulent areas. One strategy for parameterizing the **sfs** reaction could be to identify areas of strong mixing and slow the reaction rate locally. Similarly, the vertical **sfs** flux is likely to amplify the up-gradient transport of the reactive tracer in regions where there is significant mixing and sharp reactive tracer fronts.

The sharpness of the fronts created by the reaction indicates the degree to which the **sfs** terms contribute to the reactive tracer distribution. It is also a function of the relative reactive and diffusive timescales. When running a low resolution pseudo-spectral simulation, not being able to resolve sharp fronts results in ringing. It is common to use an eddy viscosity or diffusivity parameterization in a LES to smooth the distributions and avoid any artifacts from the numerical method. As shown in Chapter 4, diffusion is effectively a Gaussian filter. Recall that the magnitude of the diffusivity dictates the width of the Gaussian with larger diffusivities imposing harsher filters and that eddy diffusivity parameterizations assume the effect of the **sfs** fluxes is to transport the tracer down its resolved gradient when we have indeed found the opposite to be true.

As shown in Chapter 4, a low-pass filter can be defined with a cutoff wavenumber equivalent to the Nyquist frequency of a particular grid resolution. Therefore, filtering can be used to draw comparisons between a high-resolution DNS and a lower-resolution LES. In Section 4.2.2, we discussed how the multiplication of high wavenumber contributions that are out of phase can result in resolvable contributions. In *a priori* LES, these contributions are accounted for. However, in a true LES, the sub-grid-scale features may be aliased onto lower wavenumbers (subject to the de-aliasing strategy or numerical dissipation of the model). Assuming the aliasing is adequately dealt with, running high resolution DNS of events of features identified in a lower-resolution LES may allow for the development

of process specific parameterizations. This is certainly an improvement over parameterizations that use a constant eddy viscosity or diffusivity. While computationally more demanding than the Germano dynamic model[35], this method also avoids the assumption that the form of three-dimensional turbulence is similar on all scales.

Chapter 7

Overall Conclusions

7.1 Summary

Biogeochemical processes are ubiquitous within natural fluid environments such as the oceans or the atmosphere. Such processes can generally be described by multi-component systems wherein the components may react with themselves (growth or autocatalytic reactions), interact with one another, and react to their environment. The classic nutrient-phytoplankton-zooplankton system is a well-studied example [98, 71, 93, 78].

Within fluid environments, motions occur over a large range of length scales. Turbulence dominates the smallest scales and resolving turbulent motions has long posed a computational challenge. In response, turbulence models have been developed in an effort to capture the most essential characteristics of a turbulent flow. These models allow coupled fluid dynamical and biogeochemical systems to be simulated, but are inevitably inaccurate to some degree due to their very nature.

This thesis characterizes the description of a model reactive, passive tracer under two classes of turbulence models: Reynolds Averaged Navier Stokes simulations (RANS) and large eddy simulations (LES). The tracer is taken to be passive with respect to the fluid dynamics and undergoes a growth reaction governed by Fisher's equation. Throughout this thesis, the reactive tracer will be compared to a non-reactive, passive tracer. To begin, the Navier-Stokes equations and the partial differential equation governing the reactive tracer evolution are Reynolds averaged and spatially filtered to obtain the governing equations for each of the turbulence models. The procedure is applied to a generalized polynomial reaction function and can be extended to sufficiently smooth non-polynomial reactions.

For Fisher's equation, Reynolds averaging produces a sink in the governing equation, while the effect of spatial filtering is less clear.

Using zero and one dimensional toy models, intuition can be developed as to the effect of Reynolds averaging or spatial filtering on the evolution of the reactive tracer. It is shown that non-linear reaction functions result in the activation of higher wavenumbers. Diffusion has the opposite effect in that it effectively acts as a filter and constraints the spectral distribution of the reactive tracer. Under Reynolds averaging, a sink is introduced into the reaction function for the mean equations. In the 0D system, this results in the mean tracer value tending towards the stable equilibrium more slowly than an ensemble member. The terms introduced in the reaction function due to spatial filtering are harder to interpret, though it is possible to make some analytical progress by assuming the reactive tracer only has two active wavenumbers. Keeping the analytical results in mind, we turn to two and three-dimensional direct numerical simulations of the model reactive tracer.

To consider the effect of Reynolds averaging, an ensemble of 50 two-dimensional direct numerical simulations is run. Within each simulation, the reactive tracer is subjected to mixing induced by a Rayleigh-Taylor instability. Using the ensemble data and applying Reynolds averaging, it is shown that the mean provides a poor description of the dynamics of the ensemble members and that the fluctuations capture the downwards propagation of the tracer. Further, the magnitude of the scalar variance of the reactive tracer is found to be non-negligible when compared to that of the mean and so the sink introduced in the Reynolds averaged equations should not be ignored. The eddy diffusivity parameterization is evaluated and shown to provide a poor approximation of the eddy fluxes due to the presence of counter-gradient fluxes. To compliment the *a priori* analysis, the Reynolds averaged equation governing the evolution of the reactive tracer is solved. The mean velocities, eddy flux, and eddy reaction terms are calculated from the ensemble data. The solution to the Reynolds averaged system exhibits a lack of downward transport, likely due to cancellations in the mean vertical velocities of the ensemble members.

A two-dimensional toy model with specified velocities is used to illustrate the effect of spatial filtering. Harsh filters result in smeared distributions due to the removal of small-scale features. The dependence of the sub-filter-scale flux and reaction terms on the harshness of a low-pass filter and the reaction rate is evaluated using the toy model. The magnitudes of the sub-filter-scale terms scale with the reaction rate, though not linearly, and capture the time-dependence of the small-scale features in the prescribed velocities. To create a dataset with a larger range of spatial scales, a three-dimensional direct numerical simulation is run. For consistency, a reactive tracer is once again subjected to turbulence induced by a Rayleigh-Taylor instability. *A priori* LES is applied to the data with various filter choices. Local balances that depend on the filter applied were found in the sub-filter-

scale flux and reaction terms. The sub-filter-scale component of the unresolved flux and reaction terms is found to be the most significant and its spatial structure is dependent on the fine features present in the turbulent flow.

7.2 Discussion

The reactive timescale of our model reactive tracer is deliberately chosen to be similar to the advective timescales of the flows considered herein. In the oceans, there are numerous advective processes occurring simultaneously with varying spatial and temporal scales. To complicate matters further, there are numerous interconnected biogeochemical reactions occurring, each with a distinctive timescale. The description of a system with a reactive tracer thus often contains multiple timescales from reactive processes and environmental forcing. For example, the growth rate of phytoplankton may vary on a daily timescale due to light availability, on a seasonal cycle due to temperature changes, and may be perturbed by the injection of nutrients into the system. In the Southern Ocean, phytoplankton biomass variability exhibits subseasonal, seasonal, and multiannual components [57].

In any physical or biogeochemical system, there does not exist a clean separation of spatio-temporal scales. In the oceans, submesoscale ($O(200\text{m} - 20\text{km})$) dynamics transfer energy both down-scale from the mesoscale (where it is injected) to the scales of turbulence (where it is dissipated) and in the up-scale direction [90]. This means that fine-scale flows may impact biogeochemical processes on their own scales via eddy fluxes and on larger scales due to up-scale energy transfers [57]. The importance of fine-scale dynamics is strongly region dependent. In the tropics, low-frequency climate modes have been shown to account for most of the inter-annual phytoplankton variability, whereas correlations are weaker in higher latitudes [49]. In the Southern Ocean, the subseasonal component of phytoplankton biomass contributes the most to the inter-annual variability and does not correlate with the Southern Annual Mode, suggesting that small-scale intermittent forcing plays an important role [75].

Given this context, it suffices to say that the model reactive tracer considered in this thesis is highly idealized. The diversity of reactive tracers found in the oceans makes taking a "one size fits all" approach infeasible. Rather, herein several fundamental concepts and methods have been demonstrated that can aid in the development of parameterizations for reactive tracers within turbulent environments. Rayleigh-Taylor instabilities were deliberately chosen because of the importance of small-scale (submesoscale) vertical mixing for biological systems [57]. Considering the interactions of multiple advective scales is an avenue of future work that is actively being pursued.

For the reader looking to develop a model for a particular system containing a reactive tracer, there are several important takeaways in this thesis. First and foremost, the suitability of either RANS or LES depends highly on the tracer and model in question. For our model reactive tracer, the Reynolds averaged reaction has an unknown term depending on the scalar variance of the tracer. If there were to hypothetically exist sufficient observational data to quantify the scalar variance of the tracer, then developing a parameterization for RANS may be the best choice. Otherwise, we suggest using LES under the speculation that the resolved field will be more representative of a DNS than the Reynolds averaged field from a RANS simulation. This is a potential avenue for future work, as it remains to be concretely verified.

When the local balances in the resolved and cross-scale **sfs** flux and reaction terms are considered, the filtered reaction reduces to a sink that is dependent on the unresolved portion of the tracer distribution. While the filtered and Reynolds averaged reaction terms essentially reduce to the same mathematical form, the **sfs** reaction is more physically intuitive. The sub-grid-scale effects in a LES will be mostly localized to small-scale mixing events. In atmospheric LES, nesting is used to account for small-scale dynamics [69, 68, 41]. For incompressible systems, nesting is problematic due to the need to communicate pressure information across the entire domain instantaneously. For such systems, perhaps it would be more appropriate to identify the presence of small-scale mixing events, how they connect to one another, or what triggers them, though we recognize this is not a trivial task. Studying such events in detail through high resolution simulations would allow for the development of event-specific parameterizations, such as effective eddy viscosities, or at the very least an understanding of the significance of the event within a larger simulation. Taking this approach would allow for the description of intermediate mixing stages before a turbulent flow reaches statistical equilibrium. In regional models, mixing events are continuously perturbing the statistical equilibrium of a flow. In such contexts, it seems unlikely that the form of the three-dimensional turbulence is similar on all scales as is assumed by the Germano dynamic model [35].

As an example, internal waves are a nonhydrostatic phenomenon that most regional models cannot resolve. The shoaling dynamics of internal waves are significant and in the South China Sea have been documented to induce significant nutrient fluxes into the euphotic zone, thereby supporting biological activity [60, 45]. Describing the generation, propagation, and shoaling of internal waves is a multiscale problem. Environmental conditions such as bathymetry, wind conditions, stratification, and pre-existing turbulence among others affect the manifestation of an internal wave [102, 22, 115]. As an internal wave propagates through a region, it induces mixing and systematic transport, thereby perturbing the system. Some of these features are highlighted in Figure 7.1. The first panel

shows the generation of an internal wave due to flow over a sill. The second panel shows an internal wave of depression shoaling over undulating topography. As the wave shoals, instabilities are generated and eventually these breakdown into small-scale turbulence. A significant amount of observational, experimental, and numerical work has been focused on describing the mixing and transport induced by internal waves and their generation mechanisms (see [87] for a review). Further, several algorithms have been developed to detect and track internal waves [19]. Given the degree to which internal waves have been studied, it seems plausible that in a regional LES, they could be accounted for through a parameterization derived from observational data and tracking, and high-resolution numerical simulations. This is indeed a challenging task, but one that is well-worth attempting.

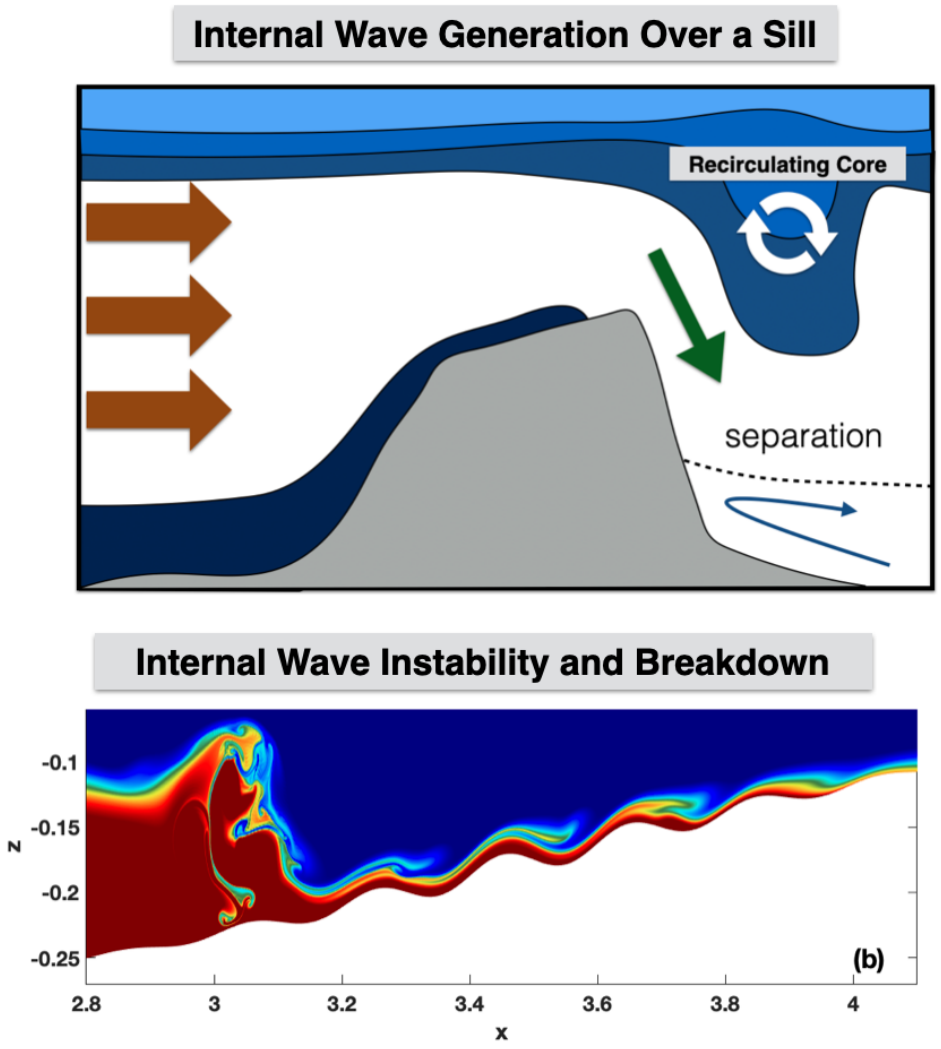


Figure 7.1: The first panel shows the generation of an internal wave over a sill. Within the wave, a recirculating core forms. Large enough topography induces separation. The second panel shows an internal wave of depression shoaling over undulating topography. As the wave shoals, instabilities are generated and breakdown into turbulence. The second panel is reproduced from [87] with permission.

References

[1] ROMS Wiki Vertical Mixing Parameterizations. https://www.myroms.org/wiki/Vertical_Mixing_Parameterizations. Accessed: 2023-08-18.

[2] Ryan Patrick Abernathey and J Marshall. Global surface eddy diffusivities derived from satellite altimetry. *Journal of Geophysical Research: Oceans*, 118(2):901–916, 2013.

[3] Edward R Abraham. The generation of plankton patchiness by turbulent stirring. *Nature*, 391(6667):577–580, 1998.

[4] Giancarlo Alfonsi. Reynolds-Averaged Navier–Stokes Equations for Turbulence Modeling. *Applied Mechanics Reviews*, 62(4):040802, 2009.

[5] Athanasios Angeloudis, Thorsten Stoesser, Carlo Gualtieri, Roger Falconer, et al. Effect of three-dimensional mixing conditions on water treatment reaction processes. In *Proceedings of the 36th IAHR World Congress. The Netherlands: The Hague*, 2015.

[6] Damien Aubagnac-Karkar, Jean-Baptiste Michel, Olivier Colin, Pauline E Vervisch-Kljakic, and Nasser Darabiha. Sectional soot model coupled to tabulated chemistry for diesel rans simulations. *Combustion and Flame*, 162(8):3081–3099, 2015.

[7] Scott D Bachman, Baylor Fox-Kemper, and Frank O Bryan. A tracer-based inversion method for diagnosing eddy-induced diffusivity and advection. *Ocean Modelling*, 86:1–14, 2015.

[8] Dhruv Balwada, K Shafer Smith, and Ryan Abernathey. Submesoscale vertical velocities enhance tracer subduction in an idealized antarctic circumpolar current. *Geophysical Research Letters*, 45(18):9790–9802, 2018.

[9] Roy Barkan, Kraig B Winters, and James C McWilliams. Stimulated imbalance and the enhancement of eddy kinetic energy dissipation by internal waves. *Journal of Physical Oceanography*, 47(1):181–198, 2017.

[10] Andrew D. Barton, Fernando González Taboada, Angus Atkinson, Claire E. Widdicombe, and Charles A. Stock. Integration of temporal environmental variation by the marine plankton community. *Marine Ecology Progress Series*, 647:1–16, August 2020.

[11] Melissa M Baustian, Ehab Meselhe, Hoonshin Jung, Kazi Sadid, Scott M Duke-Sylvester, Jenneke M Visser, Mead A Allison, Leland C Moss, Cyndhia Ramatchandirane, Dirk Sebastiaan van Maren, et al. Development of an integrated biophysical model to represent morphological and ecological processes in a changing deltaic and coastal ecosystem. *Environmental Modelling & Software*, 109:402–419, 2018.

[12] Simon Bélanger, Marcel Babin, and Jean-Éric Tremblay. Increasing cloudiness in arctic damps the increase in phytoplankton primary production due to sea ice receding. *Biogeosciences*, 10(6):4087–4101, 2013.

[13] Elisa Benincà, Vasilis Dakos, Egbert H. Van Nes, Jef Huisman, and Marten Scheffer. Resonance of Plankton Communities with Temperature Fluctuations. *The American Naturalist*, 178(4):E85–E95, October 2011.

[14] John P Boyd. *Chebyshev and Fourier spectral methods*. Courier Corporation, 2001.

[15] Annalisa Bracco, Sophie Clayton, and Claudia Pasquero. Horizontal advection, diffusion, and plankton spectra at the sea surface. *Journal of Geophysical Research: Oceans*, 114(C2), 2009.

[16] Catherine E Brennan, Laura Bianucci, and Katja Fennel. Sensitivity of northwest north atlantic shelf circulation to surface and boundary forcing: A regional model assessment. *Atmosphere-Ocean*, 54(3):230–247, 2016.

[17] Hans Burchard and Hannes Rennau. Comparative quantification of physically and numerically induced mixing in ocean models. *Ocean Modelling*, 20(3):293–311, 2008.

[18] Giulia Castellani, Martin Losch, Benjamin A. Lange, and Hauke Flores. Modeling Arctic sea-ice algae: Physical drivers of spatial distribution and algae phenology. *Journal of Geophysical Research: Oceans*, 122(9):7466–7487, September 2017.

[19] Sean Celona, Sophia T Merrifield, Tony de Paolo, Nate Kaslan, Tom Cook, Eric J Terrill, and John A Colosi. Automated detection, classification, and tracking of internal wave signatures using x-band radar in the inner shelf. *Journal of Atmospheric and Oceanic Technology*, 38(4):789–803, 2021.

[20] Sylvia T Cole, Cimarron Wortham, Eric Kunze, and W Brechner Owens. Eddy stirring and horizontal diffusivity from argo float observations: Geographic and depth variability. *Geophysical Research Letters*, 42(10):3989–3997, 2015.

[21] SB Dalziel, PF Linden, and DL Youngs. Self-similarity and internal structure of turbulence induced by rayleigh–taylor instability. *Journal of fluid Mechanics*, 399:1–48, 1999.

[22] Daniel P Dauhajre, M Jeroen Molemaker, James C McWilliams, and Delphine Hypolite. Effects of stratification on shoaling internal tidal bores. *Journal of Physical Oceanography*, 51(10):3183–3202, 2021.

[23] David Deepwell, Marek Stastna, Magda Carr, and Peter A Davies. Interaction of a mode-2 internal solitary wave with narrow isolated topography. *Physics of Fluids*, 29(7), 2017.

[24] Curtis Deutsch and Thomas Weber. Nutrient ratios as a tracer and driver of ocean biogeochemistry. *Annual review of marine science*, 4:113–141, 2012.

[25] Paul E Dimotakis. Turbulent mixing. *Annu. Rev. Fluid Mech.*, 37:329–356, 2005.

[26] Georges Djoumna, Kevin G Lamb, and Yerubandi R Rao. Sensitivity of the parameterizations of vertical mixing and radiative heat fluxes on the seasonal evolution of the thermal structure of lake erie. *Atmosphere-Ocean*, 52(4):294–313, 2014.

[27] Marta Estrada and Elisa Berdalet. Effects of turbulence on phytoplankton. *NATO ASI Series Ecological Sciences*, 41:601–618, 1998.

[28] Katja Fennel, Jann Paul Mattern, Scott C. Doney, Laurent Bopp, Andrew M. Moore, Bin Wang, and Liuqian Yu. Ocean biogeochemical modelling. *Nature Reviews Methods Primers*, 2(1):76, September 2022.

[29] Raffaele Ferrari and Maxim Nikurashin. Suppression of eddy diffusivity across jets in the southern ocean. *Journal of Physical Oceanography*, 40(7):1501–1519, 2010.

[30] Ronald Aylmer Fisher. The wave of advance of advantageous genes. *Annals of eugenics*, 7(4):355–369, 1937.

[31] Baylor Fox-Kemper, Alistair Adcroft, Claus W Böning, Eric P Chassignet, Enrique Curchitser, Gokhan Danabasoglu, Carsten Eden, Matthew H England, Rüdiger Gerdes, Richard J Greatbatch, et al. Challenges and prospects in ocean circulation models. *Frontiers in Marine Science*, 6:65, 2019.

[32] Neil K Ganju, Mark J Brush, Brenda Rashleigh, Alfredo L Aretxabaleta, Pilar Del Barrio, Jason S Grear, Lora A Harris, Samuel J Lake, Grant McCardell, James O'Donnell, et al. Progress and challenges in coupled hydrodynamic-ecological estuarine modeling. *Estuaries and Coasts*, 39:311–332, 2016.

[33] Ann E Gargett. Vertical eddy diffusivity in the ocean interior. *Journal of Marine Research*, 42(2):359–393, 1984.

[34] Brad J Gemmell, Genesok Oh, Edward J Buskey, and Tracy A Villareal. Dynamic sinking behaviour in marine phytoplankton: rapid changes in buoyancy may aid in nutrient uptake. *Proceedings of the Royal Society B: Biological Sciences*, 283(1840):20161126, 2016.

[35] Massimo Germano, Ugo Piomelli, Parviz Moin, and William H Cabot. A dynamic subgrid-scale eddy viscosity model. *Physics of Fluids A: Fluid Dynamics*, 3(7):1760–1765, 1991.

[36] Esther D Goldstein, Jodi L Pirtle, Janet T Duffy-Anderson, William T Stockhausen, Mark Zimmermann, Matthew T Wilson, and Calvin W Mordy. Eddy retention and seafloor terrain facilitate cross-shelf transport and delivery of fish larvae to suitable nursery habitats. *Limnology and Oceanography*, 65(11):2800–2818, 2020.

[37] SM Griffies, AJ Adcroft, H Banks, CW Böning, EP Chassignet, G Danabasoglu, Sergey Danilov, E Deleersnijder, H Drange, M England, et al. Problems and prospects in large-scale ocean circulation models. *Proceedings of OceanObs*, 9:410–431, 2009.

[38] Dale B Haidvogel, Hernan Arango, W Paul Budgell, Bruce D Cornuelle, Enrique Curchitser, Emanuele Di Lorenzo, Katja Fennel, W Rockwell Geyer, Albert J Hermann, Lyon Lanerolle, et al. Ocean forecasting in terrain-following coordinates: Formulation and skill assessment of the regional ocean modeling system. *Journal of computational physics*, 227(7):3595–3624, 2008.

[39] Douglas S Hamilton, Morgane MG Perron, Tami C Bond, Andrew R Bowie, Rebecca R Buchholz, Cecile Guieu, Akinori Ito, Willy Maenhaut, Stelios Myriokefalitakis, Nazlı Olgun, et al. Earth, wind, fire, and pollution: Aerosol nutrient sources

and impacts on ocean biogeochemistry. *Annual Review of Marine Science*, 14:303–330, 2022.

[40] Sandhya Harnanan, Nancy Soontiens, and Marek Stastna. Internal wave boundary layer interaction: A novel instability over broad topography. *Physics of Fluids*, 27(1), 2015.

[41] Antti Hellsten, Klaus Ketelsen, Matthias Sühring, Mikko Auvinen, Björn Maronga, Christoph Knigge, Fotios Barmpas, Georgios Tsegas, Nicolas Moussiopoulos, and Siegfried Raasch. A nested multi-scale system implemented in the large-eddy simulation model palm model system 6.0. *Geoscientific Model Development*, 14(6):3185–3214, 2021.

[42] Robert L Higdon and Andrew F Bennett. Stability analysis of operator splitting for large-scale ocean modeling. *Journal of Computational Physics*, 123(2):311–329, 1996.

[43] Greg Holloway. Estimation of oceanic eddy transports from satellite altimetry. *Nature*, 323(6085):243–244, 1986.

[44] Joanne E Hopkins, Matthew R Palmer, Alex J Poulton, Anna E Hickman, and Jonathan Sharples. Control of a phytoplankton bloom by wind-driven vertical mixing and light availability. *Limnology and Oceanography*, 66(5):1926–1949, 2021.

[45] J-J Hung, Y-H Wang, K-H Fu, IH Lee, S-S Tsai, C-Y Lee, W-T Lu, Y-J Shen, and Y-H Lin. Biogeochemical responses to internal-wave impacts in the continental margin off dongsha atoll in the northern south china sea. *Progress in Oceanography*, 199:102689, 2021.

[46] Joachim Jansen, Sally MacIntyre, David C Barrett, Yu-Ping Chin, Alicia Cortés, Alexander L Forrest, Allison R Hrycik, Rosemary Martin, Bailey C McMeans, Milla Rautio, et al. Winter limnology: How do hydrodynamics and biogeochemistry shape ecosystems under ice? *Journal of Geophysical Research: Biogeosciences*, 126(6), 2021.

[47] Igor Kamenkovich, Pavel Berloff, Michael Haigh, Luolin Sun, and Yueyang Lu. Complexity of mesoscale eddy diffusivity in the ocean. *Geophysical Research Letters*, 48(5), 2021.

[48] Daniel Kamykowski. A preliminary biophysical model of the relationship between temperature and plant nutrients in the upper ocean. *Deep Sea Research Part A. Oceanographic Research Papers*, 34(7):1067–1079, 1987.

[49] Madhavan Girijakumari Keerthi, Channing J Prend, Olivier Aumont, and Marina Lévy. Annual variations in phytoplankton biomass driven by small-scale physical processes. *Nature Geoscience*, 15(12):1027–1033, 2022.

[50] Patrice Klein and Guillaume Lapeyre. The oceanic vertical pump induced by mesoscale and submesoscale turbulence. *Annual review of marine science*, 1:351–375, 2009.

[51] Rajesh Kumar, Junde Li, Kate Hedstrom, Alexander V Babanin, David M Holland, Petra Heil, and Youmin Tang. Intercomparison of arctic sea ice simulation in roms-cice and roms-budgell. *Polar Science*, 29:100716, 2021.

[52] Pijush K Kundu, Ira M Cohen, and David R Dowling. *Fluid mechanics*. Academic press, 2015.

[53] Arnaud Laurent, Katja Fennel, and Angela Kuhn. An observation-based evaluation and ranking of historical earth system model simulations in the northwest north atlantic ocean. *Biogeosciences*, 18(5):1803–1822, 2021.

[54] Diane Lavoie, Kenneth Denman, and Christine Michel. Modeling ice algal growth and decline in a seasonally ice-covered region of the Arctic (Resolute Passage, Canadian Archipelago). *Journal of Geophysical Research: Oceans*, 110(C11), 2005. _eprint: https://onlinelibrary.wiley.com/doi/pdf/10.1029/2005JC002922.

[55] Sierra Legare and Marek Stastna. Implications of reynolds averaging for reactive tracers in turbulent flows. *Journal of Marine Science and Engineering*, 11(11):2036, 2023.

[56] Marcel Lesieur, Olivier Métais, and Pierre Comte. *Large-eddy simulations of turbulence*. Cambridge university press, 2005.

[57] Marina Lévy, Damien Couespel, Clément Haëck, Madhavan Girijakumari Keerthi, Inès Mangolte, and Channing J Prend. The impact of fine-scale currents on biogeochemical cycles in a changing ocean. *Annual Review of Marine Science*, 16:191–215, 2024.

[58] Marina Lévy and Adrian P Martin. The influence of mesoscale and submesoscale heterogeneity on ocean biogeochemical reactions. *Global Biogeochemical Cycles*, 27(4):1139–1150, 2013.

[59] Marina Lévy, Laure Resplandy, and Matthieu Lengaigne. Oceanic mesoscale turbulence drives large biogeochemical interannual variability at middle and high latitudes. *Geophysical Research Letters*, 41(7):2467–2474, 2014.

[60] Dewang Li, Wen-Chen Chou, Yung-Yen Shih, Guan-Yu Chen, Yi Chang, Chun Hoe Chow, Tsang-Yuh Lin, and Chin-Chang Hung. Elevated particulate organic carbon export flux induced by internal waves in the oligotrophic northern south china sea. *Scientific reports*, 8(1):2042, 2018.

[61] Guangpeng Liu, Annalisa Bracco, and Alexandra Sitar. Submesoscale mixing across the mixed layer in the gulf of mexico. *Frontiers in Marine Science*, 8:615066, 2021.

[62] J David Logan. *An introduction to nonlinear partial differential equations*, volume 89. John Wiley & Sons, 2008.

[63] M. Lévy, D. Iovino, L. Resplandy, P. Klein, G. Madec, A.-M. Tréguier, S. Masson, and K. Takahashi. Large-scale impacts of submesoscale dynamics on phytoplankton: Local and remote effects. *Ocean Modelling*, 43-44:77–93, January 2012.

[64] Marina Lévy, Patrice Klein, and Anne-Marie Treguier. Impact of sub-mesoscale physics on production and subduction of phytoplankton in an oligotrophic regime. *Journal of Marine Research*, 59(4):535–565, July 2001.

[65] John Marshall, Emily Shuckburgh, Helen Jones, and Chris Hill. Estimates and implications of surface eddy diffusivity in the southern ocean derived from tracer transport. *Journal of physical oceanography*, 36(9):1806–1821, 2006.

[66] K. M. Meiners, S. Arndt, S. Bestley, T. Krumpen, R. Ricker, M. Milnes, K. Newbery, U. Freier, S. Jarman, R. King, R. Proud, S. Kawaguchi, and B. Meyer. Antarctic pack ice algal distribution: Floe-scale spatial variability and predictability from physical parameters. *Geophysical Research Letters*, 44(14):7382–7390, 2017.

[67] John Miles. On transversely isotropic eddy viscosity. *Journal of physical oceanography*, 24(5):1077–1079, 1994.

[68] Chin-Hoh Moeng, Jimy Dudhia, Joe Klemp, and Peter Sullivan. Examining two-way grid nesting for large eddy simulation of the pbl using the wrf model. *Monthly weather review*, 135(6):2295–2311, 2007.

[69] Domingo Muñoz-Esparza, Branko Kosović, Clara García-Sánchez, and Jeroen Van Beeck. Nesting turbulence in an offshore convective boundary layer using large-eddy simulations. *Boundary-layer meteorology*, 151:453–478, 2014.

[70] Sheehan Olver. On the convergence rate of a modified fourier series. *Mathematics of Computation*, 78(267):1629–1645, 2009.

[71] C Pasquero. Differential eddy diffusion of biogeochemical tracers. *Geophysical research letters*, 32(17), 2005. Publisher: Wiley Online Library.

[72] Stephen B Pope. *Turbulent flows*. Cambridge university press, 2000.

[73] Jacek Pozorski and Jean-Pierre Minier. Modeling scalar mixing process in turbulent flow. In *First Symposium on Turbulence and Shear Flow Phenomena*. Begel House Inc., 1999.

[74] Channing J Prend, Glenn R Flierl, Katherine M Smith, and Alexis K Kaminski. Parameterizing eddy transport of biogeochemical tracers. *Geophysical Research Letters*, 48(21), 2021.

[75] Channing J Prend, Madhavan Girijakumari Keerthi, Marina Lévy, Olivier Aumont, Sarah T Gille, and Lynne D Talley. Sub-seasonal forcing drives year-to-year variations of southern ocean primary productivity. *Global biogeochemical cycles*, 36(7), 2022.

[76] Timour Radko. *Double-diffusive convection*. Cambridge University Press, 2013.

[77] Laure Resplandy, Marina Lévy, and Dennis J McGillicuddy Jr. Effects of eddy-driven subduction on ocean biological carbon pump. *Global Biogeochemical Cycles*, 33(8):1071–1084, 2019.

[78] Kelvin J Richards and Stuart J Brentnall. The impact of diffusion and stirring on the dynamics of interacting populations. *Journal of theoretical biology*, 238(2):340–347, 2006.

[79] Krysten Rutherford, Katja Fennel, Dariia Atamanchuk, Douglas Wallace, and Helmuth Thomas. A modelling study of temporal and spatial pco 2 variability on the biologically active and temperature-dominated scotian shelf. *Biogeosciences*, 18(23):6271–6286, 2021.

[80] JB Sallée, Kevin Speer, R Morrow, and Rick Lumpkin. An estimate of lagrangian eddy statistics and diffusion in the mixed layer of the southern ocean. *Journal of Marine Research*, 66(4):441–463, 2008.

[81] Mathilde Schapira and Laurent Seuront. Nutrient patchiness, phytoplankton surge-uptake, and turbulent history: A theoretical approach and its experimental validation. *Fluids*, 5(2):80, 2020.

[82] Alexander F Shchepetkin and James C McWilliams. The regional oceanic modeling system (roms): a split-explicit, free-surface, topography-following-coordinate oceanic model. *Ocean modelling*, 9(4):347–404, 2005.

[83] Eric D Skyllingstad and Donald W Denbo. An ocean large-eddy simulation of langmuir circulations and convection in the surface mixed layer. *Journal of Geophysical Research: Oceans*, 100(C5):8501–8522, 1995.

[84] Katherine M Smith, Peter E Hamlington, and Baylor Fox-Kemper. Effects of submesoscale turbulence on ocean tracers. *Journal of Geophysical Research: Oceans*, 121(1):908–933, 2016.

[85] Katepalli R Sreenivasan. Turbulent mixing: A perspective. *Proceedings of the National Academy of Sciences*, 116(37):18175–18183, 2019.

[86] Bharath Srinivasan. A guide to the michaelis–menten equation: steady state and beyond. *The FEBS journal*, 289(20):6086–6098, 2022.

[87] Marek Stastna and Sierra Legare. Simulations of shoaling large amplitude internal waves: perspectives and outlook. (Accepted for publication), 2024.

[88] Christopher J Subich, Kevin G Lamb, and Marek Stastna. Simulation of the navier–stokes equations in three dimensions with a spectral collocation method. *International Journal for Numerical Methods in Fluids*, 73(2):103–129, 2013.

[89] Yi Sui, Jinyu Sheng, DanLing Tang, and Jiuxing Xing. Study of storm-induced changes in circulation and temperature over the northern south china sea during typhoon linfa. *Continental Shelf Research*, 249:104866, 2022.

[90] John R Taylor and Andrew F Thompson. Submesoscale dynamics in the upper ocean. *Annual Review of Fluid Mechanics*, 55:103–127, 2023.

[91] John Ryan Taylor. Turbulent mixing, restratification, and phytoplankton growth at a submesoscale eddy. *Geophysical Research Letters*, 43(11):5784–5792, 2016.

[92] Letizia Tedesco, Marcello Vichi, Jari Haapala, and Tapani Stipa. A dynamic Biologically Active Layer for numerical studies of the sea ice ecosystem. *Ocean Modelling*, 35(1):89–104, January 2010.

[93] Vinicius Beltram Tergolina, Enrico Calzavarini, Gilmar Mompean, and Stefano Berti. Effects of large-scale advection and small-scale turbulent diffusion on vertical phytoplankton dynamics. *Physical Review E*, 104(6):065106, 2021.

[94] Vinicius Beltram Tergolina, Enrico Calzavarini, Gilmar Mompean, and Stefano Berti. Surface light modulation by sea ice and phytoplankton survival in a convective flow model. *The European Physical Journal Plus*, 137(12):1387, 2022.

[95] Lloyd N Trefethen. Spectral methods in matlab, volume 10 of software, environments, and tools. *Society for Industrial and Applied Mathematics (SIAM), Philadelphia, PA*, 24:57, 2000.

[96] G Triantafyllou, Fengchao Yao, G Petihakis, KP Tsiaras, DE Raitsos, and Ibrahim Hoteit. Exploring the red sea seasonal ecosystem functioning using a three-dimensional biophysical model. *Journal of Geophysical Research: Oceans*, 119(3):1791–1811, 2014.

[97] Giuditta Trinci, Gemma L Harvey, Alexander J Henshaw, Walter Bertoldi, and Franz Hölker. Life in turbulent flows: interactions between hydrodynamics and aquatic organisms in rivers. *Wiley interdisciplinary reviews: Water*, 4(3), 2017.

[98] JE Truscott and J Brindley. Ocean plankton populations as excitable media. *Bulletin of Mathematical Biology*, 56(5):981–998, 1994.

[99] Anastasios Tsoularis and James Wallace. Analysis of logistic growth models. *Mathematical biosciences*, 179(1):21–55, 2002.

[100] Eisuke Tsutsumi, Takeshi Matsuno, Sachihiko Itoh, Jing Zhang, Tomoharu Senjyu, Akie Sakai, Keunjong Lee, Daigo Yanagimoto, Ichiro Yasuda, Hiroshi Ogawa, et al. Vertical fluxes of nutrients enhanced by strong turbulence and phytoplankton bloom around the ocean ridge in the luzon strait. *Scientific reports*, 10(1):17879, 2020.

[101] Peter Turchin. Does population ecology have general laws? *Oikos*, 94(1):17–26, 2001.

[102] Giulia Valerio, Marco Pilotti, Clelia Luisa Marti, and Jö rg Imberger. The structure of basin-scale internal waves in a stratified lake in response to lake bathymetry and wind spatial and temporal distribution: Lake iseo, italy. *Limnology and Oceanography*, 57(3):772–786, 2012.

[103] Vasiliy Vlasenko, Nataliya Stashchuk, and Robert McEwan. High-resolution modelling of a large-scale river plume. *Ocean Dynamics*, 63:1307–1320, 2013.

[104] Vitaly Volpert and Sergei Petrovskii. Reaction–diffusion waves in biology. *Physics of life reviews*, 6(4):267–310, 2009.

[105] Peter J Wangersky. Lotka-volterra population models. *Annual Review of Ecology and Systematics*, 9(1):189–218, 1978.

[106] Asiri Umenga Weerasuriya, Xuelin Zhang, Kam Tim Tse, Chun-Ho Liu, and Kenny CS Kwok. Rans simulation of near-field dispersion of reactive air pollutants. *Building and Environment*, 207:108553, 2022.

[107] Daniel B Whitt, Marina Lévy, and John R Taylor. Submesoscales enhance storm-driven vertical mixing of nutrients: insights from a biogeochemical large eddy simulation. *Journal of Geophysical Research: Oceans*, 124(11):8140–8165, 2019.

[108] David W Winkler, Christian Jørgensen, Christiaan Both, Alasdair I Houston, John M McNamara, Douglas J Levey, Jesko Partecke, Adam Fudickar, Alex Kacelnik, David Roshier, et al. Cues, strategies, and outcomes: how migrating vertebrates track environmental change. *Movement Ecology*, 2:1–15, 2014.

[109] John C Wyngaard. *Turbulence in the Atmosphere*. Cambridge University Press, 2010.

[110] Heng Xiao and Paola Cinnella. Quantification of model uncertainty in rans simulations: A review. *Progress in Aerospace Sciences*, 108:1–31, 2019.

[111] Shuolin Xiao and Di Yang. Effect of oil plumes on upper-ocean radiative transfer—a numerical study. *Ocean Modelling*, 145:101522, 2020.

[112] Jie Zhang, Andrés E Tejada-Martínez, and Qiong Zhang. Developments in computational fluid dynamics-based modeling for disinfection technologies over the last two decades: A review. *Environmental modelling & software*, 58:71–85, 2014.

[113] Jie Zhang, Andrés E Tejada-Martínez, Qiong Zhang, and Hongxia Lei. Evaluating hydraulic and disinfection efficiencies of a full-scale ozone contactor using a rans-based modeling framework. *Water Research*, 52:155–167, 2014.

[114] Ruichen Zhu, Haiyuan Yang, Mingkui Li, Zhaohui Chen, Xin Ma, Jinzhuo Cai, and Lixin Wu. Observations reveal vertical transport induced by submesoscale front. *Scientific Reports*, 14(1):4407, 2024.

[115] A Zulberti, NL Jones, and GN Ivey. Observations of enhanced sediment transport by nonlinear internal waves. *Geophysical Research Letters*, 47(19):e2020GL088499, 2020.

APPENDICES

Appendix A

Mathematical Treatment of Other Example Reactions

A.1 Multi-Component Systems

The Lotka-Volterra (LV) equations are a simple example of a non-linear multi-component system [105]. In ODE form, the system can be written as

$$\theta_t = \theta - \theta\phi, \tag{A.1}$$

$$\phi_t = \theta\phi - \phi. \tag{A.2}$$

Note that all rate constants are taken to be 1 in the above. We want to consider how Reynolds averaging or LES filtering affects a coupled system of DEs. It is sufficient to consider the LV system in ODE form since the eddy flux and **sfs** flux terms introduced are the same for all ADR equations.

Let us start by applying a Reynolds decomposition to both components so that $\theta = \Theta + \theta'$ and $\phi = \Phi + \phi'$. Substituting and averaging yields

$$\Theta_t = \Theta - \Theta\Phi - \overline{\theta'\phi'}, \tag{A.3}$$

$$\Phi_t = \Theta\Phi - \Phi + \overline{\theta'\phi'}. \tag{A.4}$$

Under LES filtering the LV system becomes

$$\langle\theta\rangle_t = \langle\theta\rangle - \langle\theta\rangle\langle\phi\rangle + (\langle\theta\rangle\langle\phi\rangle - \langle\theta\phi\rangle) \tag{A.5}$$

$$= \langle\theta\rangle - \langle\theta\rangle\langle\phi\rangle + (\langle\theta\rangle\langle\phi\rangle - \langle\langle\theta\rangle\langle\phi\rangle\rangle) - (\langle\langle\theta\rangle\phi'\rangle + \langle\theta'\langle\phi\rangle\rangle) - \langle\theta'\phi'\rangle, \tag{A.6}$$

$$\langle\phi\rangle_t = \langle\theta\rangle\langle\phi\rangle - \langle\phi\rangle - (\langle\theta\rangle\langle\phi\rangle - \langle\theta\phi\rangle) \tag{A.7}$$

$$= \langle\theta\rangle\langle\phi\rangle - \langle\phi\rangle - (\langle\theta\rangle\langle\phi\rangle - \langle\langle\theta\rangle\langle\phi\rangle\rangle) + (\langle\langle\theta\rangle\phi'\rangle + \langle\theta'\langle\phi\rangle\rangle) + \langle\theta'\phi'\rangle. \tag{A.8}$$

The introduction of unknown terms both under Reynolds averaging and LES filtering is due to the presence of a non-linear reaction term. Under Reynolds averaging, the eddy reaction transfers population between θ and ϕ. Note that θ' and ϕ' can have opposing signs and so population transfer can be either from θ to ϕ or in the opposite direction. Compared to the simple sink term that was introduced when Reynolds averaging Fisher's equation, the effect of the two component eddy reaction term is harder to interpret and predict. We see a similar effect in the filtered equations, though there are many more unknown terms so understanding their distinct or even joint effects is challenging.

A.2 Using Taylor Polynomials on Michaelis-Menten Reaction Terms

The simplest form of a reaction function describing Michaelis-Menten kinetics [86] is

$$F(\theta) = \frac{\theta}{1+\theta}. \tag{A.9}$$

Due to the form of the equation (being non-linear and not a polynomial), substituting a Reynolds decomposition and averaging is fruitless and similarly for LES filtering.

Instead, we need to use a Taylor polynomial to approximate the equation. The Michaelis-Menten equation as written (with all parameters taken to be one) has a discontinuity at $\theta = -1$. Considering that θ is interpreted as a concentration in models in which this equation would be used, it is safe to assume $\theta \geq 0$ and so the discontinuity can safely be ignored.

The degree 3 Taylor polynomial corresponding to equation A.9 around a point $a \geq 0$ is

$$P_3(\theta) = \frac{a}{1+a} + \frac{1}{(1+a)^2}(\theta - a) - \frac{1}{(1+a)^3}(\theta - a)^2 + \frac{1}{(1+a)^3}(\theta - a)^3. \tag{A.10}$$

For simplicity take $a = 0$, then

$$P_3(\theta) = \theta - \theta^2 + \theta^3. \tag{A.11}$$

The first two terms are identical to the terms in Fisher's equation. The cubic term, being non-linear, will inevitably introduce more unknown terms under Reynolds averaging and LES filtering. In sections 2.4.2 and 2.5.2 we showed how to apply either procedure to θ^n for any positive integer n. Here, we have $n = 3$, so the terms introduced by applying the Reynolds averaging procedure to θ^3 are

$$\overline{\theta^3} = \overline{(\Theta + \theta')^3} = \Theta^3 + 3\Theta\overline{(\theta')^2} + \overline{(\theta')^3}, \tag{A.12}$$

and the resulting Reynolds averaged Taylor polynomial is

$$\overline{P_3(\theta)} = \Theta - \Theta^2 + \Theta^3 - \overline{(\theta')^2} + 3\Theta\overline{(\theta')^2} + \overline{(\theta')^3}. \tag{A.13}$$

The cubic term in $P_3(\theta)$ introduces two additional unknown terms that rely on the fluctuation, one of which involves third order correlations.

Under LES filtering θ^3 becomes

$$\langle\theta^3\rangle = \langle\theta\rangle^3 + \langle\langle\theta\rangle^3\rangle - \langle\theta\rangle^3 + 3\langle\langle\theta\rangle^2\theta' + \langle\theta\rangle(\theta')^2\rangle + \langle(\theta')^3\rangle. \tag{A.14}$$

The filtered Taylor polynomial is

$$\begin{aligned}
\langle P_3(\theta)\rangle =& \langle\theta\rangle - \langle\theta\rangle^2 + \langle\theta\rangle^3 && \text{(A.15)}\\
&- \langle\langle\theta\rangle^2\rangle + \langle\theta\rangle^2 - 2\langle\langle\theta\rangle\theta'\rangle - \langle(\theta')^2\rangle && \text{(A.16)}\\
&+ \langle\langle\theta\rangle^3\rangle - \langle\theta\rangle^3 + 3\langle\langle\theta\rangle^2\theta' + \langle\theta\rangle(\theta')^2\rangle + \langle(\theta')^3\rangle && \text{(A.17)}
\end{aligned}$$

The cubic term introduces new unknown terms (third line). Most notably, increasing the order of the non-linearity considered to some integer value n increases the number of terms in the cross–scale interaction tensor by $n - 1$.

Glossary

sfs flux An unknown transport term that arises in the spatially filtered ADR equation. The **sfs** flux has resolved, cross-scale, and **sfs** components. 23

sfs reaction An unknown reaction term that arises in the spatially filtered ADR equation. The **sfs** reaction has resolved, cross-scale, and **sfs** components. The form of each component depends on that of the reaction in question. 24

Damköhler number Ratio of the reactive to advective timescales. Defined as $Da = \frac{\alpha L}{\mathcal{U}}$ where α is the reaction rate and L and $\mathcal{U}$ are the characteristic length and velocity scales. 9, 16

eddy flux Transport of tracer fluctuations by velocity fluctuations. An unknown transport term that arises in the Reynolds averaged ADR equation. 7

eddy reaction An unknown reaction term that arises in the Reynolds averaged ADR equation. The form of the term depends on the reaction in question. 7

passive tracer A tracer that is passive with respect to fluid dynamics and non-reactive. 2, 14

reactive tracer A tracer that is passive with respect to fluid dynamics and undergoes a reaction. 2, 14

Reynolds average An average taken over an ensemble. 5

toy models Models that are highly simplified, often through the implementation of a prescribed velocity field. 3